

**Представляем**  
**научные достижения мира.**  
**Естественные науки**

Presenting  
Academic Achievements to the World.  
Natural Science

Papers from the conference for young scientists  
«Presenting Academic Achievements to the World»

March 3–4, 2011  
Saratov

Issue 2

Представляем  
научные достижения миру.  
Естественные науки

Материалы научной конференции молодых ученых  
«Presenting Academic Achievements to the World»

Март 3–4, 2011  
Саратов

Выпуск 2

УДК 5(082)  
ББК 20я43  
П71

**Представляем научные достижения мира. Гуманитарные науки** : материалы научной конференции молодых ученых «Presenting Academic Achievements to the World». – Саратов : Изд-во Сарат. ун-та, 2011. – Вып. 2 – XXX с. : ил.  
ISBN 978-5-292-

В данном сборнике опубликованы материалы участников секции естественных наук научной конференции молодых ученых «Presenting Academic Achievements to the World», которая состоялась в Саратовском государственном университете 3–4 марта 2011 года. В сборник включены статьи с результатами исследований в области физики, химии, географии, геологии и информационных технологий.

This publication assembles papers given at the conference for young scientists «Presenting Academic Achievements to the World» which was held in March 3–4, 2011 at Saratov State University. The articles present the results in such fields of natural science as Physics, Chemistry, Geography, Geology and Information Technology.

**Редакционная коллегия:**

*Н. Н. Иголкина* (отв. редактор), *Л. В. Левина* (отв. секретарь),  
*М. В. Фелипер, Д. В. Пономарев, Т. А. Сергеева*

DYNAMICAL BEHAVIOR OF VAN DER POL GENERATOR  
WITH TIME DELAYED FEEDBACK

**M. I. Balakin**

Saratov State University

Self-sustained oscillatory systems with time-delayed feedback is a very important class of systems for many fields of science, including biophysics, nonlinear optics, radio physics, etc [Неймарк, 1988; Дмитриев, 1989]. It is well known that such systems can generate complex, e.g. chaotic, oscillations. Therefore studying them could help researchers better understand dynamical behavior of systems with many degrees of freedom.

Time-delay can give rise to several interesting and novel phenomena such as multistable states, amplitude death, Neimark-Saker type bifurcation, hysteresis, etc, which cannot be observed in the absence of delay in the underlying systems [Атай, 2004; Ким, 1997; Рамана, 2004]. Indication and study of these phenomena is of special importance to certain areas of technology, for telecommunications in particular.

Study of the dynamics of distributed systems is a laborious task, which is associated with an infinite number of degrees of freedom and the presence of several control parameters. Thus it is important to consider a simple model that demonstrates all the basic features of the system dynamics, which could be treated by numerical and analytical methods.

In previously published works method of averaging was widely used to obtain solution of underlying equations at only one value of time delay [Баранов, 2010; Гинзбург, 1980; Рубаник, 1969; Pyragiene, 2005; Pyragas, 2006]. Preliminary results show that there is substantial difference in solutions of complete and averaged equations. It is also important to investigate dynamical behavior of system at several values of time delay in order to reveal diver-

Работа издана в авторской редакции

УДК 5(082)  
ББК 20я43

© Саратовский государственный университет, 2011  
ISBN 978-5-292-04042-2

sity of physical phenomena and oscillation regimes. Therefore it is particularly important to investigate complete equations at different values of time delay.

Van der Pol generator with time-delayed feedback can be represented by second-order delayed differential equation of a form:

$$\ddot{x}(t) + \lambda \dot{x}(t) + x(t) = [\varepsilon - x^2(t - \tau_d)]\dot{x}(t - \tau_d) \quad (1)$$

Here  $\lambda$  is the characteristic of dissipation, and  $\varepsilon$  is responsible for nonlinearity.  $\tau_d$  represents value of time delay.  
This paper deals with dynamical behavior analysis of van der Pol generator with time-delayed feedback.

Numerical simulation of equation (1) was carried out using the Runge-Kutta fourth order method.

In the modeling we took  $\lambda = 3$  due to the features of selected radio physical analogy.

At  $\tau_d = 0.05$  and  $\varepsilon > 3.01$  periodic orbit of period one (limit cycle) is born from fixed point. At  $\varepsilon \approx 8.0$  loops appear at the cycle. If one increases  $\varepsilon$ , radius of limit cycle grows and its shape is distorted. At  $\varepsilon = 30.3$  limit cycle loses its stability. It can be explained considering features of selected model. Volt-ampere characteristic of the amplifier is approximated with third-degree polynomial which is unbounded mathematically. Thus the system can be investigated numerically only in a certain range of parameters.

At  $\tau_d = 2.5$  a number of special physical phenomena can be displayed. At  $\varepsilon > 3.53$  limit cycle is born from fixed point. If one increases  $\varepsilon$  radius of limit, cycle grows and its shape is distorted. This effect took place because limit cycle gets closer to a saddle-type stable state located in the origin of coordinates. Thus loops appear at the cycle. At  $\varepsilon = 6.75$  torus is born from limit cycle. Torus exists at  $\varepsilon \in [6.75, 7.48]$ . At  $\varepsilon = 7.49$  torus vanishes and period-4 orbit is born. Then at  $\varepsilon = 7.68$  period-8 orbit is born through period-doubling bifurcation. At  $\varepsilon = 7.75$  chaotic attractor is born from period-8 orbit. At  $\varepsilon = 8.96$  attractor loses its stability.

At  $\varepsilon \in [4.78, 7.75]$  two different oscillation regimes co-exist in the system. Second regime can be displayed by choosing initial conditions that are not in the vicinity of origin of coordinates. The second regime represents harmonic oscillations, which in phase space corresponds to the limit cycle. With increasing  $\varepsilon$  the radius of cycle grows and the shape is distorted. At  $\varepsilon = 7.75$  phase trajectory jumps to the first regime.

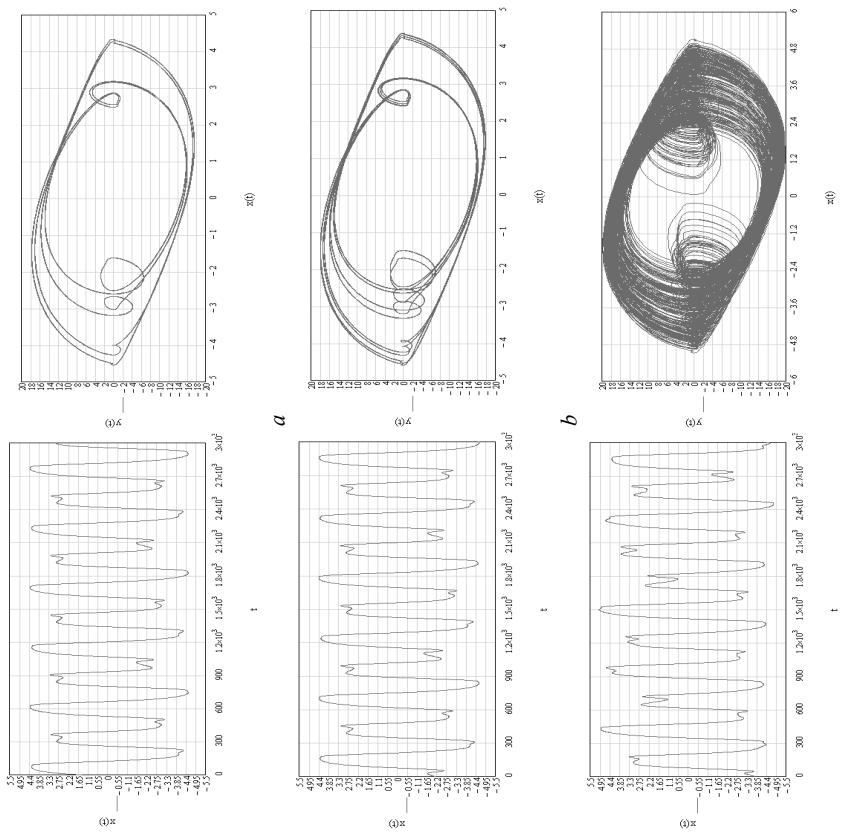


Fig. 1. Time series and phase planes.  $\tau_d = 2.5$ ,  $\varepsilon = 2.5$ ,  $\varepsilon = 7.65$  (a),  $7.75$ (b),  $7.75$ (c).

At  $\tau_d = 27.5$  oscillation excitation takes occurs at  $\varepsilon = 3.06$  and oscillation stops occurs at  $\varepsilon = 3.0$ . This fact shows the existence of hysteresis in the system, one of the most important features of time delay systems. At  $\varepsilon = 5.5$  torus is born from period-1 orbit. At  $\varepsilon = 5.55$  torus vanishes and a chaotic attractor is born. At  $\varepsilon = 7.25$  attractor loses its stability.

This paper deals with Dynamical behavior of van der Pol generator with time delayed feedback. Some preliminary results have been obtained. Using time-delayed feedback loop in the van der Pol generator substantially changes dynamical behavior of the generator. Time delay appears to give rise to several interesting and important physical phenomena, which do not exist in the system without time delay: multistable states, chaotic attractor, hysteresis. Variation of time delay leads to possible changes in dynamics of system. Therefore this effect can be used to control dynamical behavior of the system and choose oscillation regime.

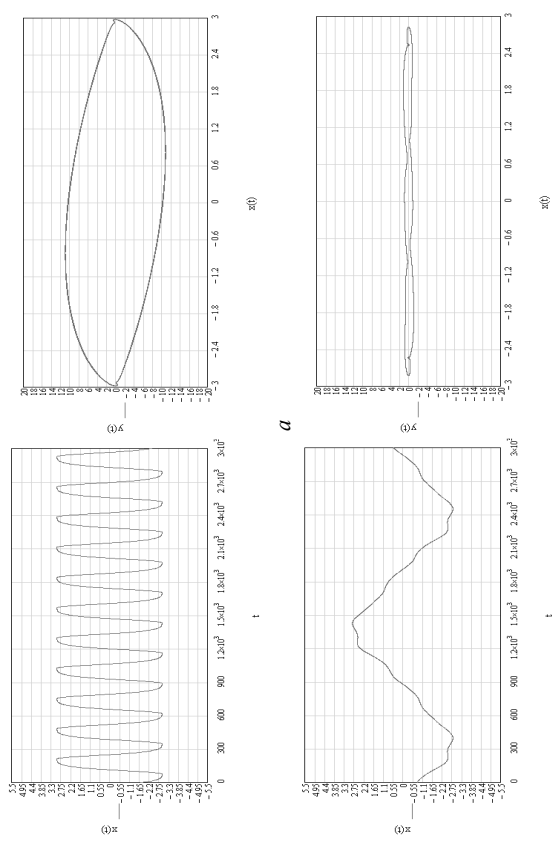


Fig. 2. Time series and phase planes at different initial conditions.  $\tau_d = 2.5, \varepsilon = 6$ .

## REFERENCES

1. Баранов С. В., Кузнецов С. П., Пономаренко В. И. Хаос в фазовой динамике осциллятора винн дер Поля с модулированной обратностью и дополнительной запаздывающей обратной связью. Изв. вузов «ПНДР», т. 18, №1, 2010.
2. Гицбург Н. С., Кузнецов Н. П. Периодические стохастические автомодуляционные режимы в электронных генераторах с распределенным взаимодействием. В кн.: Релаксивистская высокочастотная электроника. Проблемы повышения монолитности и частоты излучения. Горький, ИИФ АН СССР, 1986, с. 101-144.
3. Дмитриев А. С., Кислов В. Я. Стохастические колебания в радиофизике и электронике. М.: Наука, 1989. 280 с.

4. Неймарк Ю. И., Ланда П. С. Стохастические и хаотические колебания. М.: Наука, 1987. 424 с.
5. Рубанук В. П. Колебания квазилинейных систем с запаздыванием. М.: Наука, 1969. 288 с.
6. Atay F. M., Jost J., and Wende A., Phys. Rev. Lett. 92, 074104 (2004).
7. Kim S., Park S. H., and Ryu C. S., Phys. Rev. Lett. 79, 2911 (1997).
8. Pyragiene T., Pyragas K., Phys. Rev. E 72, 026203 (2005).
9. Pyragas K., Pyragas K., Phys. Rev. E 73, 036215 (2006).
10. Ramana Reddy D. V., Sen A., and Ramaswamy R., Phys. Rev. E 74, 035204(R) (2006).

## DEFORMATION MODELS OF MATERIALS IN RADIATION MEDIUM

**M.Y. Bogina**

Balashov Institute of Saratov State University

The experimental data analysis on how radiation influences the behavior of materials and structures suggests that the radiation medium affects the loaded structure elements in the following way: two interrelated processes occur in the structure element under load – deformation and destruction (deformation can occur both due to creep, and due to growing number of defects and other injuries, which affect the mechanical properties of materials and lead to changes in the strained state of the body). In radiation medium the structural element gets a radiation dose that, according to some law, leads to changes in short-term and long-term mechanical properties and radiation swelling, resulting in changing the deformation structure and the kinetics of its destruction.

The physical model of the phenomena occurring in structural elements can be taken to build mathematical models in the light of the theory of structural parameters and the methods of continuum mechanics. The mathematical model of deformation and destruction will contain not only the mechanical parameters (stress, strain), but also additional options connected with the effect of radiation factors. If the theory of structural parameters is applied the material behavior can be described by certain parameters of state. The state is considered to be given, if, in addition to parameters of external effects characterizing the radiation field, pressure, temperature, a certain number of structural parameters characterizing the internal state structure are also given. Some kinetic equations are compiled for these structural parameters, which include damage, creep strain and other parameters. These kinetic equations allow to determine the laws of their changes under the influence of stress state, loading history, external influences. In mechanics a system of parameters is commonly used to describe the deformation processes including: stress  $\sigma$ , strain  $\epsilon$ , the temperature  $T$ , time  $t$ . This system is not complete enough when we'd like to describe the processes of deformation and destruction. For a more accurate de-

scription, in addition to the above-mentioned parameters, the damage parameter  $\Pi$  is introduced, the radiation swelling parameter  $\varepsilon_\phi$  might be introduced as well as the dose of irradiation  $\Phi$ . These parameters may vary in different limits, but, if necessary, they can be normalized and their change from 0 to 1 can be guaranteed.

In order to describe the process of deformation and destruction of structural component in the radiation medium the system of key parameters – stress, strain, temperature and time should be completed with the following parameters: damage  $\Pi$  and irradiation dose  $\Phi$ . The change in the damage parameter can be described by the following equation:

$$d\Pi = f_1 d\sigma + f_2 d\sigma + f_3 dT + F_1 d\varepsilon_\Phi + F_2 d\Phi,$$

where  $f_1, f_2, f_3, F_1, F_2$  are some functions  $\sigma, T, \Pi, \varepsilon_\Phi, \Phi$ .

We consider the construction of physical correlation describing the deformation and destruction of the material in the light of radiation exposure in relation to two cases. The first case is the nonlinear deformation due to damage and radiation impact. The second case is the deformation due to creep and radiation exposure. To describe the deformation process we will use the physical correlation in the form of  $\sigma = f(\varepsilon, \Pi, \Phi)$ .

The specific form of this equation may be different. There are several types of the parameters  $\Pi, \Phi$  influencing the specific form of this equation. The first type is that we can represent the dependence  $\sigma = f(\varepsilon, \Pi, \Phi)$  as a multiplication of some functions of influence:

$$\sigma = f_1(\varepsilon) \cdot f_2(\Pi) \cdot f_3(\Phi).$$

Function  $f_1(\varepsilon)$  may have the form of  $f_1(\varepsilon) = A\varepsilon^k$  according to the Byulfinger Law,  $f_1(\varepsilon) = A[1 - (1 - \varepsilon/m)^k]$  according to the dependence of Saint-Venant,  $f_1(\varepsilon) = A\varepsilon - m\varepsilon^3$  is a cubic parabola;  $f_1(\varepsilon) = A\varepsilon[1 + (\varepsilon/m)^2]^{1/2}$  is the dependence of Sokolovsky;  $f_1(\varepsilon) = E\varepsilon - m\varepsilon^n$  is the three-parameter dependence;  $f_1(\varepsilon) = A\varepsilon - m\varepsilon^3 - n\varepsilon^5$  is the fifth-degree polynomial;  $f_1(\varepsilon) = A\varepsilon^m - k\varepsilon^n$  is the four-constant dependence.  $E, A, k, m, n$  are coefficients in the formulae.

Function  $f_2(\Pi)$  may have the linear form  $f_2(\Pi) = 1 - \alpha\Pi$ , the nonlinear form  $f_2(\Pi) = (1 - \alpha\Pi)^\beta$ , the exponential form  $f_2(\Pi) = \exp(-\alpha\Pi)$  and the hyperbolic form  $f_2(\Pi) = 1 / (1 + \beta\Pi)$ .

The second type of representing the damage and the irradiation dose is that the coefficients of the function  $f_1(\varepsilon)$  taken from the above-mentioned dependencies are functions of the damage parameter and the irradiation dose. That is, the dependence can be taken as the following:

$$\sigma(\varepsilon, \Pi, \Phi) = A(\Pi, \Phi)\varepsilon^{m(\Pi, \Phi)}$$

$$\text{where } A(\Pi, \Phi) = \frac{A_0 [\gamma_1 - \alpha_1 \lg(\beta_1 \Phi)]}{(1 + A_1 \Pi)},$$

$$\text{and } m(\Pi, \Phi) = \frac{m_0 [\gamma_2 - \alpha_2 \lg(\beta_2 \Phi)]}{(1 + m_1 \Pi)}.$$

Or as  $\sigma = f(\varepsilon, \Phi) \cdot \tau(\Pi, \Phi)$ ,

$$\text{where } f(\varepsilon, \Phi) = f_1(\varepsilon) \cdot \exp(-\gamma\Phi) = f_1(\varepsilon)\chi(\Phi), \quad \tau = \exp(-\Pi).$$

Sometimes it is convenient to use the physical correlation in the form:  $\sigma(\varepsilon, \Phi, \Pi) = A(\Pi)\sigma^{\alpha(\Phi)} \exp[\lambda(\Phi) \cdot \Pi]$  where the kinetic equation of damage accumulation is as follows:

$$\frac{d\Pi}{dt} = B(\Phi) \left( \frac{\sigma}{1 - \Pi} \right)^{n(\Phi)}$$

If we take into consideration the swelling or deformation due to irradiation exposure, the following formula is used:

$$\sigma(\varepsilon, \Phi, \Pi) = A(\Phi)\sigma^{\alpha(\Phi)} \exp[\lambda(\Phi) \cdot \Pi] + \varepsilon_\Phi.$$

$\varepsilon_\Phi$  can be taken as

$$\varepsilon_\Phi = \begin{cases} 0, & \Phi < \Phi_{2nop} \\ \delta \cdot \varepsilon_{\max} [\exp(\nu \cdot (\Phi - \Phi_{2nop})) - 1] / [\varepsilon_{\max} + \delta \exp(\nu \cdot (\Phi - \Phi_{2nop}))], & \Phi \geq \Phi_{2nop} \end{cases}$$

where  $\varepsilon_{\max}$  is maximum radiation strain for the material,  $\delta, \nu$  are the empirical coefficients depending on the deformability of the material and radiation energy spectrum of the neutron flux.

## REFERENCES

- Овчинников И. Г., Матюра А. В., Нормова Г. А. Напряженно-деформированное состояние армированных элементов конструкций при воздействии радиационных полей. Саратов. Сарат. гос. техн. ун-т, 2004. 204 с.

## ARTEFACTS IN SEM: HYDROCARBON CONTAMINATION

**O. Chichvarina, V. Galushka, D. Bilenko**

Saratov State University

Scanning electron microscope (SEM) is one of the main instruments that provide a linear size of nanoscale objects, it is widely used to investigate the morphology while the availability of x-ray detectors allows researchers to carry out both qualitative and quantitative analysis of chemical elements with high locality in the surface layer of specimens. Recently, however, the problem of artefacts becomes more pervasive. The occurrence of the typical dark frame- or circle-like contamination marks during measurements in SEM and the distortion of the chemical composition of the surface layer of samples contribute to measurement errors. The main cause for such errors is hydrocarbon molecules in the chamber of the SEM, its walls, as well as the adsorbed by the surface of specimen, which are polymerized by the incoming (or outgoing) electrons and photons. This leads to the formation of carbon deposition on the specimen. During the time required to perform even a single measurement, the sample sizes may vary and the extent of these changes remain unknown unless the “mechanism” of hydrocarbon contamination formation is studied, and the appropriate technique of contamination monitoring or removal is found. Thereby, the primary goals of this research were to investigate the influence of the thickness of a thin electron transparent coating on the carbon film growth rate and to find the influence of the substrate material on the speed of carbon film formation.

To find out the dependence of the received data on the composition on the coating a silicon wafer alternately covered with three layers of gold (5nm, 10nm and 15 nm) was investigated by means of the SEM. The surfaces of these three layers (Au1, Au2 and Au3, respectively) area of  $1\mu\text{m} \times 1\mu\text{m}$  were scanned in turn by the energy dispersive X-ray microanalysis system INCA Energy SEM. The experiment included 10 measurements (2 min. for each measurement).

The quantitative content of carbon increases linearly in time (Table 1). The contents of Si and Au also change which is clear from the allowance for the finite depth of the electron beam interaction with the structure. Thus, the growth of carbon film on the specimen inhibits Au electrons emission from the surface, which is proved by the descent of gold concentrations over time (Fig. 1). This fact testify the distortion brought by the carbon contaminants into the data about the quantitative composition of specimen.

Judging from Fig.2. the deposition rate of carbon «carry-over» on the sample with golden covering does not depend on the thickness of the coating. An experiment to determine the rate of growth of the carbon film depending on the sample material was also performed. Si, Au and In wafers

with the area of  $1\mu\text{m} \times 1\mu\text{m}$  were bombarded with a 20 kV, 1,6 nA electron beam in the SEM for 20 minutes (2 min. for each measurement). Change over time in the read out carbon content of the wafers is shown in Fig. 3.

*Table 1*  
Quantitative changes in the composition of three golden layers covered on the silicon wafer (weight %)

	5nm golden covering			10nm golden covering			15nm golden covering		
	C	Au 1	Si	C	Au 2	Si	C	Au 3	Si
8,24	3,98	89,1	6,8	8,1	83,07	11,64	12,44	77,47	2
11,19	3,93	89,01	11,45	7,67	82,77	13,96	12,02	77,9	4
11,92	4	89,16	13,33	7,91	83,8	16,92	12,1	77,69	6
15,2	3,7	88,98	18,39	7,22	83,76	19,07	12,04	78,06	8
15,79	3,53	89,7	18,8	7,13	83,85	19,24	12,34	78,18	10
19,54	3,65	89,63	21,24	7,48	83,75	21,68	12,22	77,89	12
22,57	3,36	89,92	22,58	7,35	83,8	25,27	12	78,47	14
23,49	3,78	89,91	24,13	6,89	84,17	25,53	11,93	78,32	16
24,99	3,44	89,66	26,01	7,14	83,59	28,35	11,72	78,02	18
27,42	3,6	90,38	27,02	7,3	83,77	30,5	12,11	77,98	20

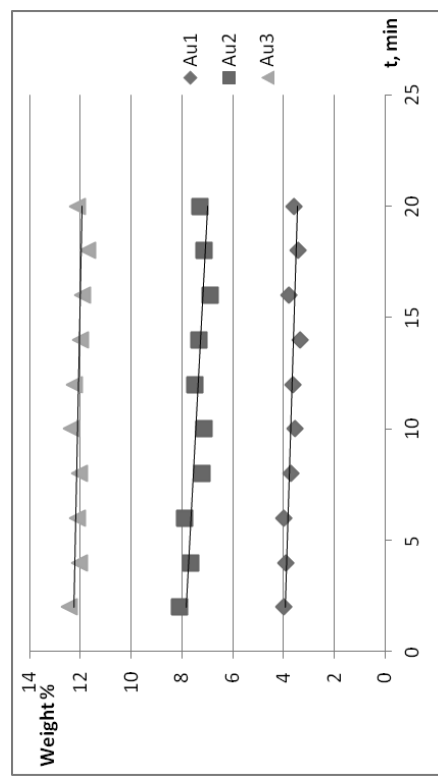


Fig.1. Descent of gold concentrations over time.

growth rate. The effect can be also explained with thermal conductivity of Si, Au and In. Perhaps, the substrates were heated during the experiment which provoked desorption of the carbon molecules from the specimen and decelerated the formation of carbon contamination.

In conclusion, Fig. 1 evidences the great contribution of the hydrocarbon contamination in the measurements on SEM. Carbon film formation modifies the morphology and leads to the errors in linear sizes as well as distorts the data on the composition of samples. The thickness of covering doesn't influence carbon film growth rate. The difference in the speed of carbon deposition growth depending on the substrate material allows us to suggest that specific covering would pretend the process of carbon film formation or delays it in such a way that it could be negligible. The further research of the process of carbon film formation is planned in order to offer the best way to deal with this problem.

#### REFERENCES

1. Egerton R.F. Radiation damage in the TEM and SEM // Micron. – 2004. – V 35. – p. 399-409
2. Larionov Yu. V. Effect of Sample Contamination in SEMs on Linear Size Measurements // Journal of Surface Investigation. X-ray, Synchrotron and Neutron Techniques. – 2008. – V 2. – N. 5. – p. 727-737
3. Goldstein J.I., Newberry D.E. Scanning Electron Microscopy and X-ray microanalysis / London Moscow, Kluwer Academic /Plenum Publishers. – 2003. – 689p.
4. Vane R. Environmental Contamination Sources and Control in High Resolution Scanning // XEI Scientific Inc. – 2005. – V 11. – p. 900-901.

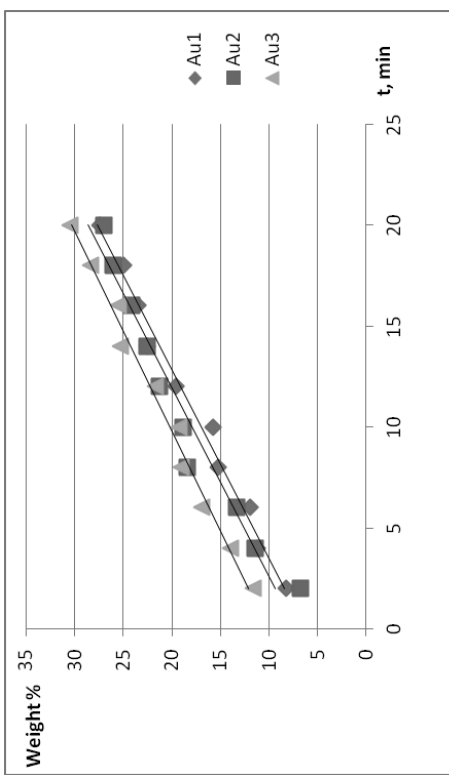


Fig. 2. Growth of carbon film on the silicon substrate with golden coating of different thicknesses

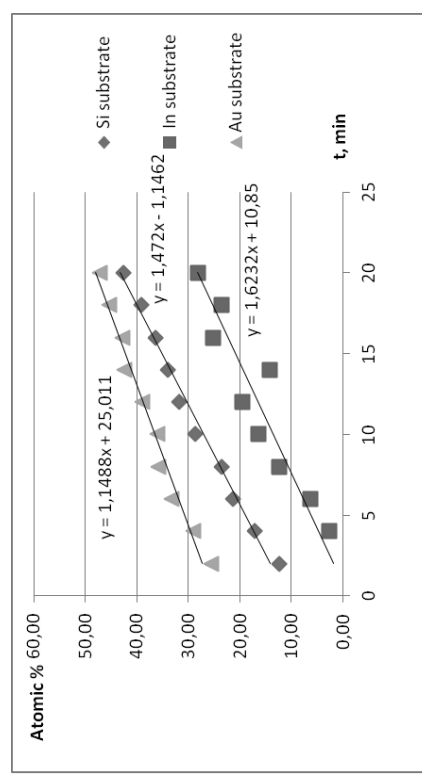


Fig. 3. Growth of carbon «carry-over» on the substrates of Si, Au, In

It can be assumed from this dependence that carbon deposition on the wafers with various compositions occurs at different speed but these differences are less pronounced in comparison with the initial content of carbon which is nonzero. Obviously, the substrates had already been contaminated before the exposure due to the adsorption processes which are typical for each material. Owing to different adsorption coefficients the wafers adsorb with different speeds; therefore, the initial value of C differs depending on the substrate material. Secondary electron coefficients may contribute to the carbon film

Saratov State University

#### Introduction

A major part of physical phenomena causing a keen interest of scientists can be researched using a computer modeling. This approach presents some difficulties in the case of complicated phenomena modeling (e.g., nonlinear phenomena), because it supposes a solving systems of stiff differential equations. The main problem is connected with the fact, that a solution (a mathematic function) is a smooth function, but is so fast changeable, that conventional methods like Runge-Kutta method in this way are nonoperability. To get a satisfactory result conventional methods require a very small

fluctuation of function arguments and not guaranty expectable accuracy [1]. Therefor in this way different implicit and prediction-correction methods [2] are widely used. But using such methods researcher can achieve high accuracy by essential computational speed decreasing. In many cases it's inadmissible step on the way to solve the problem.

Among of different numerical methods the Adams method [3] is well known. This method is suitable in the case of very complex dependency functions. In this case it is faster than Runge-Kutta method. But the Adams method, used a high order polynomials, is very slow and has no enough accuracy, because it loads computer resources on a preliminary stage.

All known methods of stiff differential equations systems solving has not enough accuracy, but works very fast in one way and they can have a hight accuracy and great time consuming in another way.

The mathematical problem of solving differential equations system can be stated in vector form as:

$$\frac{d\vec{Y}}{d\vec{X}} = \vec{F}(\vec{X}, \vec{Y}) \quad (1)$$

where  $\vec{Y}(y_1, y_2, \dots, y_M)$  is a column vector of objective function,  $\vec{X}(x_1, x_2, \dots, x_N)$  is a column vector of  $\vec{Y}$  function arguments. The most widely known method for the solution (1) is Runge-Kutta's method. But this method doesn't work since this equation has fast oscillation solutions. We propose to use Lagrangian interpolation in aggregate with Gauss-Christoffel quadrature formulas. In this section we describe proposing method in more details.

We will consider only one component of  $\vec{X}$ ,  $\vec{Y}$  and  $\vec{F}$  vectors, because a number of this vectors dimensions is not principally influence method algorithm. In this way we can formulate problem (1) in follow form as:

$$\frac{dy}{dx} = f(x, y(x)) \Rightarrow y(x) = \int_a^b f(x, y(x)) dx \quad (2)$$

Let's consider the right-hand side  $f(x, y(x))$  of the equation (2) not on the entire plane and its arguments  $x$  and  $y(x)$ , but only on certain integral curve  $y(x)$  corresponding to the desired solution. In this case, the function  $f(x, y(x))$  equals to the following equation:

$$F(x) \equiv f(x, y(x)) \quad (3)$$

The widely known method proposed by Adams constructs Newton interpolation  $n$ -order polynomials in the neighborhood of nodes  $y_i, \dots, y_{i+n}$ . In contrast to Adams method our method uses Lagrange interpolation polynomials. Of course, there are many situations in which Adams method is more desirable than Runge-Kutta method, but also it has a difficulty when  $n$  is greater than two. Using of Lagrange polynomials gives a significant gain in computational speed due to the following factors:

- no need to calculate the expansion coefficients of the polynomial at each iteration;
- no need to bring a polynomial to the canonical form by using quadrature formulas of Gauss-Christoffel.

Let's choose a certain grid  $\{x_N : a = x_0 < x_1 < \dots < x_N = b\}$  on the interval  $[a; b]$ . In this situation the equation (2) can be written as follows:

$$\frac{dy}{dx} = F(x) \quad (4)$$

At the each interval of selected mesh we will construct Lagrange interpolation polynomials, i.e. we will replace the right-hand side of expression (2) by formula (5).

$$F(x) \approx \sum_{j=0}^{N-1} F(x_j) l_j(x) \forall x \in [a; b] \quad (5)$$

where  $F(x_j) = const \forall x$  is the value of function  $F(x)$  in discrete counts  $x_j$ ,  $l_j(x) = \prod_{k=0, k \neq j}^n \frac{x - x_k}{x_j - x_k}$  is a basis polynomial in Lagrange polynomial expansion.

Taking into account equation (5) formula (4) can be presented in a form as:

$$y(x) = \sum_{j=0}^{N-1} \int_a^{a+(j+1)(b-a)/N} \sum_{j=0}^n F(x_j) l_j(x) dx = \sum_{j=0}^{N-1} \sum_{j=0}^n F(x_j) l_j(x) \quad (6)$$

To calculate the element of integration (6) we use quadrature formulas of Gauss-Christoffel. The resulting equation corresponds to the Gauss formula with weight  $p(x) = 1$ . Using a linear transformation of arguments we can rewrite bounders of integral (6) to segment  $[-1; 1]$ . On this segment Legendre polynomials are orthogonal with the unit weight. Let's mark nodes of Legendre polynomials as  $\xi_k$  and weight as  $\gamma_k$ . Using inverse linear transformation (7) we can calculate nodes and weights for every segment  $[q; p]$ .

The widely known method proposed by Adams constructs Newton interpolation  $n$ -order polynomials in the neighborhood of nodes  $y_i, \dots, y_{i+n}$ . In contrast to Adams method our method uses Lagrange interpolation polynomials. Of course, there are many situations in which Adams method is more desirable than Runge-Kutta method, but also it has a difficulty when  $n$  is greater than two. Using of Lagrange polynomials gives a significant gain in computational speed due to the following factors:

- no need to calculate the expansion coefficients of the polynomial at each iteration;
- no need to bring a polynomial to the canonical form by using quadrature formulas of Gauss-Christoffel.

Let's choose a certain grid  $\{x_N : a = x_0 < x_1 < \dots < x_N = b\}$  on the interval  $[a; b]$ . In this situation the equation (2) can be written as follows:

$$y(x) = \sum_{i=0}^{N-1} \int_{a+i(b-a)/N}^{a+(i+1)(b-a)/N} F(x) dx \quad (4)$$

At the each interval of selected mesh we will construct Lagrange interpolation polynomials, i.e. we will replace the right-hand side of expression (2) by formula (5).

$$F(x) \approx \sum_{j=0}^{N-1} F(x_j) l_j(x) \forall x \in [a; b] \quad (5)$$

where  $F(x_j) = const \forall x$  is the value of function  $F(x)$  in discrete counts  $x_j$ ,  $l_j(x) = \prod_{k=0, k \neq j}^n \frac{x - x_k}{x_j - x_k}$  is a basis polynomial in Lagrange polynomial expansion.

Taking into account equation (5) formula (4) can be presented in a form as:

$$y(x) = \sum_{j=0}^{N-1} \int_{a+i(b-a)/N}^{a+(i+1)(b-a)/N} \sum_{j=0}^n F(x_j) l_j(x) dx = \sum_{j=0}^{N-1} \sum_{j=0}^n F(x_j) l_j(x) \quad (6)$$

To calculate the element of integration (6) we use quadrature formulas of Gauss-Christoffel. The resulting equation corresponds to the Gauss formula with weight  $p(x) = 1$ . Using a linear transformation of arguments we can rewrite bounders of integral (6) to segment  $[-1; 1]$ . On this segment Legendre polynomials are orthogonal with the unit weight. Let's mark nodes of Legendre polynomials as  $\xi_k$  and weight as  $\gamma_k$ . Using inverse linear transformation (7) we can calculate nodes and weights for every segment  $[q; p]$ .

$$x_k = \frac{1}{2}(p+q) + \frac{1}{2}(q-p)\xi_k \quad (7)$$

$$c_k = \frac{1}{2}(q-p)\gamma_k$$

Taking into account equation (7) the element of integration (6) can be presented in follow form as:

$$\int_p^q l_i(x)dx \approx \sum_{k=1}^M c_k l_i(x_k) = \frac{q-p}{2} \sum_{k=1}^M \gamma_k l_i\left(\frac{p+q}{2} + \frac{q-p}{2}\xi_k\right) \quad (8)$$

Nodes  $\xi_k$  of Legendre polynomials can be found using numerical methods of one-dimensional optimization. Weights  $\gamma_k$  can be calculated by the next equation:

$$\gamma_k = \frac{1}{P'_M(\xi_k)} \int_{-\xi_k}^{\xi_k} P_M(\chi) d\chi \quad (9)$$

It should be noted, that nodes  $\xi_k$  and weights  $\gamma_k$  are calculated on a preliminary stage, and in the main program we use this numbers like constants. Therefore it has not influence on the numerical calculation speed.

As a result, taking into account equations (4) – (8), we have the final formula for calculating the integral equation (2).

$$y(x) = \sum_{i=0}^N \sum_{j=0}^n F(x_j) \frac{(b-a)}{2N} \sum_{k=1}^M \gamma_k l_j\left(\frac{2a+(2i+1)(b-a)/N}{2} + \frac{b-a}{2N}\xi_k\right) \quad (10)$$

The accuracy of proposed method is determined by quadrature formulas precision and a quality of Lagrange polynomials approximation of an integral curve.

#### Results and discussion

The efficiency of the proposed algorithm was tested on the classical system of stiff differential equations.

$$\begin{cases} \frac{dy_1}{dx} = -2y_1 - 998y_2; \\ \frac{dy_2}{dx} = -1000y_2. \end{cases} \quad (11)$$

One can see that the exact solution of this system of differential equations has the form as:

$$y_1(x) = e^{-2x} + e^{-1000x}, \quad (12)$$

$$y_2(x) = e^{-1000x}. \quad (13)$$

When we solve this problem using fourth-order Runge-Kutta method, some difficulties arises because solution has two terms which vary at different speeds: the first term  $e^{-1000x}$  decreases very fast and second  $e^{-2x}$  changes slowly. As a result we have the follow misalignment (on segment  $[0; 0.1]$  with 1000 steps):

$$\max_{PK4}(\delta y_1(x=0.1), \delta y_2(x=0.1)) = 4.16 \cdot 10^{-2} \sim 10^{-2}$$

The second solution was found using proposed method. We have used same segment  $[0; 0.1]$  with 1000 steps. The result is follow:

$$\max(\delta y_1(x=0.1), \delta y_2(x=0.1)) = 5.11 \cdot 10^{-6} \sim 10^{-6}$$

On the base of this results we can note, that proposed method has visible growing of calculation efficiency.

We created a program on python programming language that implements the algorithm described above and collected results of comparison with Runge-Kutta method on the system (11) into table I below.

Table Results of methods comparison

Precision	Runge-Kutta method			Proposed method		
	Number of steps	Time consumption (ms)	Number of steps	Time consumption (ms)	Time consumption acceleration	
0.000100	400000	6200	50	4	1550	
0.000025	1600000	24000	200	18	1333	
0.000014	2800000	43000	350	31	1387	
0.000010	4000000	61000	500	43	1418	

In table time consumption acceleration parameter describes how many times the proposed method is faster than Runge-Kutta method. It was calculated for a few precisions.

As we can see, the proposed method is about thousand times faster than Runge-Kutta in the case of our example. This acceleration lets us efficiency use this method for more complicated problems related to stiff differential equations.

## Conclusion

In this paper the method of solving differential equations systems was proposed. This method creation was motivated by a desire to improve conventional methods, which gives unacceptable results for stiff differential equations. The method algorithm was obtained and presented. The efficiency of method was confirmed by results of comparing with Runge-Kutta method. The developed method will be used in the calculation of nonlinear effects that occur in periodic electrodynamics structures.

## REFERENCES

1. *Mydrov A. E.* Numerical methods for PC on Basic, Fortran and Pascal languages. Tomsk: MP Rasko, 1991
2. *Kalitkin N. N.* Numerical methods. St. Petersburg : BHV, 2011
3. *Samarsky A. A.* Introduction to Numerical Methods. Moscow : Lan, 2009.
4. *More J. J., Cosnard M. Y.* Numerical Solution of Nonlinear Equations // ACM Transactions on Mathematical Software. Vol. 5. № 1. March. 1979. P. 64–85.

## DISTRIBUTION OF THE LOCAL STRESS OF ATOMIC MONOLAYER GRAPHENE

*O. E Glukhova, I. V. Kirillova, V. V. Shumayev*

Saratov State University, Saratov

Graphene is a two-dimensional allotropic modification of carbon. It has a unique local sorption, electrical, transport and mechanical properties, which makes it a promising nanomaterial for electronics, especially for flexible transparent electronics. The application of graphene in the design of flexible displays requires a preliminary study of the influence of strain on its atomic and electronic structure.

At present, scientists experimentally study strain compression, tension, flexure of one- and two-layer graphene, and measure force constants (Young's modulus, Poisson's ratio) [1, 2]. In this study the deformation of nanoscale objects requires high tech equipment that makes such experiments rare and unique. But often a costly experiment can be replaced by a numerical-analytical modeling and numerical experiment, which is carried out by using molecular dynamics.

This work is devoted to theoretical investigation of deformation of monolayer graphene using an empirical model of graphene and the theory of stability of nanoplates, including the development of methods for calculating the distribution of local stress nuclear monolayer graphene.

1. Molecular and mechanical model of graphene. Young's modulus. Theoretical basis of the empirical model is a valence force field with the interaction of van der Waals unbound atoms. The total energy  $E_{\text{tot}}$  of a finite graphene sheet is a polynomial each component of which has a weighting factor, determined by processing experimental data:

$$E_{\text{tot}} = \sum K_r (r - r_0)^2 + \sum K_\theta (\theta - \theta_0)^2 + \sum \left( \frac{K_a}{r^{12}} - \frac{K_b}{r^6} \right) \quad (1)$$

The first term takes into account changes in bond lengths in the nanostructure with respect to the bond length in graphite ( $r_0 = 1.42 \text{ \AA}$ ), the second – the change in the bond angles with respect to the angle between the bonds in graphite ( $\theta_0 = 120^\circ$ ), and the third – the interaction of van der Waals (Lennard-Jones),  $K_r, K_\theta, K_a, K_b$  – weight coefficients. This way of defining the total energy of nanostructures has been selected as one of the best. It is known that the more complex form of the polynomial that gives total energy, the greater the number of unknown weight coefficients and, consequently, the more difficult and ambiguous the process of parametrization will be (search of weight coefficients).

The weight coefficients are the solution to the minimax problem with constraints with values in the following statement:

$$\min_{\mathbf{A}} \max S(\mathbf{A}), \quad \text{rDE } S(\mathbf{A}) = \sum_{i=1}^3 |r_i - r_i^0|, \quad (2)$$

where  $\{r_i\}$  – the set of C-C bond lengths,  $\{r_i^0\}$  – the set of known (calculated or experimental) values,  $\mathbf{A} = (K_r, K_\theta, K_a, K_b)$  – the vector of variable parameters. To find the global minimum, surface of the objective function was built for each set, and base point shifted hence its profile. Set  $\{r_i\}$  was found by minimizing the total energy (1) of the nanotube to the coordinates of all atoms. As the known values of  $\{r_i^0\}$  experimental and theoretical data on the geometric dimensions and bond lengths of nanotubes were taken.

The solution of the minimax problem (2) gave the following weighting factors [3]:

$$\begin{aligned} K_r &= 3,25 \cdot 10^2 \frac{\partial \mathcal{E}}{\partial r^2}, K_\theta = 4,4 \cdot 10^{-19} \frac{\partial \mathcal{E}}{\partial \theta^2}, K_a = \\ &= 4,0 \cdot 10^{-139} \frac{\partial \mathcal{E}}{\partial r^{12}}, K_b = 1,5 \cdot 10^{-80} \frac{\partial \mathcal{E}}{\partial r^6}. \end{aligned} \quad (3)$$

A modified empirical model allows calculating the atomic magnetic structure of carbon clusters with satisfactory accuracy: the error is less than 3%. Young's modulus is determined by  $E = T / S \cdot (L / \Delta L)$  where the force of tension (compression)  $T$  is calculated by binding energy of the elastic tension

(compression)  $\Delta E$ :  $\Delta E = T \cdot \Delta L / 2$ ;  $L$  – length of the undeformed atomic frame,  $\Delta L$ -lengthening of the frame. The area  $S$  is calculated as the area of the edge width of 3,4 Å (the distance between the layers of graphite).

## 2. Method for calculating local stresses nuclear skeleton

A single-layer graphene sheet is represented as a nanoplate with orthotropy of mechanical properties. To calculate the distribution of local power grids of atomic-layer graphene we apply the theory of stability for plates. Deflection function  $w$  has the form [4]:

$$D_1 \frac{\partial^4 w}{\partial x^4} + 2D_3 \frac{\partial^4 w}{\partial x^2 \partial y^2} + D_2 \frac{\partial^4 w}{\partial y^4} = -T_x \frac{\partial^2 (w_0 + w)}{\partial x^2}, \quad (4)$$

where  $T_x$  – force attached to the body along the  $x$  axis (the efforts along the  $y$  and  $z$  are absent,  $T_y = T_z = 0$ ),  $w_0$  – the initial function of deflection,  $D_1, D_2, D_3$  – stiffnesses, calculated by these formulas:

$$D_1 = \frac{E_1 h^3}{12(1 - \vartheta_1 \vartheta_2)}, D_2 = \frac{E_2 h^3}{12(1 - \vartheta_1 \vartheta_2)}, D_3 = D_{12} + 2D_{66} = 9_2 D_1 + \frac{G h^3}{12}, \quad (5)$$

where  $E_1$  and  $E_2$  – Young's modulus along the axes of  $x$  and  $y$ ,  $\vartheta_1$  and  $\vartheta_2$  – Poisson's ratios in the directions  $x$  and  $y$ ,  $G$  – shear modulus,  $h$  – the plate thickness.

We consider the stability of a rectangular plate size  $a \times b$ , compressed in the direction  $X$ . In this case, the boundary conditions take the form:

$$\begin{cases} x = 0, x = a, w = 0, M_x = 0 \\ y = 0, y = b, w = 0, M_y = 0 \end{cases}, \quad (6)$$

where  $M_x$  and  $M_y$  – the main moments about  $x$  and  $y$  axes.

We will find the deflection function in the following form:

$$w(x, y) = F \sin \frac{\pi x}{a} \sin \frac{\pi y}{b}, \quad (7)$$

The initial function is similar:

$$w_0(x, y) = F_0 \sin \frac{\pi x}{a} \sin \frac{\pi y}{b}. \quad (8)$$

$F$  and  $F_0$  correspond to features of function in the middle of the plates. By substituting (7) and (8) in (4) we get:

$$(D_1 \frac{\pi^4}{a^4} + 2D_3 \frac{\pi^4}{a^2 b^2} + 2D_2 \frac{\pi^4}{b^4})F = T_x [F_0 + F] \frac{\pi^2}{a^2}. \quad (9)$$

Transforming this expression and introducing a new constant  $D = \pi^2 [D_1 \frac{1}{a^2} + 2D_3 \frac{1}{b^2} + D_2 \frac{a^2}{b^4}]$ , we obtain an expression for a parameter  $F$ :

$$F = \frac{T_x F_0}{D - T_x}. \quad (10)$$

Deflection function can be written as:

$$w = \frac{T_x F_0}{D - T_x} \sin \frac{\pi x}{a} \sin \frac{\pi y}{b}. \quad (11)$$

The normal stresses  $\sigma_1$  on the  $x$  direction at each point of the plate surface (i.e. in the vicinity of each atom graphene) is given by:

$$\sigma_1 = -\frac{6D_1}{h^2} \left( \frac{\partial^2 w}{\partial x^2} + 9_1 \frac{\partial^2 w}{\partial y^2} \right). \quad (12)$$

By substituting (11) into (12) we obtain the final formula for the stresses:

$$\sigma_1 = \frac{6D_1}{h^2} \frac{T_x F_0}{D - T_x} \sin \frac{\pi x}{a} \sin \frac{\pi y}{b} \left( \frac{\pi^2}{a^2} + 9_1 \frac{\pi^2}{b^2} \right) \quad (13)$$

Let us consider a small graphene fragment with 78 atoms shown at Fig. 1.

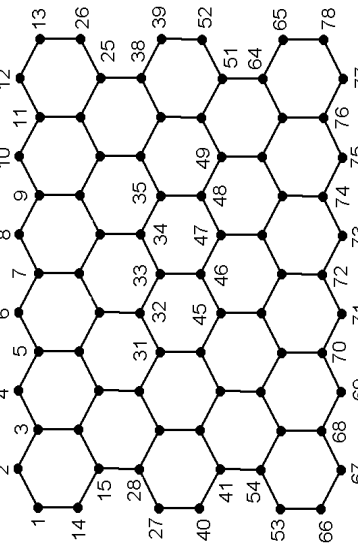


Fig. 1. Graphene fragment

Graphene sheet has the following geometric dimensions: length along the direction  $X$   $a=66,42$  Å; length  $b=19,88$  Å; thickness of nanoplate is taken as  $h=3,4$  Å. Calculated by using the molecular-mechanical model of graphene

(see Section 1) Young's moduli are  $E_1 = 0.99$  TPa,  $E_2 = 0.81$  TPa, Poisson's ratios are  $\vartheta_1 = 0.27$ ,  $\vartheta_2 = 0.2$ . Our computed elastic parameters are well agreed with experimental data and alternative calculations: the Young modulus are about 1 TPa [3], Poisson's ratio 0.12-0.413 [5].

According to the calculated elastic parameters, stiffness of the graphene sheet are defined:  $D_1 = 2.79$  TPa\* $\text{\AA}^3$ ,  $D_2 = 3.06$  TPa\* $\text{\AA}^3$ ,  $D_3 = 2.64$  TPa\* $\text{\AA}^3$ ,  $D=0.8$ . nN. The initial strain is absent, consequently  $F_0 = 1$ .

For the deformed sheet subjected compressed by 5% in the direction of X, we calculated the distribution of local stresses near each atom using the formula (13), which can be written as:

$$\sigma_1 = S \sin \frac{\pi x}{a} \sin \frac{\pi y}{b} \quad (14)$$

where  $F_0 = 1$  For the such strain force is  $T_x = 1.98$  nN,  $S=1.49$  TPa. Value of stresses near each atom can be found by substituting its coordinates in (14). We calculated not absolute but relative importance of local stress  $\sigma^* = \frac{\sigma}{S}$ . Distribution of this quantity over the atoms of graphene allows to suggest which atoms can be eliminated from the graphene sheet. Figure 2 shows the distribution of atoms.

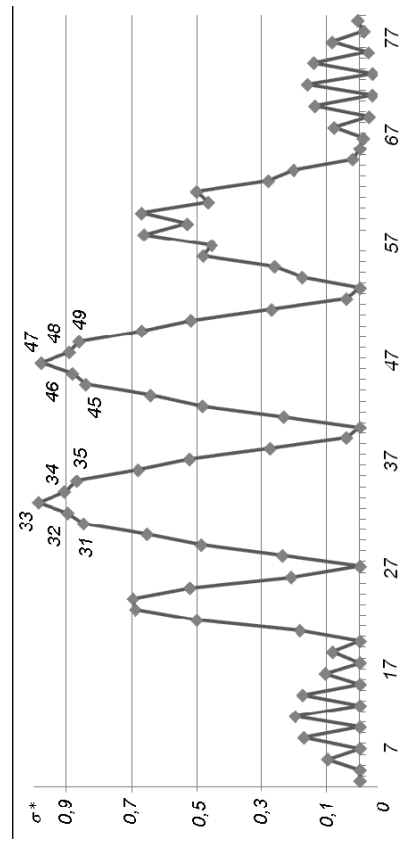


Fig. 2. Dependence on atomic number

## REFERENCES

1. *Otakar Frank, Georgia Tsoukleris, John Parthenios, Konstantinos Papagelis, Ihsam Riaz, Rashid Jalil, Koshy S. Novoselov, and Costas Galiotis. Compression Behavior of Single-Layer Graphenes / / ACS NANO. – VOL. 4 • NO. • 3131-3138 • June 2010.*
2. *Changgu Lee, Xiaodong Wei, Jeffrey W Kysar, James Hone. Measurement of the Elastic Properties and Intrinsic Strength of Monolayer Graphene // SCIENCE – VOL. 321 18 JULY 2008.*
3. *Glukhova O.E. Rigidity of Y-shaped carbon nanotubes during deformation tension / compression / Nano and Microsystem Technology. – 2009. – № 1. – S. 19-22.*
4. *Lechnický SG. Theory of Elasticity of an Anisotropic Body. Moscow: Nauka, 1977*

- of Single-Layer Graphenes / / ACS NANO. – VOL. 4 • NO. • 3131-3138 • June 2010.
2. *Changgu Lee, Xiaodong Wei, Jeffrey W Kysar, James Hone. Measurement of the Elastic Properties and Intrinsic Strength of Monolayer Graphene // SCIENCE – VOL. 321 18 JULY 2008.*
  3. *Glukhova O.E. Rigidity of Y-shaped carbon nanotubes during deformation tension / compression / Nano and Microsystem Technology. – 2009. – № 1. – S. 19-22.*
  4. *Lechnický SG. Theory of Elasticity of an Anisotropic Body. Moscow: Nauka, 1977*

## SIMULATION OF THE FULLERENES FILLED NANOTUBES BENDING

**O. E. Glukhova, A. S. Kolesnikova**

*Saratov State University*

Currently, we are investigating the processes of polymerization of fullerenes carbon nanotubes. There are known methods of fullerenes polymerization in the peapod under the influence of pressure, temperature and when between neighboring fullerenes the carbon atoms are added. It is shown (M. Chorro, J. Cambedouzou, A. Iwasiewicz-Wabnig, L. Noe, S. Rols, M. Monthoux, B. Sundqvist, P. Launois) that the C<sub>60</sub> fullerenes polymerization in the peapod at the pressure of 1.5 GPa and the temperature of 300 °C, and between C<sub>70</sub> fullerenes polymerization process is not observed. It is shown (S. Kawasaki, T. Hara, T. Yokoma, F. Okino, H. Touhara, H. Kataura, T. Watanuki, Y. Ohishi, 2006) that the polymerization process between the C<sub>60</sub> is under pressure without any temperature. The initial distance between the centers of fullerenes is 0.956 nm, and under the pressure of 25 GPa, the distance between the centers of fullerenes is reduced to 0.845 nm. This value corresponds to the distance of 0.145 nm between the nearest neighboring carbon atoms of fullerenes. Consequently, the chemical reaction and the polymerization process occur. It is shown (In-Ho Lee, S. Jun, H. Kim, S.Y. Kim, Y. Lee, 2006) that the C<sub>60</sub> fullerenes, which have the defect SW in its structure (Stone-Wels's defect is a defect, based on the turning of the longitudinal bond) and are located at the distance of 0.99 nm, begin to approach to each other and have the form the C<sub>120</sub> structure, when a carbon atom is added. The polymerization process can occur between the C<sub>20</sub> fullerenes in the nanotube closed with both ends at the pressure of 5 GPa, which is carried by C<sub>60</sub> fullerene (Glukhova O.E., 2009).

In this work we have investigated theoretically the bending effect on the polymerization process in the peapod with the C<sub>60</sub> fullerenes using two methods: the empirical method, which is well-proved in the study of hardness and elasticity of the complex forms nanotubes, and the tight-binding method,

which is the quantum-mechanics method (O.E. Glukhova, I.N. Saliy, R.Y. Zhnichkov, I.A. Khvatov, A.S. Kolesnikova, M.M. Slepchenkov, 2010).

The total energy of carbon tubular nanostructure is defined by the empirical, molecular-mechanical model as a polynomial, whose components have their weight coefficient.

$$E_{tot} = \sum k_r (r - r_0)^2 + \sum k_\theta (\theta - \theta_0)^2 + \sum \left( \frac{k_a}{r^{12}} - \frac{k_b}{r^6} \right) \quad (1)$$

Here the first term takes into account the change of the binding length in the nanostructure in the relation of the binding length in the graphite ( $r_0 = 1.42\text{\AA}$ ), the second term – the change of angles between the bindings in the relation of the angle between the bindings in the graphite ( $\theta = 120^\circ$ ), and the third term – van der Waals interaction (Lennard-Jones potential),  $K_r$ ,  $K_\theta$ ,  $K_a$ ,  $K_b$  – weight coefficients.

The total energy of the system is determined by the tight-binding method calculated as

$$E_{tot} = E_{bond} + E_{rep} \quad (2)$$

Here the term  $E_{bond}$  is the bond structure energy that is calculated as the sum of energies of the single particle occupied states,  $E_{rep}$  – the repulsive energy that is a repulsive potential.

The model peapod is formed by the nanotube (10,10) with the length of 2.44 nm, filled with 27 the C<sub>60</sub>. The C<sub>60</sub> molecules are situated at the distance of 0.339 nm from the tube wall. Fullerenes are on the tube axis at the distance equal to 0.815 nm. The distance decrease between the C<sub>60</sub> is observed at the peapod bending of 270 degrees.

The moment of the overlap of C<sub>60</sub> fullerenes electron clouds is fixed at the distance of 0.14–0.16 nm. As the result, C<sub>60</sub> fullerenes are polymerized, when the distance is sufficient to overlap π-electron clouds. The deformation of the structure is observed. The peapod surface of a smaller radius becomes wavy-like by an external force. To change the framework of a peapod there is a chemical interaction between fullerenes and the framework. Figure 2 shows the fragment of the peapod after the polymerization process. If the structure is not held by the both ends after the polymerization it remains in the same condition. Consequently, the process of polymerization is possible at the peapod bending of 270 degrees.

So, it was established that at such a bending:

1. The atomic structure of peapod is not destroyed.
2. The nanotubes surface of a smaller radius becomes wavy-like and is connected with the fullerenes in some places of trough.
3. The fullerenes approach to the distance of 0.14 nm between the atoms of the cell and are polymerized.
4. The formed hybrid compound of the nanotube, which was formed, retains the atomic structure unchanged even when there is no external load.

## REFERENCES

1. M. Chorro, J. Cambedonou, A. Iwasiewicz-Wabnig, L. Noe, S. Rolz, M. Monthoux, B. Sundqvist and P. Launois, Discriminated structural behaviour of C60 and C70 peapods under extreme conditions// A letters journal exploring the frontiers of physics, 2007 Volume 79, Number 5, p.56003
2. Ghikhova O.E. Rigidity Y-Shaped Carbon Nanotube at Stretching/Compression Deformation// Nanotechnology news 2009 V1
3. S. Kawasaki, T. Hara, T. Yokomae, F. Okino, H. Tokhara, H. Kataura, T. Watanuki, Y. Ohishi, Pressure-polymerization of C60 molecules in a carbon nanotube// Chemical Physics Letters, 2006, V.418,p. 260-263
4. In-Ho Lee, S. Jun, H. Kim, S.Y. Kim, Y. Lee, Addatom-assisted structural transformations of fullerenes// Applied physics letters, 2006,V.88, p. 011913

## CALCULATION OF BENDING AND ELASTIC PROPERTIES OF MONOLAYER GRAPHENE

**O. E. Glukhova, S. S. Vetsel**

Saratov State University

Modern science keeps developing. Every day scientists create new materials. One of them is graphene, which was first obtained in 2004. Graphene is a two-dimensional modification of carbon, formed by a layer of carbon atoms one

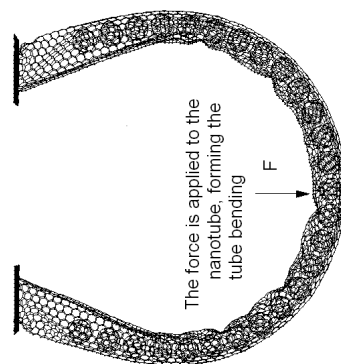


Fig 1. The peapod bending of 270 degrees

atom thick, connected by  $sp^2$  bonds in the two-dimensional hexagonal lattice. Elastic properties of graphene are not yet well understood. For waves of graphene of relatively large size (about 1.5 microns) Young's modulus was found (about 1 TPa), but not found rigidity. Also, the equation of the deflection of graphene was not obtained. Graphene has great potential if used in nanotechnology, because its Young's modulus is 5 times greater than the Young's modulus of steel. The aim of our study was to determine under the load the stiffness and construction of the deflection of graphene nanoplate consisting of 432 carbon atoms by the method of linear combination of atomic orbitals.

#### A mathematical model of the bending of thin plates

We consider a plate as an elastic body bounded by two parallel planes. We refer to the plate coordinate system, which is chosen as follows: xy-plane is compatible with the median plane and the z axis is perpendicular.

The problem of bending of thin plates can be considered as an ordinary three-dimensional problem of elasticity theory. However, the general solution of the basic system of elasticity theory still could not be obtained. Therefore, all the elasticity problems are divided into classes, each of which due to the introduction of simplifying hypotheses is possible to obtain an approximate solution of problems. One of them is the class of problems of bending of thin plates. The problem of equilibrium plate clamped at the edges was declared as a subject of the Paris Academy of Sciences in 1850. Kirchhoff in 1850 was the first to formulate the approximate theory of bending of thin plates built on two assumptions:

1. Line segments, which in the undeformed state plates were normal to its flat middle surface bending remains straight and normal to the curved surface of the median (the hypothesis of direct normals) and does not change its length.

2. Normal stress  $\sigma_z$  in sections parallel to the median plane, is a small quantity compared with the stresses in the cross-sections –  $\sigma_x, \sigma_y, \tau_{xy}$  (top three stresses).

We introduce the basic system of elasticity theory.

Equilibrium equation:

$$\begin{cases} \frac{\partial \sigma_x}{\partial x} + \frac{\partial \tau_{xy}}{\partial y} + \frac{\partial \tau_{xz}}{\partial z} = 0 \\ \frac{\partial \tau_{xy}}{\partial x} + \frac{\partial \sigma_y}{\partial y} + \frac{\partial \tau_{yz}}{\partial z} = 0 \\ \frac{\partial \tau_{xz}}{\partial x} + \frac{\partial \tau_{yz}}{\partial y} + \frac{\partial \sigma_z}{\partial z} = 0 \end{cases}$$

where  $\sigma_x, \sigma_y$  – the principal stresses,  $\tau_{xy}$  – shear stress.

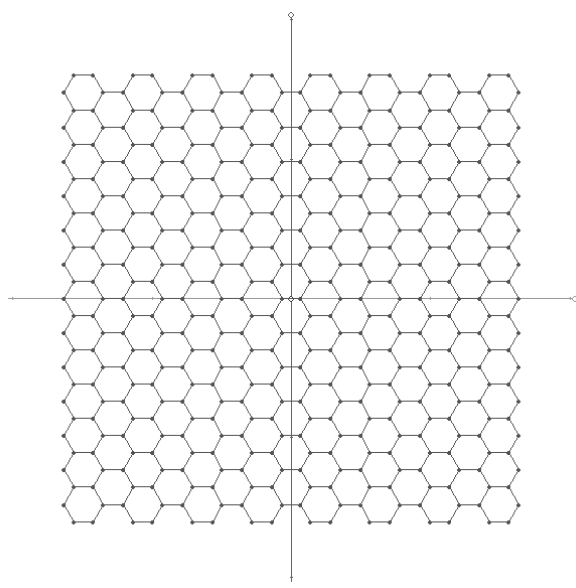


Fig. 1. The structure of graphene plate

The equations of Hooke's law:

$$\begin{cases} \varepsilon_x = a_{11} \sigma_x + a_{12} \sigma_y + a_{13} \sigma_z + a_{16} \tau_{xy} \\ \varepsilon_y = a_{12} \sigma_x + a_{22} \sigma_y + a_{23} \sigma_z + a_{26} \tau_{xy} \\ \varepsilon_z = a_{13} \sigma_x + a_{23} \sigma_y + a_{33} \sigma_z + a_{36} \tau_{xy} \\ \gamma_{yz} = a_{44} \tau_{yz} + a_{45} \tau_{xz} \\ \gamma_{xz} = a_{45} \tau_{yz} + a_{55} \tau_{xz} \\ \gamma_{xy} = a_{16} \sigma_x + a_{26} \sigma_y + a_{36} \sigma_z + a_{66} \tau_{xy} \end{cases}$$

Here  $a_{11}, a_{12}, \dots, a_{66}$  – elastic constants (the coefficients of deformation),  $\square$  – relative deformation along the main diagonal of the hexagonal lattice of graphene,  $\square_x$  – relative deformation along the diagonal perpendicular to the main diagonal of the hexagonal lattice of graphene,  $\square_{xy}$  – relative shift.

On the basis of the second hypothesis of Kirchhoff equations of Hooke's law  $\sigma_z$  can be set equal to zero. In this case, Kirchhoff considered two of the first and sixth equations:

$$\begin{cases} \varepsilon_x = a_{11} \sigma_x + a_{12} \sigma_y + a_{16} \tau_{xy} \\ \varepsilon_y = a_{12} \sigma_x + a_{22} \sigma_y + a_{26} \tau_{xy} \\ \gamma_{xy} = a_{16} \sigma_x + a_{26} \sigma_y + a_{66} \tau_{xy} \end{cases}$$

This system can be regarded as a system of three algebraic equations for  $\sigma_x, \sigma_y, \tau_{xy}$ . Solving it, we get:  
 $\sigma_x = (a_{22} a_{66} - a_{26} a_{26}) \varepsilon_x + (a_{26} a_{16} - a_{12} a_{66}) \varepsilon_y + (a_{12} a_{26} - a_{16} a_{22}) \gamma_{xy}$ .

Similar equations are obtained for  $\bar{\sigma}_{ij}, \tau_{ij}$ . If we put:

$$B_{11} = \frac{(a_{22} a_{66} - a_{26} a_{26})}{\Delta};$$

$$B_{12} = \frac{(a_{26} a_{16} - a_{12} a_{66})}{\Delta};$$

$$B_{16} = \frac{(a_{12} a_{26} - a_{16} a_{22})}{\Delta};$$

( $B_{ij}$  called the reduced coefficient of deformation), then we can write that  
 $\begin{cases} \sigma_x = B_{11} \varepsilon_x + B_{12} \varepsilon_y + B_{16} \gamma_{xy} \\ \sigma_y = B_{12} \varepsilon_x + B_{22} \varepsilon_y + B_{26} \gamma_{xy} \\ \tau_{xy} = B_{16} \varepsilon_x + B_{26} \varepsilon_y + B_{66} \gamma_{xy} \end{cases}$

Let us introduce new constants:

$$D_{ij} = B_{ij} \frac{h^3}{12}, \quad (i,j = 1,2,6).$$

Constant  $D_{ij}$  called stiffness.  $D_{11}$  and  $D_{22}$  bending stiffness relative to the axes OY and OX, respectively,  $D_{66}$  torsional rigidity,  $h$  – thickness of plate.

As a result, we obtain:

$$\begin{aligned} D_{11} \frac{\partial^4 w}{\partial x^4} + 4D_{16} \frac{\partial^4 w}{\partial x^3 \partial y} + 2(D_{12} + 2D_{66}) \frac{\partial^4 w}{\partial x^2 \partial y^2} + 4 D_{26} \frac{\partial^4 w}{\partial x \partial y^3} + \\ + D_{22} \frac{\partial^4 w}{\partial y^4} = 0^{[2]}. \end{aligned}$$

– basic differential equation of the theory of bending of thin anisotropic plates, where  $q(x,y)$  – acting on the plate load,  $W = W(x,y)$  – a function of deflection plates.

Graphene has two different Young's modulus in the direction of the axes Ox and Oy, which means it can be considered as an orthotropic material. Orthotropic material is a material in which at each point there are three planes of elastic symmetry. Let the three planes of elastic symmetry coincide with the

coordinate planes, then  $a_{16} = a_{26} = 0$ . We simplify the basic differential equation of the theory of bending of thin plates.  $\square$

You can introduce technical constants:  $\square$

$$a_{11} = 1/E_1, \quad a_{22} = 1/E_2, \quad a_{12} = -\frac{\vartheta_1}{E_1} = -\frac{\vartheta_2}{E_2}, \quad a_{66} = 1/G,$$

where  $E_1$  – Young's modulus along the axis Ox,  $E_2$  – Young's modulus along the axis Oy,  $\vartheta_1, \vartheta_2$  – Poisson's ratios along the axes Ox, Oy, respectively, and  $G$  – Young's modulus of the second kind.  $\square$

$$\begin{aligned} E_i &= \frac{24U}{\varepsilon^2 Fl} \\ G &= \frac{E}{2(1+\nu)} \\ B_{11} &= a_{22}/(a_{11}a_{22} - a_{12}^2) = E_1/(1 - \vartheta_1\vartheta_2) \\ B_{22} &= E_2/(1 - \vartheta_1\vartheta_2) \\ B_{12} &= \vartheta_1 E_2/(1 - \vartheta_1\vartheta_2) = \vartheta_2 E_1/(1 - \vartheta_1\vartheta_2) \\ B_{16} &= B_{26} = 0 \\ B_{66} &= 1/a_{66} = G \\ D_{22} &= \frac{E_2 h^3}{12(1-\vartheta_1\vartheta_2)} = D_2 \\ D_{12} &= \frac{\vartheta_1 E_2 h^3}{12(1-\vartheta_1\vartheta_2)} = \frac{\vartheta_2 E_1 h^3}{12(1-\vartheta_1\vartheta_2)} \\ D_{16} &= D_{26} = 0 \\ D_{66} &= \frac{G h^3}{12} = D_k \end{aligned}$$

$D_3 = D_{12} + 2D_{66} = \vartheta_2 D_{12} + 2D_k = \vartheta_1 D_2 + 2D_k$   
The equation for the deflection function W for an orthotropic material is  
the following:  $\square$

$$D_1 \frac{\partial^4 w}{\partial x^4} + 2D_3 \frac{\partial^4 w}{\partial x^2 \partial y^2} + D_2 \frac{\partial^4 w}{\partial y^4} = q(x,y) \quad (II)$$

We have theoretically obtained values of Young's modulus and Young's modulus of the second kind for the graph, and also felt stiffness. The results are shown in the table below.  $\square$

□□□□□□□□□□□□□□□□	□□□□□□□□□□□□□□	0□□□□□
□□□□□□□□□□□□□□□□	□□□□□□□□□□□□□□	0□□□□□
□□□□□□□□□□□□□□□□	□□□□□□□□□□□□□□	0□□□□□

## TEST FOR QUANTITATIVE DETERMINATION T-2 AND HT-2 TOXINS

*A. V. Koptel*

*Saratov State University*

For comparison, the shear modulus for diamond is 478 GPa, and Young's modulus of 210 GPa for steel. In 2009 we obtained values of Young's modulus for a plate of graphene – 0.737 TPa and 1,127 for the axes Ox and Oy, respectively [3]. Experimental values are the same  $1,0 \pm 0,1$  TPa [4].

B11=	0,8568
B22=	0,6749
B12=	0,0620
B66=	0,3902
D1=	2,80644E-30, TPa·m <sup>3</sup>
D2=	2,21058E-30, TPa·m <sup>3</sup>
D3=	2,24345E-30, TPa·m <sup>3</sup>

### Results

Thus, knowing the hardness and reduced coefficients of deformation  $B_{ij}$  for graphene, we can arrange the system to determine the principal and shear stresses and the equation for the deflection function  $W(x, y)$ . Therefore, knowing the coefficients of the equation for the deflection, we can solve the first or second major problem of elasticity theory for graphene, that is, either knowing the function of deflection of the graphene nanoplate we can determine the load acting on the plate, or knowing the load we can define the function of deflection graphene nanoplate.

### REFERENCES

1. *Лехтицкий С. Г. Анизотропные пластики*. М. : Государственное издательство техничко-теоретической литературы, 1957.
  2. *Лехтицкий С. Г. Анизотропные пластики*. М. : Государственное издательство техничко-теоретической литературы, 1957.
  3. *Яновский Ю. Г., Никитина Е. А., Карнеги Ю. Н., Никитин С. М. Квантово-механическое исследование механизма деформации и разрушения графена // Физическая мезомеханика*. 2009. Т. 12. № 4.
  4. *Changui Lee. Measurement of the Elastic Properties and Intrinsic Strength of Monolayer Graphene // Science*. 2008.
- After adsorption the next stadium was washing of each column with carbonate buffer (1 ml). Finally, the frit was blocked to avoid unspecific binding. It was performed with 0.5 ml 0.1% solution of casein in phosphate-saline buffer in each column for 10 minutes under intensive mixing. The next stadium was washing of column with 0.75 ml 0.2% casein in phosphate-saline buffer.

Molds can produce highly toxic substances during their growth on foods and feeds. These toxic metabolites are designated mycotoxins [1]. The mycotoxins dealt with in this paper are the T-2 and HT-2 toxins. These are one of the trichothecene mycotoxins. These are produced by members of several fungal genera, mainly by members of the genus *Fusarium*. Of over 150 known trichothecenes, only a few occur under natural conditions. T-2 toxin is one of those that have been detected in agricultural crops, especially in wheat and maize. It may be the cause of serious economic losses, and, when ingested, it can produce toxic syndromes in humans and animals in concentrations as low as micrograms or nanograms of toxin per gram of food or feed.

Estimation of trace amounts of T-2 toxin present in food sample due to fungal contamination is a difficult task, as it requires laborious and extensive cleanup treatments to remove interfering substances from the sample matrix before analysis.

Methods for determination of toxins could be classified as instrumental and non-instrumental. Most of instrumental methods are based on chromatographic principles. But an application of these methods needs dearly equipment and long difficult sample preparation. Non-instrumental methods for mycotoxin detection are mostly immunochemical, they are quick and do not require long and difficult preparation. But disadvantages of these methods are insufficient sensitivity and possible matrix influence.

So, we have developed rapid methods for determination of T-2 and HT-2 toxins in wheat samples by instrumental immunochemical test at level 0.1 mg/kg. Test is based on specific antibodies which are linked with polyethylene frit. Polyethylene frit was conditioned in ethanol during 10 minutes in an ultrasonic bath to prepare the column (Senova Abcap HP) to the adsorption of proteins. After degassing is completed (bubble formation has stopped and the filter shows an unruffled surface) the frit has to be placed into column. Then 1.5 ml of carbonate buffer was passed through each column.

Then 0.5 ml antibody in pre-selected concentration was placed into the columns and adsorption was conducted for 20 minutes at room temperature under intensive mixing.

After adsorption the next stadium was washing of each column with carbonate buffer (1 ml).

Finally, the frit was blocked to avoid unspecific binding.

It was performed with 0.5 ml 0.1% solution of casein in phosphate-saline buffer in each column for 10 minutes under intensive mixing.

The next stadium was washing of column with 0.75 ml 0.2% casein in phosphate-saline buffer.

The analysis procedure was included:

1. An incubation of the analyte. Standard toxin solution (0.5 ml) in certain concentration was placed in each column and intensive mixed under 6 minutes.
2. Washing step. Solution of casein 0.2% (0.75 ml) in phosphate-saline buffer was passed through each column to remove unbound toxin.
3. An incubation of the conjugate. The conjugate solution (50  $\mu$ l) in selected concentration was placed in each column for 3 minutes.
4. Washing step. Solution of casein 0.2% (0.75 ml) in phosphate-saline buffer was passed through each column to remove the unbound conjugate.
5. Washing step. Substrate buffer (0.75 ml) passed through each column.
6. Finally, substrate (50  $\mu$ l) was added in each column, which was the cause of color.

Determination of color intensity was performed photometrically using reader Senova: net column was a calibrate column, and then intensity of all the columns was measured. Determination was performed according to the description of the equipment.

For the immunoassay feed samples were ground and portions (5 g) were extracted with 15 mL acetonitrile–water, 80/20 (v/v), for 15 min at room temperature. Then extract was diluted 1:5. The final concentration of acetonitrile in diluted sample solution was 16% [2].

First, the optimal conditions for the single mycotoxin assay were determined. The concentrations of immunoreagents were optimized according to the following criteria: must be a maximum difference in intensity of the color between column through which is missed toxin and without toxin

The dilutions of the antibody T2 and the HT2-HRP conjugate were optimised. Antibody T2 dilutions of 1:10, 1:100, 1:1000 and 1:1500 were tested and 1:1000 was chosen as the optimal. HT2-HRP conjugate solutions were tested in the range of 1:1,000 to 1: 100,000. Satisfactory results were obtained for the dilutions in the range of 1:10,000–1:25,000. Increasing of the dilution resulted in decreasing of colour intensity and longer development time.

Matrix interference was eliminated by appropriate dilution of sample extracts with assay buffer PEG (1:1).

A general scheme for analysis of mycotoxins with immunochemical test is shown in Fig. 1. Extract of wheat was passed through the solid sorbent with grafted antibodies, if there were toxins in the sample, they were associated with primary antibody. Next, conjugate of analyte with peroxidase horseradish was added into the column, which was binded to free antibody binding sites. The final stadium was the addition of the chromogenic substrate, which was changes its color in the presence of the horse-radish peroxidase conjugate. Washing was necessary after each stadium.

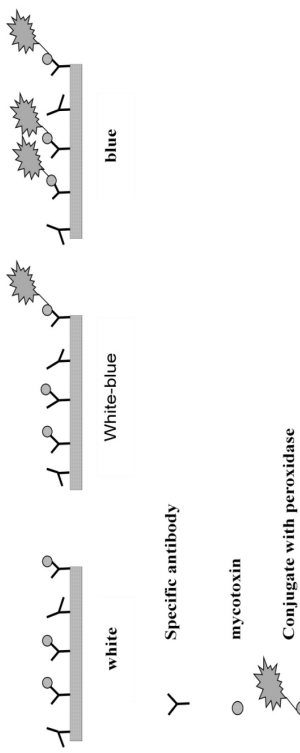


Fig. 1. General scheme for analysis of mycotoxins immunochemical test.  
A – in the presence of toxin, color did not develop by adding substrate.  
B – in the presence of small quantity of toxin, low-intensity color developed by adding substrate.  
C – in the absence of toxin, intense blue color developed by adding substrate.

Dependence of intensity of developed color from the time of its development at different concentrations of standard solutions of T-2 toxin is shown in Fig. 2. The conclusion from this dependence is that the sensitivity of determination of this method is limited quantity of 3.3 ng/ml for T-2 toxin.

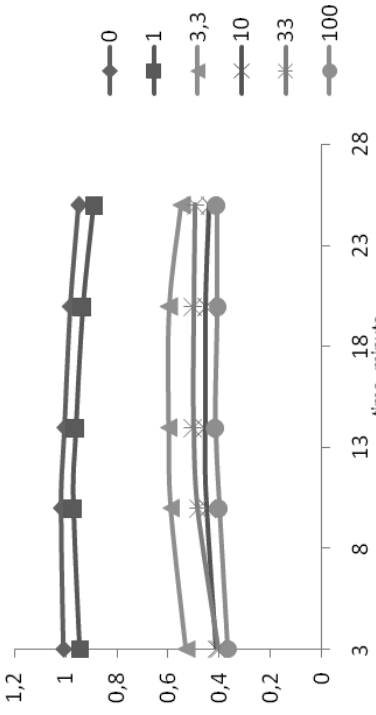


Fig. 2. Dependence of intensity of color from the time

The calibration dependence the concentration of T-2 toxin (ng/ml) of intensity (Fig. 3) is built on the basis of data from Fig. 2. This curve has a S-figurative form, which is characteristic of all competitive methods. The limit of detection is 1.1 ng/ml, which is determinated according to this curve.

Immunochemical test allows to analyze a large number of samples in a short period of time (analysis of 6 samples – 30 min) to confirm the presence or absence of T-2 and HT-2 toxins in samples for a certain concentration level. Speed of performance of analysis, high specificity of the antibodies, the precision, the ability to conduct experiments outside the lab – all of these criteria can contribute the introduction of immunochemical tests of determination T-2 and HT-2 toxins in samples of wheat in practice.

## REFERENCES

1. *De Saeger S., Van Peteghem C.* Dipstick Enzyme Immunoassay To Detect Fusarium-T-2 Toxin in Wheat. Applied and environmental microbiology. 1996, Vol.62, N6. P.1880-1884.
  2. *Basova E. Yu., Goryacheva I. Yu., Rusanova T. Yu., Burnistrova N.A., Dietrich R., Marlbauer E., Detavernier C., Van Peteghem C., De Saeger S.* An immunochemical test for rapid screening of zearalenone and T-2 toxin. Anal Bioanal. Chem. 2010, Vol. 397, N 1. P. 55-62.

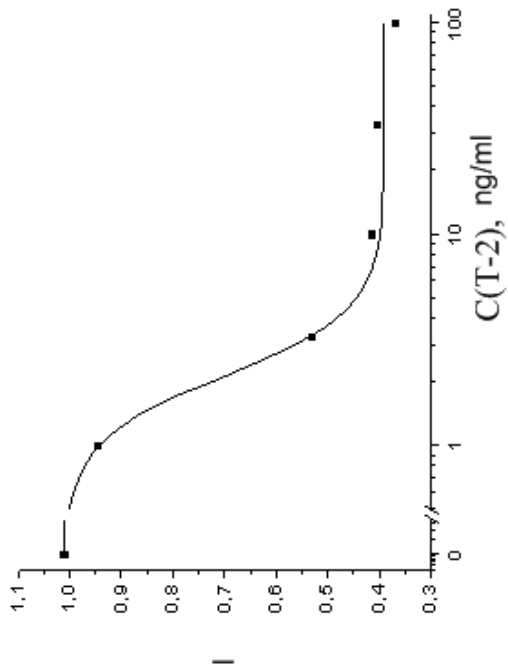


Fig.3. The calibration curve for T-2 toxin (ng / ml) determination

Dependence of intensity of color from the time of its development at different concentrations of standard solutions of T-2 toxin, extract of wheat artificially contaminated with T-2 toxin and wheat is shown in Fig. 4. Differences in values due to matrix effects of wheat.

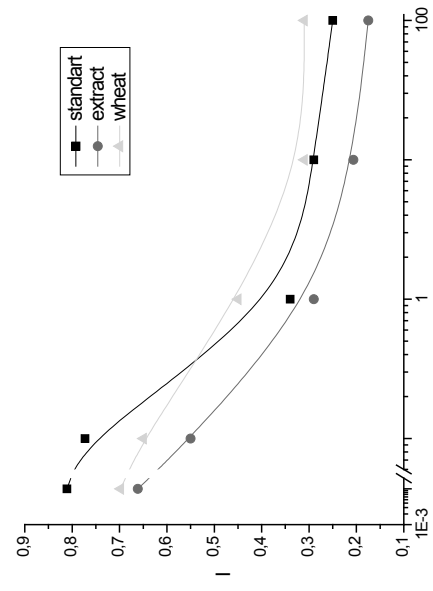


Fig.4. Dependence of intensity of color from the time of its development

At the present time, huge attention gives to questions of population health keeping and extension of life expectancy in the country. Those tasks aren't executable without qualitative medical care as well as pharmaceutical service. But under existing conditions towards the networks' managers arise the serious aim – to preserve operating efficiency and profitability of pharmacy organizations. For the effective solution of this aim it needs to process great value as statistical, as spatial information about consumers and competitors and making

Marketing is a process of goods and services advertising from producer to consumer. It is an integral part of developing and planning of each company (Kent, Omar, 2007).

There is no single marketing policy. Each company and each sales outlet should approach those questions individually for creating their own unique image. But for all that marketing activity of the most companies base on the marketing-mix concept. This concept started at the 1960<sup>th</sup> and it's the most widespread at the present moment. The point of marketing-mix concept is that marketing activity is developing systematically based on a.k.a. "4 P's":

- *product*: range of goods including amount and types of goods and brands and products of own trade mark;
- *price*: price policy including pricing for the purpose of product promotion, discounts and determine of discounts retail prices;
- *place*: stores location and ways of distribution. Factors of “place” include accessibility and location comfort and sale outlet design. As the increase of marketing influence to the work of the store need to appreciate the role of distribution centers, warehouses and storerooms.
- *promotion*: way with the help of which trade company advertises and promotes it's name through the brand image, that creates by goods' design, sign, wrapping and brand (Лахчехок, 2003).

Key point for sales outlets working in services sector, such as pharmacy companies, is a location (“place”). The location has an influence on choice of goods, prices, and ways of promotion. For the identification of the most optimal sale outlet location, marketing services have to work not only with statistical information, but also with spatial information. Spatial information analysis is impossible without visualization and processing. But it's very hard to solve this problem manually, that's why companies use different computer-aided facilities.

Geoinformation systems (GIS) often use for processing huge value of spatial information during marketing research. Geographical information systems (GIS) make it possible do following things:

- create models of pedestrian and transport accessibility;
- solve problems of carrier's route optimization (logistics tasks);
- make multifactor's analysis;
- reveal territories that are favorable of new sales outlets opening;
- estimate sales outlets prospects etc.

Thereby by cooperation marketing and geoinformation technologies will arise integrated geomarketing technologies.

Geomarketing (as a technology) is a process of planning, making decision, pricing, promotion, and realizing ideas, goods and services (includes information and political) by the use of interchange, that satisfy certain individuals and organizations thought the instrumentality of geoinformation technologies (Лверкоб, 2002).

Spatial analysis methods using for making geomarketing reports base on mapping variegated information helped to successfully solve network business problems. As a result of such analysis, can, for example, mapping data of population size, structure, sales of own network, business rivals location, creating models of prospective customer movement etc (Лверкоб, 2002).

For successful pharmacy network development it is necessary to allow lots of parameters: goods' and services' prices, service level, advertising actions etc. But, in the F. Kotler and S. Wolton opinions, there are “3 keys to store's success: place, place and one more time place” (Корнеп, 1991). Geomarketing technologies allow to process huge volume of spatial information in

- computer-aided mode for exist market position analysis. They allow reducing level of uncertainty during the process of making decision about new sales outlets opening and existing store network developing.
- factors, influence to the situation. Using GIS technologies increase amount of the factors to the needed for analysis propose.

Concerning pharmacy networks, it is possible to sort out the following main factors, influencing for sales outlet success:

- quantity of people, living on the territory;
- quantity of people, working on the territory;
- remoteness from the business rivals;
- nearness to the main transport and pedestrian roads;
- nearness to the center of population gravity.

Those factors are identify sales outlet profitability, range of goods, pricing policy etc.

Thereby, the most optimal pharmacy location is: in dense population part of the city, where at the same time working lots of people, located near big transport and pedestrian road of the city, near shopping centre or bus stop and faraway from business rivals. This case is perfect and now days there are not such places within the city, that's why it is necessary to find the places with the most optimal combination of all 5 factors.

For availability analysis, authors suggested numerical score of the territory:

$$A = \frac{K}{H + T + (P / 2)} \times O,$$

where A – index of the territory availability, H – density of population numerical score, T – density of working on this territory population numerical score, P – population stream numerical score, K – decreasing coefficient of competitive influence, O – coefficient of neatness to the bus stops influence (Хвопотухин, 2010).

We will see below the concept of those indexes (tables 1, 2).

**Table 1**  
**Numerical score of working and living population density**

Population density, people/hectare	Density of working on this territory population, people/hectare	Points
less than 50	less than 25	1
from 50 to 100	from 25 to 50	2
from 100 to 150	from 50 to 100	3
from 150 to 200	from 100 to 200	4
more than 200	more than 200	5

Table 2

Coefficient K value	Koefficient K
Time of pedestrian availability to nearest pharmacy, min	
less than 5	2
from 5 to 10	1,3
from 10 to 15	1,2
from 15 to 20	1,1
more than 20	1

For people's streams analysis, all streets were divided into 5 classes that were given appropriate points:

1. Streets and passages with a little population size (low-rise built-over land);
2. Main streets of low-rise built-over land and small streets of the central part of the city
3. Main streets;
4. Main trunk roads and central streets;
5. Streets located in the places of the most people concourse and are the main transport and pedestrian roads.

Then, by the special possibilities of GIS all this indexes will sum up and for the each part of the territory will define the index of the territory availability (A). Whole territory of Saratov was divided into 3 classes:

1. The least perspective (from 1 to 5 points);
2. Perspective (from 5 to 9 points);
3. The most perspective (more than 9 points).

According this dividing, the map of perspective zones for opening new pharmacies was created (fig. 1).

As we can see from the map, the most perspective zones are areas near Podstantsia, Gorodskoy park, Oktyabrskoe ravine, Kosmonavtov embankment, housing estate near 3<sup>rd</sup> Dachnaya and Sokolovogorskij settlement. Perspective zones are also areas the most remote from the exist pharmacies, territories near bus stops and considerable area of the Saratov central part in spite of many exist pharmacies. It is because of the facts, that this is an area of the main people streams (here locates lots of working places, entertaining centers, stores, shopping centers).

Results of analysis show the general picture of the perspective places for new pharmacies location. For pharmacies proper places identification are needed to organized detailed research of the situation for each perspective area. GIS technologies simplify and accelerate the process of treatment spatial information and allow reducing charge of marketing projects.

## PERSPECTIVE ZONES FOR OPENING NEW PHARMACYS



Figure 1. Perspective zones for opening new pharmacies

Also the most important factor that influence to availability index (nearness to the bus stops) was taken into account. If the territory locates in the range of one hundred-meters-long zone from the bus stop (i.e. within the field of vision), the coefficient O will be 1.5 points. Otherwise it will be 1 point.

#### REFERENCES

1. Даниченок Л.А. *Основы маркетинга*. М.: ММКИФИ, 2003.
2. Котлер, Ф. *Основы маркетинга*. М.: Прогресс, 1991.
3. Хеорострухин Д.Л. Геоинформационное моделирование в маркетинговых исследованиях (на примере анализа аптечной сети г. Саратова) // Научные исследования студентов Саратовского государственного университета: Материалы IV конференции В.Я. Геомаркетинг: практические задачи и методы. М.: Финансы и статистика, 2002.
4. Цветков В.Я. Геомаркетинг: практические задачи и методы. М.: Финансы и статистика, 2002.
5. Kent T., Omar O. Retailing. New York, 2007.

#### PHOTODYNAMIC LIPOLYSIS WITH INDOCYANINE GREEN

**Kozina A. M., Yanina I. U., Svenskaya U. I., Genina E. A., Portnov S. A., Bashkatov A. N., Tuchin V. V.**

Saratov State University

#### Introduction

The problem of the overweight is worldwide. Hypodermic fat depot not only bring about psychologic problems but present a real risk for human health. Today the most popular method of destruction fat depots is lipoplasty. Besides the traditional suction-assisted lipoplasty, other options include ultrasound-assisted and external ultrasound-assisted liposuction, power-assisted liposuction, and laser lipolysis.

The efforts in the search for alternatives and new tools aim mainly at reducing downtime, decreasing operator effort for the surgeon and assistant, reducing bleeding and promoting skin tightening. It is necessary to develop novel optical technologies of photodynamic and photothermal therapy. [1]

The goal of our work is development of photodynamic method using capsular Indocyanine Green. Indocyanine green (ICG), a tricarbocyanine dye with a strong absorption band between 600 and 900 nm, has been used in medicine since 1956 and exhibits some characteristics of an ideal photosensitizer, in particular absorption in the near infrared part of the visible spectrum (805 nm in human plasma) allowing deeper tissue penetration. [2]

#### Materials and methods

In our experiment we used capsular ICG. This dye is well-attached with albumin and is distributed in blood very fast. So, we expect that if we have capsular ICG we can apply it more locally. [3] In the places where we have fat cells.

Shells are spheres with radius 4-5 μm. The encystations process is presented here

(Fig. 1): A) it is ageing polyelectrolytic multi-layer shells in compound solution, which is needed to be encyst and molecules of which can percolate through shell membrane. b); f) compound had been warming up until shells diameter started decrease and shells covering became impenetrable; it leads to three – fourth of capsular substance closing; c), g) extraction of ambient molecules by frequentative ablation in water; d),e) salt adjunction leads to sponginess of micro-shells walls and it conduce to macro-molecules penetration through shells covering.

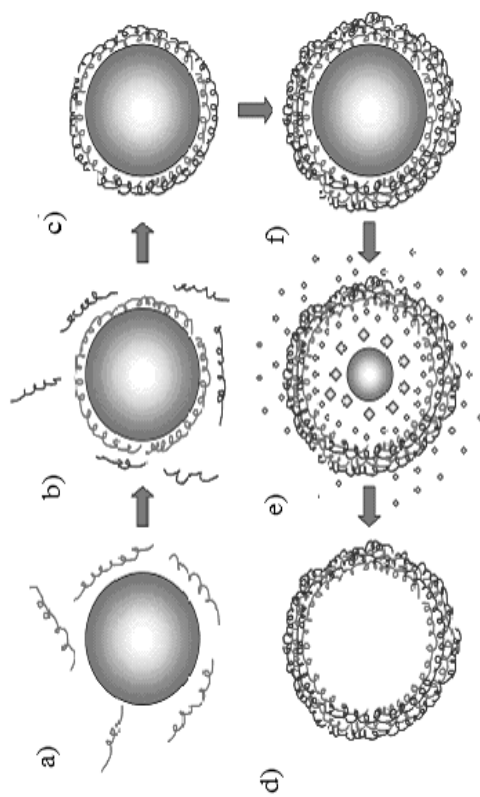


Fig. 1. The encystations process

Pilot plant and experimental methodology  
The device of tube (Fig. 2) comprises microscope, Digital Camera for Microscope DCM500 (USB2.0) Resolution 5 M pixels, which was conglomerated with personal computer.

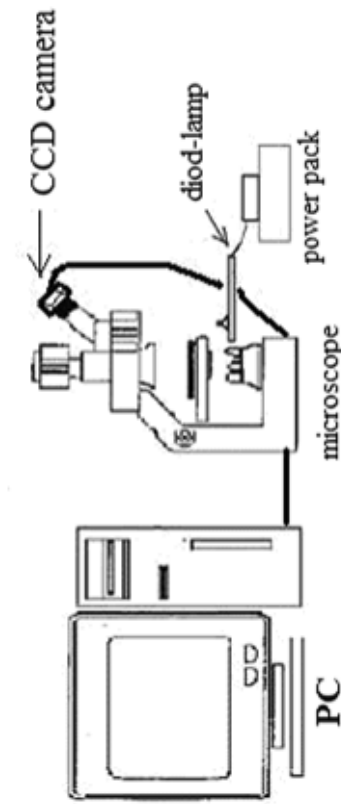


Fig. 2. The device of tube.

1. we took human fat tissue (post-surgical material). After refrigeration we made thin tissue truncation (thickness about 100 mcm). And then the sample was set up on micrometer stage.

2. some drops of solution with dye encystes were applied topically.

3. then the tissue was being irradiated during 1 minut, irradiation power – 1,5 W (OPC-B015-MMF-FCITS, 805 nm; Ultra Lume Led 5)

4. and then the sample was being observed during 2 – 3 hours, with certain temperature maintenance

5. the photos of the cells taken by camera were transferred to the personal computer.

Photos were taken every 5 minutes.

- Photo of fat tissue immediately after irradiation;
- Photo in 45 minutes after irradiation;
- Photo in 2 hours after irradiation;
- Photo in 2 hours 45 minutes after irradiation;

We could already see membranes destruction under laser light influence in 15 min by detail observing. And if we look at the photo, which was taken in 2 hours 40 min we could see almost absolute fat cells localization. And we could see remnant on tissue ICG shells.

We suppose that light irradiation (dyed) fat tissue leads to the damage of fat cells by means of apoptosis mechanism. Low intensity irradiation of dying cells leads to the damage of their membranes and ICG outgate in intercellular area. So it is possible to actualize lipolysis process.

#### Conclusion

As we know, ICG connects with cells membranes protein. [5] Capsular ICG, can not make such adumation [4], but we see that membrane damage took place, so, we expect, that under the influence of light ICG effluents from shells and interacts with membrane proteins.

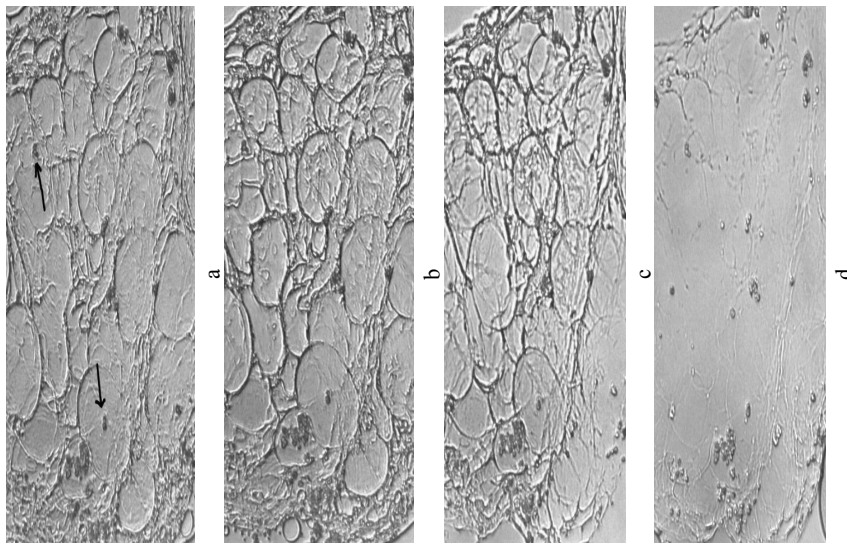


Fig. 3. Fat tissue condition before and after dyeing and irradiation.

We made spectrophotometric measurements collimated and total transmittance and diffusion reflectance of ICG shells in water. Measurements have been made before and after irradiation and after 4 hours. Here are diagrams, which present correlation between this coefficients and wavelength. Changes in collimate transmittance diagram looked especially intelligible, but we could also observe changes in diffusion reflectance and total transmittance. It confirms our conjectures that ICG effluent from shells after laser exposure.

It is just a conjecture, brought forward empirically, which demands detailed study and confirmation. The researches can be useful for developing novel optical technologies for treatment of obesity cellulite, as, evidently, the optical technologies promise less danger to the patient than the widely used surgical and pharmaceutical treatments.

## REFERENCES

1. Serge R. Mordon, Benjamin Wassmer, Jean Pascal Reynaud, Jaouad Zemmouri. Mathematical modeling of laser lipolysis. *Biomedical engineering online*, 2, 2008.
2. Green F.J. The Sigma-Aldrich Handbook of Stains, Dyes and Indicators. Aldrich Chemical Company, Inc. Milwaukee, Wisconsin, 407, 1990.
3. E. Donath, G.B. Sukhorukov, F. Caruso, et al. Novel Hollow Polymer Shells by Colloid-Templated Assembly of Polyelectrolytes. *Angew. Chem. Int. Ed.*, 16 (37), 2201-2205, 1998.
4. G. B. Sukhorukov, D. B. Volkakin, A.M. Gruenert, et. al. Porous calcium carbonate microspheres as templates for encapsulation of bioactive compounds. *Journal of Materials Chemistry*, 14, 2073 – 2081, 2004.
5. Янина И.О., Симонченко Г.Р., Кочубей В.И., Тучин В.В. Спектры поглощения жировой ткани человека при ее сенсибилизации красителями. Оптика и спектроскопия, 109 (2), 247-255, 2010.

## 3) Decomposition by time steps.

Every system part on every detail level can be decomposed using one of the presented principles. The choice depends of structure and purpose. Thereby all principles can be used over and over again and combine with each other.

The decomposition by roles

If every component of the divided system describes some role or some piece of the system, the decomposition by roles can be applied. As a rule such components functioning is parallel and stand-alone, except interacting at special moments of time.  
The example the decomposition principle using is conveyor systems. It is very useful to divide a conveyor into blocks. Every block do its own work, in other words it has personal role in the system. A blocks interacting is passing products from block to block. Every conveyor block is implemented by separated case-effect complex, the complexes links implements interacting. The decomposition by stages

If there are some separated time stages can be identified in the system, decomposition by stages can be applied. Very often the stages run consistently – stage by stage, the next stage depends of the previous stage results.  
Pay attention, that unlike the decomposition by roles, when the system components describe parallel processes for all system functioning time, using the decomposition by stages, every stage describes only part of the time, then it transfers control to the next stage.

The example of using the principle is a procedure of one product creating: preparing, conversion, painting, assembling, testing, and shipping.  
The decomposition by time steps

Despite the fact that the decomposition by time steps is the special case of decomposition by stages, it allows to synchronize parallel processes in complicated system, which makes the principle applying rather efficient in a complicated systems modeling.

There are two conditions under which using the decomposition by time steps principle is justified. The first, a model developer does not know quantity and lengths of the stages. The second, the stages cores have equal cores.

The decomposition by time steps principle allows dynamically dividing the system functioning process into different length parts (steps). The interaction between system components occurs at step changing. The every step length is chose individually before modeling and depends of the system structure, purposes and interaction specifics. The main purpose of decomposition in this case is the parallel processes synchronizing.

The principle realization requires adding some auxiliary complexes in decomposition structure; also it requires some special functionality of the modeling complexes.

The structure of a complex, decomposed by time steps

Without losing generality, let's consider a cause-effect complex, which describes a system. The system will consist of three parallel processes, which will interact with each other (Fig. 1).

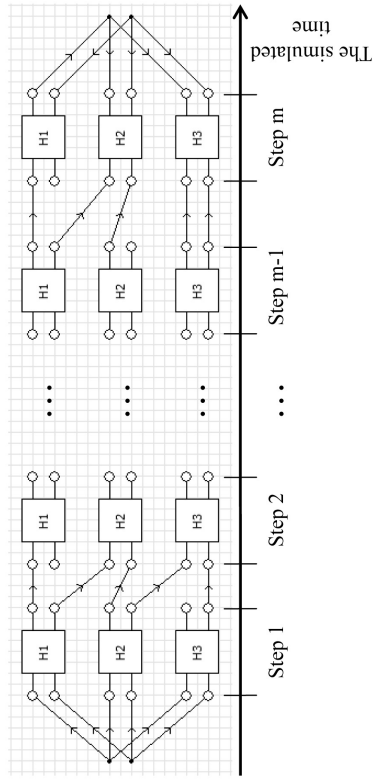


Fig. 1. Three chains of complexes, which describe parallel processes

The complex is divided into  $m$  steps, every step contains three modeling complexes (notice, the three modeling complexes represent the decomposition by roles). The interactions between processes are implemented by appropriate links between complexes.

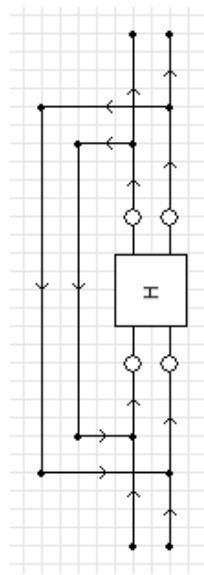


Fig. 2. The cycle construction

Unfortunately, the steps quantity and the length of every step are unknown at designing time, because this information will be defined using causes and conditions at modeling time. Therefore the author suggests using cycle constructions (Lapkovsky R., 2010) for the most common complex structure developing, which allows system modeling with different start causes and conditions. Every step is described by one cycle iteration (Fig. 2). Complex «H» includes three complexes, which describe three parallel processes. The parallel processes synchronization Despite the fact that the problem of the steps variable quantity and lengths has been solved, the problem of processes synchronization stills open.

Let's consider the problem in details. The interaction between couple of processes is realized by the cause-effect link between two complexes: the first complex, which describes the first process on the step number  $i$  and the second complex, which describes the second process on the step number  $i+1$ . For bigger interactions number cause-effect link is applied for everyone. Every modeling complex at every step has to describe own process for some simulated time, for ending at the moment, when interaction is needed.

The main complication is that all complexes must get the information of a step length before they will model the step. In other words all interacting complexes must have the information of the nearest interaction time. Initiative and receive complexes can be allocated. Only initiative ones have the information of coming interaction, at the same time receiving ones have not any information about it. Therefore they can't model own processes for needed time.

For solving the problem author suggests using the special states method (Бусленко Н.Н., 1968). In the cause-effect complexes modeling the special state is a system state at which interaction between any processes is required.

Every modeling step divided into two substeps. At the first substep every modeling complex calculates the time, the appropriate process will pass to the special state. Then the special auxiliary complex calculates a minimal time value. At the second substep every modeling complex models the system for the calculated minimal time.

Thereby the system modeling process is divided into time steps; every of them finishes with special state, when the interaction is realized. Such dividing is rather optimal, because the fewer number of steps dividing erases some interactions, the greater number of steps dividing increases cycle iterations, which will makes extra load.

The article suggests the approach for parallel processes synchronization as one of the decomposition principles in the cause-effect complex designing. The additional information about processes synchronization approach presented in (Иванов А.С., Лапковский Р.Ю., Уколов Д.А., Филимонюк Ю.О., 2011).

### Conclusion

In the way of the cause-effect complexes system approach the classification of the complicated complexes decomposition principles have been represented. Also author suggests some advantages and disadvantages of every principle applying. The cause-effect complex designing using decomposition by time steps have been represented in details. The principle allows describing complicated systems, which consist of a big variety of parallel processes interacting.

## REFERENCES

1. Буслаенко Н. П. Моделирование сложных систем. М.: Наука, 1968. С. 198 – 228.
2. Иванов А. С., Лапковский Р.Ю., Укоб Д.А., Филиппонок Л.Ю. Кибернетический подход к моделированию разнородных процессов в мехатронных системах. // Мехатроника, автоматизация, управление. 2011. № 1. С. 16 – 20.
3. Резников А. Ф., Твердохлебов В. А. Причинно-следственные комплексы взаимодействий производственных процессов. // Проблемы управления. 2010. № 3. С. 51 – 59.
4. Резников А. Ф., Твердохлебов В. А. Причинно-следственные комплексы взаимодействий производственных процессов. // Проблемы управления. 2008. 137 с.
5. Lapkovsky R. The modification of the model of a cause-effect complex // Представляем научные достижения мира. Естественные науки: Материалы научной конференции молодых ученых «Presenting Academic Achievements to the World», 29–30 марта 2010 г. – Саратов: Изд-во Сарат. ун-та, 2010. – 164 с.: ил.

mechanically damaged. Then the water, bypassing liquid state, sublimes in high vacuum ( $1.3 \cdot 10^{-4} - 1.3 \cdot 10^{-5}$  Pa). Dehydrated sample is placed in the pouring environment. This method eliminates the effects of chemical fixatives and dehydrating agents. But application of freeze – drying method is connected with variety of difficulties. Although it is possible to avoid the formation of water crystals during the rapid and deep freeze theoretically, it is difficult to achieve practically [1].

Method of freeze – replacement decreases tissue damage caused by soaking tissue in the pouring environment. Also this method saves membranes containing lipids. The first step of freezing is the same as in the method of freeze – drying, but water in glassy state is removed by immersing the frozen tissue before pouring into acetone, alcohol or any other dehydrating substances. However, artefacts appear in the structure of samples because of application of chemical agents.

Method of freeze – etching virtually eliminates both chemical and structural changes in tissues that are caused by chemical fixation, dehydration, pouring and cutting. The tissue is immersed with glycerol and frozen in liquid freon which is cooled to  $-150$  °C by liquid nitrogen. Then the tissue is immersed in liquid nitrogen ( $-196$  °C). After extraction of liquid nitrogen tissue is placed on the cooled table and broken down with the blade. Fracture surface is exposed to high vacuum. Interface is etched and organelles are segregated in relief. Then the etched surface is sprayed by a coating of platinum and carbon. The disadvantage of this method is requirement of special equipment and skills [2].

Spraying of a uniform conductive coating allows us to investigate the dielectric biological samples. Method of covering the objects surface with conductive layer of carbon or metal (gold, platinum etc.) is often used [3].

### 3. Methods of research of biological specimens

Biological specimens can be investigated by different methods of electron microscopy. At first, samples should be prepared and covered with conductive layer. Then they can be investigated in high vacuum mode and in this case high resolution is achieved.

Low vacuum mode allows investigating non-conducting materials in their natural state. This mode can also be used in case when specimens gas during evacuation. You can also study damp samples in low vacuum mode, using the method of freezing. However, due to residual gas in the chamber, electrons are strongly dispersed, preventing us from obtaining high-resolution images. Also, low vacuum mode does not provide full compensation charge in the bulk, but only on the surface of the sample. To exclude the formation of space charge region it is preferable to use low-voltage mode, where low-energy electron beams do not penetrate deep under the surface [4].

## SCANNING ELECTRON MICROSCOPY RESEARCH OF BIOLOGICAL SPECIMENS

A. Osokina

Saratov State University

### 1. Introduction

Biological specimens are insulators, which often contain liquid and change their structure under the influence of electron beam. For these reasons, their study is associated with certain difficulties, such as special sample preparation and selection of the regime of investigation which shouldn't change the structure of the sample. Therefore there is a necessity for study methods of preparing biological specimens and technique of their investigation by scanning electron microscopy (SEM).

### 2. Methods of preparing biological specimens for research by SEM

Sample preparation can be divided into the following steps: processing of the sample until it is fixed, fixation, drying and sputtering of conducting coating. Methods of freeze – drying, freeze – replacement or freeze – etching are often used to avoid artefacts.

Method of freeze – drying decreases probability of appearance of artefacts and retains low-molecular proteins in the specimen under consideration. The essence of this method is that a small piece of tissue is placed in isopentane, freon or any other liquid, cooled with liquid nitrogen. In this case, the tissue is stabilized, and all metabolic processes immediately stop. Water, bypassing crystalline phase, transforms into the glassy state. Therefore, the cells are not

#### 4. Local rise in surface temperature

There are two types of electron dispersion: elastic and inelastic. In case of elastic dispersion the direction of velocity vector is changed, and its absolute value remains practically constant, so kinetic energy of electrons is not changed. Energy that transferred from the electron beam to the sample is less than 1 eV. And this energy is negligible compared with its initial energy, which is usually 10 keV or more. In case of inelastic dispersion energy transferred to atoms and electrons of the sample and the kinetic energy of the electron beam decreases. And some quantity of the energy is transferred into solid state due to excitation of lattice vibrations, i.e. due to heating. In the case when the electron beam falls on a massive sample, an area in which it gives the energy is in good thermal contact with the whole mass of the sample, acting in this case as an effective heat sink. In this way a significant rise in temperature of the sample in the beam incidence is prevented. In thin samples or at high currents and accelerating voltages of the electron beam a significant heating of the bombarded area can take place. [5].

For an axisymmetric electron beam falling normal to the surface of a semi-infinite body with thermal characteristic  $\lambda$ , the task of heating is as follows:

$$\frac{1}{a} \frac{\partial T(r, z, t)}{\partial t} - \Delta T(r, z, t) = \frac{q(r, z, t)}{\lambda}. \quad (1)$$

Solving this problem they suggest that heat losses from the surface are absent, i.e.:

$$D = \frac{C_2 V_2 J}{(C_1 - C_2) S \tau} \quad (2)$$

The initial temperature is assumed to be zero,  $q(r; z, t) -$  volume source [6]. Local rise in temperature along the radius on the surface of the beam axis for isotropic substrates can be estimated with the help of the following equation:

$$\delta T(r) = \frac{U I}{4 \pi k d} \left( 2 \frac{I}{r} \left( 1 - e^{-r/I} \right) - e^{-r/I} \right), \quad (3)$$

where  $U$  – voltage applied to the electrodes;  $I$  – the tunneling current,  $k$  – coefficient of thermal conductivity of the substrate;  $d$  – the length of the inelastic dispersion of electrons in the substrate;  $r$  – radius of the beam on the sample surface [7].

This formula is valid for continuous heating of the sample area. Since the SEM electron beam moves over the sample at a certain rate, then each section of the sample has a local rise in temperature that is proportional to the inverse velocity of beam pattern, which is equal to the inverse sweep rate of output. For equation (3) two utmost cases are considered:

1.  $r >> l$ ;

2.  $r < l$ , suggesting that  $r = l/2$ .  
In the first case the equation is:

$$\delta T_1(r) = \frac{U I}{2 \pi k r}; \quad (4)$$

In the second case, the expansion of the exponential in Taylor series leads to:

$$\delta T_2(r) = \frac{U I}{8 \pi k r} * 1.5. \quad (6)$$

The dependence of local heating of the sample on the beam radius for voltages 30 kV and 3 kV and for peak current was obtained. The data presented in Fig. 1.

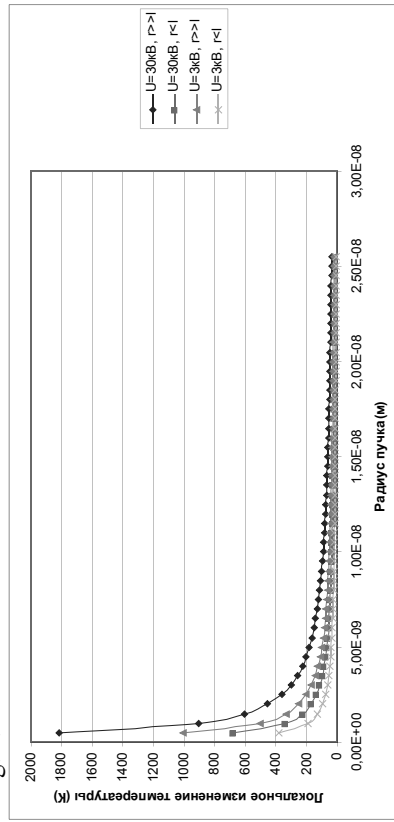


Fig.1. Dependence of the local temperature change of the beam at accelerating voltage of 30 kV and 3 kV, peak current and inverse sweep rate 437.4 ms / pxl.

From these results it is clear that increasing the inverse sweep rate local rise in temperature at the given point increases. Also, the surface heating increases significantly with increasing of accelerating voltage and current. The electron beam is better focused on the sample, the smaller radius of the interaction of electrons with the sample. But as the exponential schedule shows, the heating of the surface increases with decreasing radius of the beam.

Thus, increasing the voltage and current electron beam, the radius of the beam and the inverse sweep rate, on the one hand, we can get better quality image, but on the other hand, there is a greater local heating of the sample.

## 5. Experimental analysis of samples

Different samples were investigated for the mastering of methods for studying biological samples by SEM: human tooth cut, bone structure with implants, polymer fibers based on chitosan coated with mammalian epithelial cells (Fig. 2).

Structure images of dentin were obtained when studying the surface morphology of human tooth cut (Fig. 2a). In this paper we used samples of human tooth cut as an object of investigation. The cut of the tooth was obtained by sawing the sample with high-speed circular saw with a diamond disk. Then the objects of research were washed in phosphoric acid and treated in an ultrasonic bath to remove impurities of organic and inorganic nature. Gold thickness of 5 nm was sprayed for better conductivity. Morphology of the dentin (the layer under the enamel) was studied using scanning electron microscope Mira \ LMU

The interaction of bone structure with implants coated with silver-containing substance was considered (Fig. 2b). It was concluded that when applying an antibacterial silver-containing coating and with increasing time of engraftment, is the best healing of the bone with the implant.

It was studied the morphology of polymer fiber structures based on chitosan and their interaction with the epithelial cells of a mammal. All samples were dried without external influence, i.e. using natural evaporation of liquid, and studied in high vacuum mode. In this case, epithelial cells strongly deformed (Fig. 2c). Gold thickness of 5 nm was sprayed to obtain high-quality of images. It was found that using the method for drying biological samples leads to significant deformation of their shape and size changes. It was found that the cells are fixed in fabric material in the cells between the fibers of the material with subsequent ingrowth (Fig. 2d).

## 6. Conclusion

In this paper ways of preparing biological samples for research by scanning electron microscopy were investigated. Basic methods of research of biological samples were studied and mastered: low and high – vacuum modes. Thermal effect of electron beam on the sample was studied. In particular dependence of the local temperature increase from the beam radius was obtained.

Different samples were investigated for mastering the methods for studying biological samples by SEM: human tooth cut, bone structure with implants, polymer fibers based on chitosan coated with epithelial cells of a mammal.

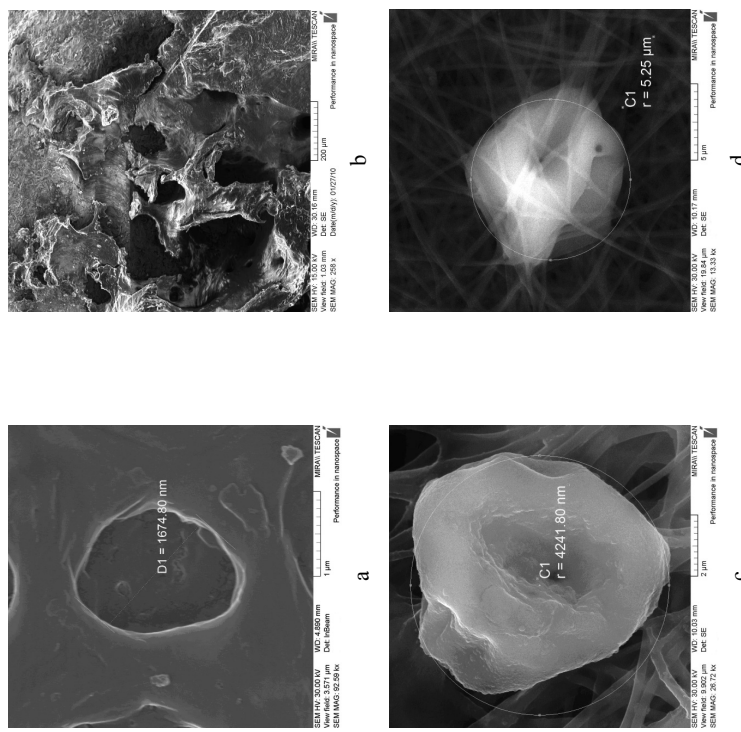


Fig. 2. The results of studies of biological samples by SEM:  
a) The image of morphology of human tooth cut with an increase in  $93 kx$ . b) The image of seam of bone and implant, coated with silver material. Term engraftment is 40 days. c) The morphology of the cell with an increase in  $27 kx$ . d) The morphology of fibers coated with cells after 24 hours.

## REFERENCES

1. Karpupu V.Ya. Electron Microscopy. – K.: Karpupu B.Y. Электронная микроскопия. – K.: Highest School. Head Publishing, 1984 – 208 p.
2. Willy B. Electron Microscopy for Beginners. – M.: World, 1985 – 314 p.
3. Kerrick D.M., Emihizer L.B. and Villame J.F. The role of carbon film thickness in electron microprobe analysis // Amer Mineral. 1973 – No 58 – 920-925 p.
4. Ivanov S. Low-voltage Scanning Electron Microscopy for the Study of Nanomaterials // Nanotech, 2009, 1-5 p.
5. Goldstein J. Newberry D. In 2 vol.: Scanning Electron Microscopy and X-ray Microanalysis, vol.1: Trans. from English. – M.: World, 1984 – 303 p.
6. Rikalin N.N. Zhev I.V. Fundamentals of electron beam processing of materials. – M.: Engineering, 1978 – 238 p.
7. Nevolin V.K. Probe of nanotechnology in electronics. – M.: Technosphere, 2005 – 152 p.

Quinolone effectiveness antibiotics are the most important clinical medication with wide spectrum of biological action and high effectiveness. Many analytical methods such as high performance liquid chromatography (Roudaut B., 2002), thin layer chromatography (Choma I., 2004), spectrophotometry (Mostafa Samia, 2002), and fluorimetry (Hebphoeba H.B., 2007) have been described for their determination in biological liquids, foodstuff and drugs. However, for screening the drugs in respect of their falsification or fast semi quantitative determination chemical test methods should be developed.

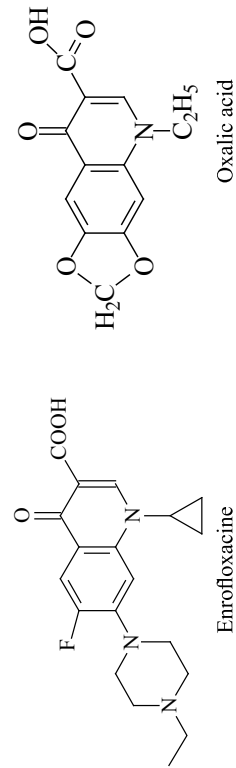
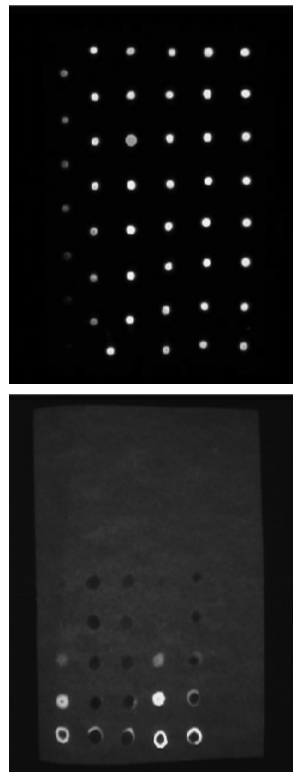


Figure I. Structural formula of antibiotics.

The aim of our present study was to investigate a possibility to determine the enrofloxacin and oxalic acid (Fig. 1) antibiotics using their fluorescence signal on TLC plate. To enhance the native fluorescence signal of adsorbed antibiotics we test the effect of surfactant micelles, lanthanide ions, some second ligands and their combination. In this way, the enhancement of fluorescence intensity was recorded using video densitometer "Sorbfil" ( $\lambda_{\text{exc}} = 365 \text{ nm}$ ) and "Sorbfil" ATX TLC plates with normal silica stationary phase. Micelles of sodium dodecylsulfate (SDS, anionic surfactant), cetylpyridinium chloride (CPC, cationic surfactant), triton X-100 and brij-35, both nonionic surfactants, were selected as representatives of surfactants.  $\text{Tb}^{3+}$  as lanthanide ion, EDTA and 1,10-phenanthroline (Phen) as second ligands.

As matrix were used filter paper and TLC plates “Sorbfil ATLC”. After the treatment of reagents and antibiotics on the filter paper the unequal sorbution due to high porousness of sorbent was occurred. Visually it was observed in forming diffuse and incompact zones that impeded the processing of image in Photoshop CS3. Among the tested materials the clearest images of the stains of antibiotics were obtained when using the Sorbfil ATLC plates. The spaces for all analyzed spots were equal (Fig. II).



**Figure II.** The application of filter paper (a) and TIC plates (b) as matrix

It was established that antibiotics investigated have insignificant native fluorescent signal. Addition of all surfactants mentioned did not change the intensity of Enrofloxacin and Oxalic acid fluorescence. An impregnation of silica by  $Tb^{3+}$  salt changed a color of fluorescence due to formation of chelate with energy transfer and enhanced slightly the intensity of enrofloxacin and oxalic acid emission. Complexation of quinolones with metals to produce fluorescent chelates has been used for the development of fluorimetric method for the determination of these compounds. The excitation of the complexed lanthanide ion must also be achieved via the organic ligand which would thus act as an antenna or sensitizer, thereby compensating for the low absorption coefficient of the lanthanide ion. Hence, the sensitized lanthanide-based emission in complexes with the proper organic chromophoric units displayed important enhancements, several orders of magnitude larger. In these cases the excitation of the ligand is followed by intramolecular energy transfer from the ligand triplet state to the lower-lying emissive lanthanide excited state

The sensitisation fluorescence is occurred in cases when the triplet state energy of ligand is equal or exceeds the resonance level of metal ion. The triplet state energies for enrofloxacin and oxalic acid are 24280 cm<sup>-1</sup> and 20620 cm<sup>-1</sup>, respectively, both much higher in energy than the resonance level of Eu<sup>3+</sup> (17260 cm<sup>-1</sup>) and Tb<sup>3+</sup> (20500 cm<sup>-1</sup>) ions (Смирнова Т.Д., 2009). The large energy gap between the resonance levels of the acceptor and excitation states of donor molecule determine the efficient of energy transfer. Hence for binary chelate with Eu<sup>3+</sup> ion the less intensity of fluorescence (emission) excited state.

simultaneous treatment of TLC plates by  $Tb^{3+}$  and micelles of SDS or CPC slightly enhanced of Oxalic acid while mixture of  $Tb^{3+}$  and triton X-100 or bri-35 enhanced Oxalic fluorescence by a factor 1.6 and 2.3, simultaneously wavelength 545 nm) then for chelates with  $Tb^{3+}$  where the energy gap corresponds to effective energy transfer. Modification of  $Tb^{3+}$  – enrofloxacin complex by EDTA and Phen second ligands was also ineffective.

ously. Maximum fluorescence of Enrofloxacin reached in the case of modification by  $Tb^{3+}$  and brij-35 micelles. The use of micellar systems to enhance the fluorescence of metal ion complexes is well known. Micelles provide an environment characterized by higher viscosity and lower polarity than the bulk aqueous solution and hence increased luminescence quantum yields can be expected (Sanz-Medel, 1987).

Relationship between the intensity of luminescence of the Tb (III) complexes with enrofloxacin and oxalic acid and the pH of the solution were investigated in a range from 3 to 11. Maximum intensity of luminescence of sorbents of the complexes enrofloxacin and oxalic acid with Tb (III) as in aqueous solutions is detected at pH 6.8–7.6.

In this methodic the application of buffer was refused due to high dilution of reagents in spots that significantly decreased the intensity of  $Tb^{3+}$  binary chelates fluorescence.

The investigation of influence of sorbents humidity on intensity of a signal showed that 30 minutes heating of TLC plates by the temperature (30–36°C before treatment is essential. This procedure decrease the quenching of  $Tb^{3+}$  fluorescence by aqua molecules, sorbed on TLC plate.

It was established that the treatment of TLC with larger quantities of sample solution on the stains enhance the intensity of fluorescence. The optimal volume of the sample applied to the plate and provided maximum intensity of signal constitutes 2  $\mu$ l for each antibiotics.

The determination of enrofloxacin and oxalic acid  $1 \cdot 10^{-1}$  M was conducted by graduation graphs. Different amounts of the standard solutions of oxalic acid and enrofloxacin in a range of concentrations  $1 \cdot 0 \cdot 10^{-3}$  M –  $1 \cdot 0 \cdot 10^{-2}$  M were applied to the plate. As the reagent was used the mixture of  $Tb^{3+}$  ( $1 \cdot 0 \cdot 10^{-2}$  M) and Brij-35 ( $1 \cdot 0 \cdot 10^{-1}$  M) solutions in proportion 1:1. The intensity of fluorescence was measured at 548 nm.

The graduation graph was constructed in coordinate system the intensity of main color (G) – the concentration of antibiotics. As a result test-methods for determination of enrofloxacin and oxalic acid in the interval  $10^{-3}$  M –  $10^{-2}$  M and in the presence of  $Tb^{3+}$  – Brij-35 system were developed.

## REFERENCES

- Nefrologa N.B., Смирнова Т.Д., Штыков С.Н. Флуориметрическое определение некоторых хинолонов с помощью золатов гербия в организованных средах // Современные проблемы теоретической и экспериментальной химии: Межвуз. Сборник науч. Трудов VI Всерос. Конф. Молодых ученых с Международным участием. Саратов: Изд-во «Научная книга», 2007. С. 213-217.*
- Смирнова Т.Д., Штыков С.Н. и др. Флуориметрическое определение локсициклина с помощью золата европия и 1,10-фenantролина в мицеллярных растворах Тритона X-100 // Химия и химическая технология. 2009. Т.52, вып. 1. С. 39 – 42.*
- Choma I., Choma A., Komanecka I., Pilorz K., Staszczuk K. Semiquantitative estimation of enrofloxacin and ciprofloxacin by thin-layer chromatography-direct bi-*

- aoutography // J. Liq. Chromatogr. and Relat. Technol. 2004. Vol. 27, № 13, P. 2071 – 2085.
- Mostafa Samia, El-Sadek Mohamed, Awad Alla Esmail. Spectrophotometric determination of ciprofloxacin, enrofloxacin and pefloxacin through charge transfer complex formation // J. Pharm. and Biomed. Anal. 2002. Vol 27, № 1 – 2, P. 133 – 142.*
  - Rouadaut B., Yorke L-C. High-performance liquid chromatographic method with fluorescence detection for the screening and quantification of oxolinic acid, flumequine and sarafloxacin in fish // J Chromatogr. B. 2002. 780, N 2, c. 481-485.*
  - A. Sanz-Medel, R. Fernandez de la Campa, J.I. Garcia Alonso. Metal chelate fluorescence enhancement in micellar media: mechanism of action // Analyst. 1987. Vol. 112, P.493.*

## THE MAIN PHYSICAL AND CHEMICAL PROPERTIES OF NANOFILTRATION MEMBRANES BASED ON ALKYLPIRIDINIUM SALTS

### E. S. Pogorelova, E. G. Kulapina, N. M. Makarova

Saratov State University

Synthetic surfactants are widely used in everyday life (disinfectants and detergents) and industry (corrosion inhibitors, additives in the textile industry), which leads to environmental pollution. Biologically hard cationic surfactants – alkylpyridinium salts – are very dangerous for ecology. Therefore summary and separate determination of cationic surfactants becomes an actual. Membrane technologies are the most inexpensive and universal methods of separation. The investigation of transport processes in nanofiltration membranes gives the information about the basic physical and chemical characteristics of membranes: diffusion, permeability, ion fluxes (Кулапина Е.Г., Чернова Р.К. и др. 2008).

Diffusion, permeability and ion fluxes were determined in practice. For this purpose we constructed the two-chamber cell (fig.1). It consists on source and receiver sections and molecular sieve (nanofiltration membrane) between them. The pore sizes correspond to sizes of the molecule of cetylpyridinium chloride,  $C_{16}P_1 = 1\%$ . Mixing solutions in the sections of the source and the receiver is realized by means of magnetic stirrers. Chamber's volume is 1.59 ·  $10^{-3}$  m<sup>3</sup>.

The methodology of the researches on the basic parameters of membrane transport is as follows. The nanofiltration membrane was previously prepared for the work: it was keeping in 500 ml of distilled water during 7 days. The source was filled by solution of alkylpyridinium salt  $C_nH_{2n+1}C_5H_5NCl$  ( $n=10$  – decyl-,  $n=16$  – cetyl-,  $n=18$  – oktadecylpyridinium) with the known concentration ( $1 \cdot 10^{-3}$  –  $1 \cdot 10^{-4}$  M), the receiver was filled by distilled water. Further

sampling was carried out the chambers through 30, 90, 120, 150, 210 minutes from the start of the experiment ( $V_{\text{aliquot}} = 1 - 10 \text{ ml}$ ). Determination of the concentration of test substances at the source and the receiver was performed by potentiometric titration using solid-contact sensor based on cetylpyridinium tetraphenylborate.

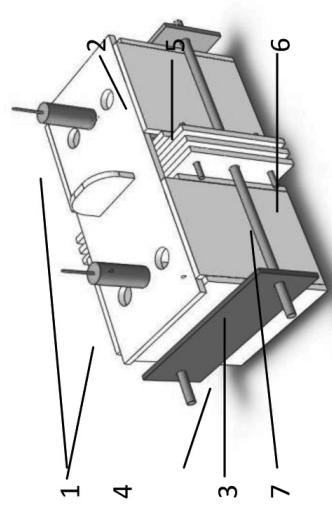


Fig. 1. There is the two-chamber cell for the investigation of transport characteristics of membranes. 1 – ion selective electrodes, 2 – plexiglass container, 3 – source,  $V=330 \text{ ml}$ , 4 – cap, 5 – receiver,  $V=330 \text{ ml}$ , 6 – molecular sieve, 7 – fastening plates.

Mass transfer through the membrane passes the following steps: diffusion through the boundary layer, adsorption of substances on the surface of the membrane, transport through the membrane, desorption from the membrane, diffusion through the boundary layer on the reverse side of the membrane (Ярославцев А.Б., Никоненко В.В. и др., 2003). These transport processes can characterize quantitatively by diffusion coefficient, permeability and ion flux.

The diffusion coefficient is the amount of material passing through  $1 \text{ m}^2$  of membrane surface at a constant temperature per unit time and a difference of concentrations on both sides of the membrane equal to one (Плещинский М.Б., Абрамzon A.A., 1999). In our case we have only the pore diffusion characterized by sorption processes inside the membrane. The diffusion coefficient is calculated by the formula (Ковалев С.Б., Лазарев К.С., 2008):

$$D = \frac{C_2 V_2 l}{(C_1 - C_2) S \tau},$$

where  $C_1$  – the concentration of solute in the source,  $M_1$ ;  $C_2$  – the concentration of solute in the receiver,  $M_2$ ;  $V_2$  – the volume of the receiver,  $\text{m}^3$ ;  $l$  – the membrane thickness,  $\text{m}$ ;  $S$  – working area of the membrane,  $\text{m}^2$ ;  $\tau$  – the time of experiment, sec.

The permeability is a phenomenological concept and it encompasses a variety of mechanisms of mass transfer across the membrane (ХАБАРСИЧ Т.С., КАММЕРШТЕЙН К., 1981). The permeability depends on the diffusion coefficient, the concentration of diffusing substance and the thickness of the membrane:

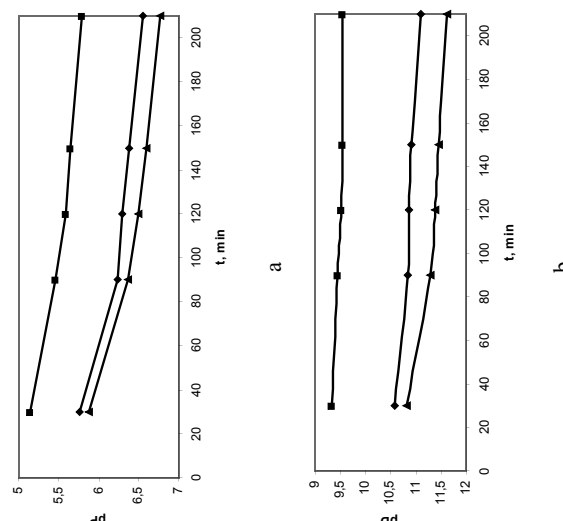
$$P = D \frac{C_1}{C_2 l}.$$

Membrane permeability with respect to various substances, and consequently, the flow of these substances are different and depend on the membrane properties. For a quantitative description of diffusive mass transfer through a nanofiltration membrane we can use the following equation for the ion flux (Харитонов С.Б., 2003):

$$J = P(C_1 - C_2).$$

Next, we consider the dependence of described parameters of membrane transport on the time of experiment and the concentration of diffusing substances.

Permeability, diffusion and ion flux of cationic surfactants are decreased during the experiment. This is due to blockage of the membrane pores by surfactants, which have good adsorption capacity because of its oil and water sensitive (fig.2).



The resulting pattern is the fact that sieve pores become clogged quickly with increasing concentrations of diffusing substances, and transfer rate of ions decreases, thus we observe decreasing of permeability of nanofiltration membrane. The total number of the substance passing through the sieve increases, therefore ion flux increases. The driving force of diffusion is a concentration gradient, under which the solute diffuses through the membrane in the direction of a dilute solution, so that the diffusion coefficient decreases with increasing concentration of cationic surfactant in the source.

Thus, in the present work the transport properties of nanofiltration membranes based on alkyliridium salts in the conditions of diffusive mass transfer were investigated; the basic parameters of membrane transport: diffusion coefficient, permeability and ion flux were calculated; their dependences on time and concentration of diffusing substances were established.

#### REFERENCES

- 1 *Козаев С.В., Лазарев К.С.* Исследование кинетических коэффициентов полимерных мембран на двухкамерной плоскокамерной ячейке // Труды ПГТУ. 2008. Вып. 21. с. 22-23.
- 2 *Кулапина Е.Т., Чернова Р.К., Кулапин А.И.* Потенциометрические сенсоры для определения синтетических поверхностно-активных веществ. Саратов. «Научная книга», 2008 г. 205 с.
- 3 *Петельский М.Б., Абрамzon А.А.* Особенности диффузии поверхностно-активных веществ через пористую мембрану // Журн. физ. химии. 1999. Т.73. №6. С.1085-1088.
- 4 *Харитонов С.В.* Транспортные свойства селективных мембранны, обратимых к катионам азотсодержащих органических оснований: проницаемость и поток ионов // Журн.аналит.химии. 2003. Т. 58. №2. С.199-206.
- 5 *Хванг С.-Т., Каушерштейн К.* Мембранные процессы разделения. / Пер. с англ. М.: «Химия». 1981. 464 с.
- 6 *Ярославцев А.Б., Никоненко В.В., Заболоцкий В.И.* Ионный перенос в мембранных и ионообменных материалах // Успехи химии. 2003. Т.72. № 5. С. 438.

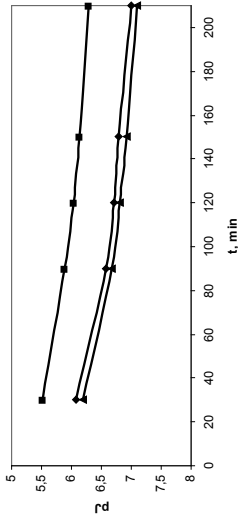


Fig. 2. The dependences of diffusion (a), permeability (b), ion flux (c) of DP (1), CP (2) and ODP (3) from time of experiment ( $C_{\text{initial}}=5 \cdot 10^{-4} \text{ M}$ , pore former is CP, 1%).

When the concentration of cationic surfactants in the source increases, ion flux increases, but permeability and diffusion decrease (fig.3).

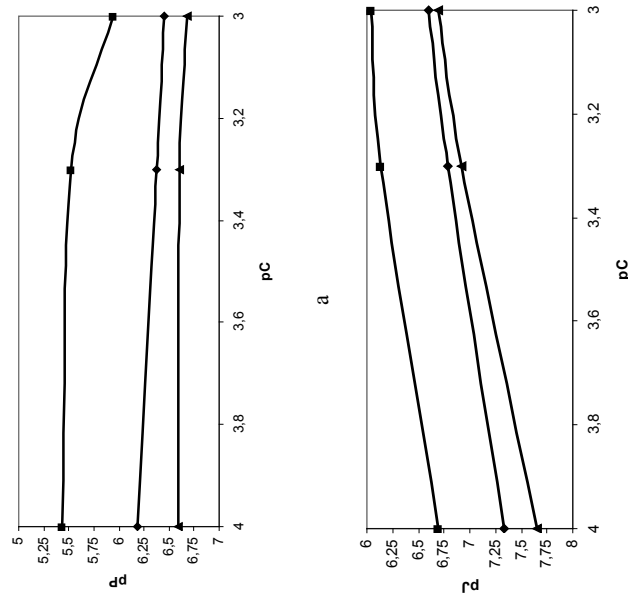
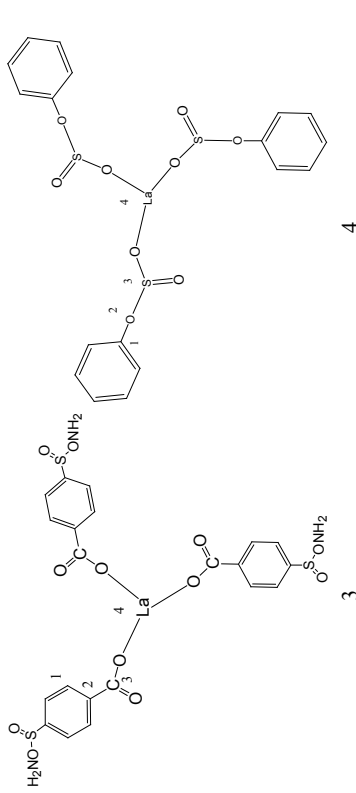


Fig. 3. The dependences of diffusion (a), permeability (b) and ion flux (c) of DP (1), CP (2) and ODP (3) from initial concentration of solution of cationic surfactants (pore former is CP, 1%).

Saratov State University

M. V. Pozharov

1. Introduction  
For many years the scientists of the Chair of General and Inorganic Chemistry of Saratov State University have researched interactions between



salts of rare earth metals (REMs) and organic acids. Such compounds include REM benzoates, salicylates, 4-sulfoamidobenzoates, benzosulphonates and other complexes with metal/ligand ratio of 1:3 ( $\text{LnAn}_3$ ). However, while there are many publications dedicated to synthesis of such complexes and study of their physical and chemical properties (Диденко Е.А., 1974; Пиркес С.Б. и др., 1972; Пиркес С.Б., Диденко Е.А., 1976; Пиркес С.Б. и др., 1984; Ермоленко В.И., 1962; Xia Li, Chun-Yan Wang and Huai-Ming Hu, 2008; Xia Li, Yan-Qiu Li and Xiao-Shuo Wu, 2008) some questions regarding molecular structure of the said complexes require contemporary quantum chemical study. It should be noted that until recent times (Васина А.А., Захарова Т.Б., 2006; Монахова Ю.Б. и др., 2008) complex REM compounds with organic ligands have never been studied using the quantum chemical methods.

The primary objectives of this work are to study molecular structure of lanthanum complexes with organic ligands with the help of contemporary quantum chemical methods and to find a connection between structural characteristics and physical and chemical properties of lanthanum complexes with organic ligands.

## 2. Methods of study

Figure 1 shows graphic formulas of studied compounds with important atoms numbered. Electron structure and geometry of the studied complexes were computed using PC GAMESS v. 7.0 (GAMESS (US)) program with ab initio UHF-SBKJC basis which can be used to optimize structure of molecules containing the rare earth metal atom and to study properties of the said molecules. Experimental data (thermal stability and solubility in water) of the studied complexes have been taken from works conducted by scientists of the Chair of General and Inorganic Chemistry (Диденко Е.А., 1974; Пиркес С.Б. и др., 1972; Пиркес С.Б. и др., 1984).

## 3. Results and discussion

The results of structural study of lanthanum benzoate (Fig.1, □ 1), lanthanum salicylate (Fig.1, □ 2) and lanthanum 4-sulfoamidobenzene (Fig.1, □ 3) are present in Table 1. The common structural feature of these complexes is that lanthanum is coordinated with organic acid ligands by oxygen atom of carboxyl group in the said ligands. According to the data presented in Table 1, the interaction between lanthanum cation and organic acid anions leads to substantial polarization of  $\text{C}\square\text{O}$  bond which is manifested in the increase of electron density on oxygen atom. At the same time, the increase of negative charge of carboxyl group carbon atom is observed for all studied complexes which, along with the decrease of  $\text{C}\square\text{O}$  bond order and increase of the said bond length, indicates the positive mesomeric effect of carboxyl group.

Unlike the other complexes, in the course of interaction between lanthanum cation and sulfonylbenzoate-anion (Fig.1, □ o. 4) the atom of lanthanum becomes coordinated with the ligand by oxygen atom of sulfonate group. Changes in geometry and electron structure of resulting compounds are similar to those of complexes 1-3 (Table 1). At the same time, an increase of positive charge of sulfur atom (from 0.99 to 1.18) is observed. The presence of oxygen atom with lone-electron pair near the atom of sulfur leads to an increase of electron density on oxygen atom from -0.75 to -0.81. The formation of donor-acceptor bond between lanthanum cation and oxygen of sulfonate group leads to decrease of  $\text{S}\square\text{O}$  bond order from 1.08 to 0.86, subsequently increasing length of the said bond.

According to calculation data, the existence of a rather strong bond between lanthanum cation and organic acid anion is evidenced by the decrease of charge on lanthanum atom (from 3.0 in its individual state to 2.1-2.3 in complexes 1-4) and the corresponding values of  $\text{La}\square$  bond order. The length

of La-O bond in the said complexes are  $\approx 2.53$ - $2.54$  Å, which corresponds to known values of covalent bond length for lanthanum atom.

Spatial structure of the aforementioned lanthanum complexes has also been studied. The results of spatial structure study are present in Table 1. The study has shown that complexes 1-3 (benzoate, salicylate and 4-sulfoamidobenzoate) have non-planar structure, the torsion angle between atoms 1, 2, 3 and 4 (see Fig. 1) in these complexes is 78.9° and carboxylic groups lie in the same plane as benzene rings. The torsion angle between atoms 1, 2, 3 and 4 in lanthanum benzosulfonate was found to be much less (only 12°) than the same angle in complexes 1-3 where lanthanum coordinates with organic acid ligand through carboxylic group.

On the basis of calculated values of full energy of organic acid anions, lanthanum cation and corresponding complexes, we can deduce the amount of energy contained in one La-O bond of the studied complexes (Table 1). According to calculation data, interaction between lanthanum cation and oxygen atom of organic acid anion leads to stabilization of C-O and S-O bonds in corresponding ligands which are less energetically stable in individual organic acid molecules. The bond energies are rather high and have the same order of magnitude for all studied compounds.

magnitude for all studied compounds.

After the geometry was settled, the positions of bands in IR-spectra as well as zero-point energies of benzoate-anion and lanthanum benzoate were found (Table 2). It should be noted that calculated spectra of benzoate-anion and the corresponding lanthanum complex are free of imaginary frequencies which means that we have reached global minimum during the optimization of the said compounds geometry. As you may see from Table 2, experimental and calculated positions of band in IR-spectra of lanthanum benzoate correlate rather well, this being another proof of calculation validity. In the course of interaction between lanthanum cation and benzoic acid the stretching frequency of carboxylic group shifts from 1690 cm<sup>-1</sup> in ligand to 1664 cm<sup>-1</sup> in complex 1. It should also be noted that the band corresponding to symmetrical stretching vibrations of COO-group shifts from a higher-frequency zone in benzoate-anion to a lower-frequency zone in lanthanum benzoate ( $\Delta=29$  cm<sup>-1</sup>).

Table I

Principal structural characteristics of organic acid anions and lanthanum complexes with corresponding anions

*Table 2*  
Primary bands of benzoate-anion and lanthanum benzoate IR spectra (experimental and calculated data),  $\nu$ ,  $\text{cm}^{-1}$ .

No.	Band assignment	Lanthanum benzoate (exp.)	Lanthanum benzoate (calc.)	Benzoate-anion (calc.)
1.	$\nu(\text{C-H, aromatics}), \text{cm}^{-1}$	3080	3091	3070
2.	$\nu(\text{C=O}), \text{cm}^{-1}$	1674	1664	1690
3.	$\nu(\text{C=C, aromatics}), \text{cm}^{-1}$	1606, 1591	1594, 1597	1560, 1617
4.	$\nu_{\text{as}}(\text{COO}), \text{cm}^{-1}$	1542	1543	-

*End table 2*

No.	Band assignment	Lanthanum benzoate (exp.)	Lanthanum benzoate anion (calc.)	Benzooate-anion (calc.)
5.	$\nu_s(\text{COO})$ , $\text{cm}^{-1}$	1400	1387	1416
6.	$\delta(\text{C-H, aromatics})$ , $\text{cm}^{-1}$	1184, 1107, 1016, 856	1172, 1107, 1006, 866	1215, 1106, 1071, 850
7.	Zero-point energy, $\text{kJ/mol}$		879	286

Thus, IR-spectra confirms coordination of lanthanum atom with organic acids molecules by the oxygen of hydroxyl-group.

Another primary objective of this work was to find a connection between computed structural parameters and physical and chemical properties of lanthanum complexes found through various experimental methods. Analysis of various structural and experimental parameters of studied lanthanum complexes has resulted in finding several correlations between a structural characteristic (bond order, dipole moment) and a physical property (decomposition temperature, solubility) of the complex in study.

When comparing experimental data with calculated structural characteristics, it was found that decomposition temperature goes higher as La-O bond energy increases, thus increasing thermal stability of the compound. The solubility of complexes in polar solvent (water) increases as electrical dipole moment increases which is not surprising as it follows a well-known pattern: substances of similar nature usually are highly soluble in each other.

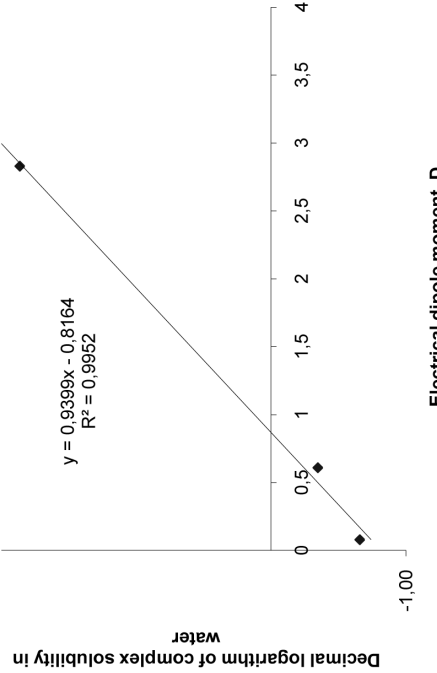


Fig. 2b: Correlation between electrical dipole moment of complex molecules and decimal logarithm of complex solubility in water (at 25°C)

The correlation between average decomposition temperature and calculated La-O bond energy can be shown as a linear plot (Fig. 2a). The same can be said about correlation between logarithm of complex solubility and electrical dipole moment of the said complex (Fig. 2b). The plot data was processed using least-square procedure, the correlation coefficients being 0.99.

#### 4. Conclusion

On the basis of linear dependencies between the aforementioned structural characteristics and physical properties it can be concluded that calculated structural parameters can be used to find physical and chemical characteristics of lanthanum complexes with similar geometry and electron structure. Decomposition temperature goes higher as La-O bond energy increases, thus increasing thermal stability of the compound. The solubility of complexes in polar solvent (water) increases as electrical dipole moment increases which is not surprising as it follows a well-known pattern: substances of similar nature usually are highly soluble in each other. The study has shown that calculated characteristics can be used to correctly assess physical and chemical properties of molecules (such as its solubility in water and decomposition temperature) a priori. This assessment can be used to synthesize compounds with desired properties for a particular application such as separation of rare-earth metals from a complex mixture.

Thus, it can also be said that quantum chemical calculation data correlates with experimental data rather well. Calculation also confirms coordination of

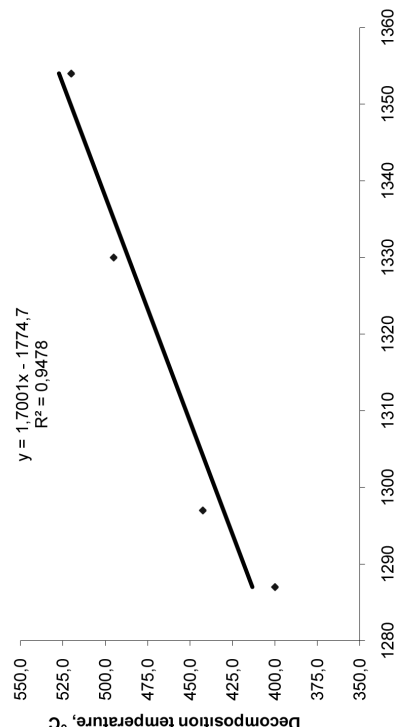


Fig. 2a: Correlation between La-O bond order and complex decomposition temperature

lanthanum complex with organic acid anions through the atom of oxygen. Linear dependencies between structural parameters (bond order, electrical dipole moment) and physical properties (complex decomposition temperature, solubility of the said complex in water) can be used to synthesize compounds with desired characteristics.

#### Acknowledgements

The author thanks Mushtakova S.P., Zacharova T.V. and Monakhova Yu. B. for providing helpful advice and reference materials and making helpful discussions of the details of this work.

#### REFERENCES

- Лиценко Е.А. Синтез и физико-химическое исследование соединений редкоземельных элементов с бензосульфоновой и о-сульфобензойной кислотами : дис. ... канд. хим. наук. Саратов, 1974. 150 с.
- Пиркес С.Б., Лиценко Е.А., Буцкова Р.Т., Шестакова М.Т. Получение и изучение некоторых свойств о-сульфобензоатов РЭ персиковой подгруппы // Ж. неорган. химии. 1972. Т.17. №11. С.2922-2925.
- Пиркес С.Б., Лиценко Е.А. ИК-спектры средних о-сульфобензоатов РЭ // Коопр. химия. 1976. Т.2. №5. С.691-694.
- Пиркес С.Б., Пашкай А.В., Ваистуб Т.Г., Баранова Т.А., Чулкаевич А.К., Файнлейб А.М. П-сульфамидбензоаты лантанидов и иттрия // Ж. неорган. химии. 1984. Т. 29. №10. С.2488-2491.
- Еришоненко В.И. Комплексные соединения салициловой кислоты с редкоземельными элементами. // Редкоземельные элементы. – Киев: Изд-во АН УССР, 1962. – С.148-162.
- Баранова Т.А. Синтез и физико-химическое исследование РЭ с ароматическими кислотами, содержащими амино- и сульфогруппы: дис. ... канд. хим. наук. Саратов, 1989. 200с.
- А.А. Васина, Захарова Т.В. Квантово-химическое изучение строения молекул ароматических кислот и соединений РЭ // Химические науки, выпуск 3 / Саратов: Научная книга, 2006. С. 36 – 39
- Ю.Б. Монахова, С.П. Мулатакова, Т.В. Захарова, М.В. Поликаров Взаимодействие лантана с некоторыми органическими кислотами. Квантово-химический расчет // Изв. Сарат. ун-та. Новая сер. Сер. Химия. Биология. Экология. вып. 2/2. С. 17-21.
- Xia Li, Chun-Yan Wang and Huai-Ming Hu. The first example of tetrานuclear lanthanide complexes with 2-sulfobenzoate and 1,10-phenanthroline// Inorganic Chemistry Communications. 2008. Vol. 11, №3. P. 345-348
- Xia Li , Yan-Qiu Li and Xiao-Shuo Wu 1-D and 2-D lanthanide coordination polymers constructed from 4-sulfobenzoate and 1,10-phenanthroline// Inorganic Chemistry Communications. 2008, Volume 11, Issue 7, 774-778

We consider some optimality solutions of antagonistic games with preference relations. In such games, instead of payoff functions, reflexive binary preference relations are given. A game with preference relations *in the normal form* is a system

$$G = \langle X, Y, A, \rho, F \rangle$$

where  $X$  is the set of *strategies* of player 1,  $Y$  is the set of *strategies* of player 2,  $A$  is the set of *outcomes*,  $r \subseteq A^2$  is a preference relation of the player 1,  $F$  is the realization function, that is, a map from the set of all *situations*  $X \times Y$  into the set of outcomes  $A$ . Assertion  $a_1 \leq a_2$  means that outcome  $a_1$  is less preference than  $a_2$  for player 1.

**Remark.** For antagonistic game a preference relation of the player 2 is  $\rho^{-1}$ .

Given a preference relation  $r \subseteq A^2$ , we denote  $\rho^s = \rho \cap \rho^{-1}$  its symmetric part and  $\rho^* = \rho \setminus \rho^s$  its strict part. We write  $a_1 \overset{\rho}{\leq} a_2$  instead of  $(a_1, a_2) \in \rho$ ,  $a_1 \overset{\rho}{\sim} a_2$  instead of  $(a_1, a_2) \in \rho^*$ ,  $a_1 \overset{\rho}{<} a_2$  instead of  $(a_1, a_2) \in \rho^*$ .

We introduce three types of equilibrium concepts: equilibrium (Rozen, 2010), Pr-equilibrium and saddle point. We consider antagonistic games with various preference structure: linear, acyclic, transitive and antisymmetric (Savina, 2010).

**Definition 1.** Situation  $(x_0, y_0) \in X \times Y$  is called

- an *equilibrium point* if for any strategies  $x \in X, y \in Y$  the condition holds:

$$F(x, y_0) \overset{\rho}{\geq} F(x_0, y_0) \quad (2)$$

- a *Pr-equilibrium point* if for any strategies  $x \in X, y \in Y$  the condition

$$F(x, y_0) \overset{\rho}{\geq} F(x_0, y_0) \quad (3)$$

- is satisfied;

- a *saddle point* (or *Nash equilibrium*) if the condition

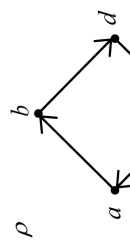
$$F(x, y_0) \overset{\rho}{\leq} F(x_0, y_0) \overset{\rho}{\leq} F(x_0, y) \quad (4)$$

holds.

**Example.** Consider antagonistic game  $G$  of the form (1) in which the set of strategies of player 1 is  $X = \{x_1, x_2\}$ , the set of strategies of player 2 is  $Y = \{y_1, y_2\}$ , the set of outcomes is  $A = \{a, b, c, d\}$ , the realization function is given by the Table 1 and the preference relation is given by diagram (Fig. 1).

Table I  
The realization function  $F$

$F$	$y_1$	$y_2$
$x_1$	$a$	$b$
$x_2$	$c$	$d$



Situations  $(x_1, y_1)$  and  $(x_2, y_2)$  are saddle points but outcomes in theirs are different.  
From this example it is easy to show that the following assertion is true.

**Proposition.** In antagonistic games with acyclic preference structure of the form (1) the outcomes in saddle points are the same.

**Definition 2.** In antagonistic game  $G$  of the form (1) outcome  $a$  is called • acceptable for player 1 if

$$\neg(\exists x \in X)(\forall y \in Y)F(x, y) >^{\rho} a;$$

- quite acceptable for player 1 if  $(\exists y \in Y)(\forall x \in X)F(x, y) >^{\rho} a$ ;

- acceptable for player 2 if  $\neg(\exists y \in Y)(\forall x \in X)F(x, y) <^{\rho} a$ ;
- quite acceptable for player 2 if  $(\exists x \in X)(\forall y \in Y)F(x, y) \leq^{\rho} a$ .

**Definition 3.** Outcome  $a$  is said to be *acceptable (quite acceptable) in game  $G$*  if it is acceptable (quite acceptable) for both players.

**Definition 4.** Situation  $(x_0, y_0) \in X \times Y$  is said to be *acceptable (quite acceptable) in game  $G$*  if outcome  $F(x_0, y_0)$  is acceptable (quite acceptable) in game  $G$ .

The basic properties of equilibrium concepts are the following result.

### Theorem

1. In antagonistic game with preference relations of the form (1) the following conditions hold:

- a)saddle points are equilibrium points;
- b)Pr-equilibrium points are equilibrium points also.

2.Saddle points are Pr-equilibrium points in antagonistic game with transitive preference structure.

3.In antagonistic game with linear transitive preference structure three types of equilibrium concur.

4.Any quite acceptable outcome is acceptable in antagonistic game with preference relations of the form (1).

5.Outcome in equilibrium point is quite acceptable (and acceptable also) in antagonistic game with preference relations of the form (1).

6.Let  $G$  be an antagonistic game with linear and antisymmetric preference structure. If set of quite acceptable outcomes is nonempty, then set of saddle points is nonempty also.

Proof.

1. a) Let  $(x_0, y_0)$  be a saddle point. Suppose that situation  $(x_0, y_0)$  is not an equilibrium point. Then there exist  $x' \in X, y' \in Y$  such that the condition  $F(x', y_0) >^{\rho} F(x_0, y_0)$  or  $F(x_0, y_0) >^{\rho} F(x_0, y')$  holds. Let the first condition is satisfied. Putting in condition (4)  $x = x'$  we get  $F(x', y_0) \leq^{\rho} F(x_0, y_0)$  which is contradictory with the condition  $F(x', y_0) >^{\rho} F(x_0, y_0)$ . Thus,  $(x_0, y_0)$  is an equilibrium point.

b) Let  $(x_0, y_0)$  be a Pr-equilibrium point. Putting in condition (3)  $x = x_0$  we get  $F(x_0, y_0) >^{\rho} F(x_0, y)$ . Now putting in condition (3)  $y = y_0$  we obtain  $F(x, y_0) >^{\rho} F(x_0, y_0)$ . Hence,  $F(x, y_0) >^{\rho} F(x_0, y)$ . Thus,  $(x_0, y_0)$  is an equilibrium point.

2.Let  $G$  be an antagonistic game with transitive preference structure. Let  $(x_0, y_0)$  be a saddle point in game  $G$ . Suppose that situation  $(x_0, y_0)$  is not a Pr-equilibrium point. Then there exist  $x' \in X, y' \in Y$  such that the condition  $F(x', y_0) >^{\rho} F(x_0, y')$  holds. Putting in (4)  $x = x', y = y'$  we get  $F(x', y_0) \leq^{\rho} F(x_0, y')$ . Since

relation  $\rho$  is transitive then  $F(x', y_0) \leq F(x_0, y')$  which is contradictory with the condition  $F(x', y_0) \stackrel{\rho}{>} F(x_0, y')$ . Thus,  $(x_0, y_0)$  is a Pr-equilibrium point.

3. Let  $G$  be an antagonistic game with linear transitive preference structure. It is sufficient to proof that equilibrium points are saddle ones. Let  $(x_0, y_0)$  be an equilibrium point. Since relation  $\rho$  is linear then condition (2) will be written in the form  $F(x, y_0) \stackrel{\rho}{\leq} F(x_0, y_0) \stackrel{\rho}{\leq} F(x_0, y)$ . Thus,  $(x_0, y_0)$  is a saddle point.

4. The assertion follows from logical rule of changing quantifiers  $\exists V \Rightarrow \forall \exists$ .

5. Let  $(x_0, y_0)$  be an equilibrium point. For  $x = x_0$  we get outcome  $F(x_0, y_0)$  is quite acceptable for player 2 and for  $y = y_0$  we obtain outcome  $F(x_0, y_0)$  is quite acceptable for player 1. Thus,  $F(x_0, y_0)$  is a quite acceptable in game  $G$ .

6. Let  $G$  be an antagonistic game with linear and antisymmetric preference structure. Let  $a$  be a quite acceptable outcome then the system of the conditions

$$\begin{cases} (\exists x_0 \in X) (\forall y \in Y) F(x_0, y) \stackrel{\rho}{\not\leq} a, \\ (\exists y_0 \in Y) (\forall x \in X) F(x, y_0) \stackrel{\rho}{\not\geq} a. \end{cases}$$

is satisfied. Since relation  $\rho$  is linear then we get

$$F(x, y_0) \stackrel{\rho}{\leq} a \stackrel{\rho}{\leq} F(x_0, y). \quad (5)$$

Putting in the last condition  $x = x_0, y = y_0$  we obtain  $F(x_0, y_0) \stackrel{\rho}{\leq} a \stackrel{\rho}{\leq} F(x_0, y_0)$ .

Since relation  $\rho$  is antisymmetric then  $F(x_0, y_0) = a$ . Put in condition (5)  $a = F(x_0, y_0)$ . Thus,  $(x_0, y_0)$  is a saddle point.

## REFERENCES

1. Rozen V.V. Equilibrium Points in Games with Ordered Outcomes // Contributions to game theory and management. Vol. III. Collected papers on the Third International Conference Game Theory and Management. SPb.: Graduate School of Management SPbU, 2010. P. 368 – 386.
2. Savina T.F. Homomorphisms and Congruence Relations for Games with Preference Relations // Contributions to game theory and management. Vol. III. Collected papers on the Third International Conference Game Theory and Management. SPb.: Graduate School of Management SPbU, 2010. P. 387 – 398.

The nonlinear waveguides and periodical nonlinear structures exhibit attractive properties that make them suitable for novel devices development with wavelength tunable characteristics. Bragg grating systems are widely used in optical communication systems, as notch filters (Yaremcuk et al., 2008), in dispersion compensation modules (Sumetsky, Eggleton, 2005), in pulse compressors, in optical multiplexers and demultiplexers (Romero et al., 2003), with an optical circulator, as fiber Bragg grating biosensors (Yu, Yin, 2008), in nonlinear optical cells and tissues microscopy, in the all-optical switching devices (Stegeman, Wright, 1990; Broderick et al., 2000).

The waveguiding properties and the possibility of soliton propagation in nonlinear periodic dielectric structures are interesting subjects of intensive investigation during past several decades. The soliton formation is based on the interplay between temporal dispersion and nonlinearity in the system (Agrawal, 2007). The typical length at which this balance is achieved varies from a few hundred meters to several kilometers. In real Bragg grating structures this balance is realized only in a few centimeters (Taverner et al., 1998). Being opposed to conventional solitons, which can be formed due to dispersion of glass material, the solitons in Bragg grating exist because of the balance between the nonlinearity and the dispersion of the grating. These gap solitons propagate stably through the grating and due to modulation instability in grating structure the periodic train of pulses can be observed (Aceves, Wabnitz, 1989).

The nonlinear waveguides and periodical nonlinear structures exhibit attractive properties that make them suitable for utilizing in all-optical ultrafast application and novel devices development with wavelength tunable characteristics. The numerical simulations of these devices therefore are of great importance. Usually computer simulations for investigation the nonlinear pulse propagation in Bragg gratings are based on the numerical solution of the nonlinear Schrödinger equation (De Sterke, Sipe, 1995). In our work the Finite-Difference-Time-Domain (FDTD) method is applied because it is straightforward solution of six-coupled field components of Maxwell's equations.

The model of the two-dimensional nonlinear periodic structure consisting of alternating layers of Kerr nonlinear media is shown in Fig. 1. The waveguide width is  $2a = 1$  mm, the period of structure  $d = 1$  mm, the linear part of layers refractive indices  $n_1 = 1.45$ ,  $n_2 = 2.0$ . The layers consist of the media with positive Kerr-like nonlinearity

$$n_{l,II} = n_{l,2} + n_{nl} |E|^2,$$

where  $n_{nl} = 3 \cdot 10^{-8}$  mm<sup>2</sup>/W – the nonlinear additive to the linear part of refraction index of silica glass. So the nonlinear media with instantaneous third-order nonlinearity responses are analyzed. The wave propagates along the  $x$ -direction. The structure is surrounded by vacuum with the refractive index  $n = 1$ . The input signal was set in the  $x_1$  plane, which was placed in the lead-in waveguide domain with the refractive index  $n_0 = (n_1 + n_2)/2$ .

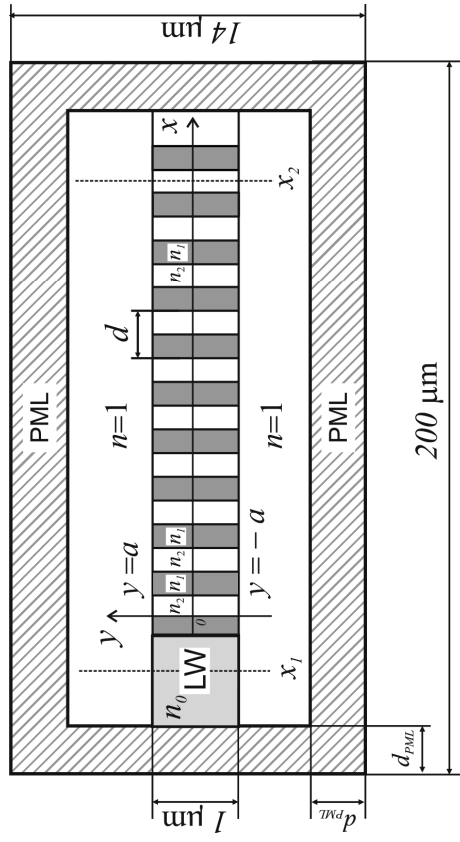


Figure 1. Schematic diagram of the nonlinear Bragg grating model. A perfectly matched layers surround the system. LW – the lead-in waveguide.

For calculations we utilize the FDTD numerical simulation method (Taflove, Hagness, 2005). The FDTD method has been widely used for solving the problems of the electromagnetic wave propagation in different media, because it is a straightforward solution of six-coupled field components of Maxwell's equations. This method is based on Yee's algorithm (Yee, 1996) and computes the electric and magnetic field components by discretizing the Maxwell's equations both in time and space domain and then solving the system of the discretized equations in a time marching sequence by alternatively calculating the electric and magnetic fields in the computational domain.

The free electromagnetic code from the MIT MEEP package (Oskooi, 2010) was used to perform the FDTD computational method. To simulate wave propagation in an unbounded medium the perfectly matched layer (PML) absorbing boundary conditions was applied. The PML has been shown to be one of the most effective boundary condition because it can truncate the simulation space without artificial reflections. Inside the PML domain each field component splits into two subcomponents and the system of the discretized Maxwell's equa-

tions slightly modifies. In the Fig. 1 the PML regions are depicted with hatching. The computational domain size was chosen to be  $200 \times 14$  mm, the size of dielectric periodic structure was  $200 \times 1$  mm, the number of periods was 190. The thickness of the PML on all boundaries of computational domain was equal to  $d_{PML} = 30 \cdot \Delta x = 3$  mm. The cell size was chosen as  $\Delta x = \Delta y = 0.1$  mm, the time step was taken as  $\Delta t = 8 \cdot 13 \cdot 10^{-7}$  s and the value of Courant stability factor was taken to be  $S = 0.5$  that satisfy the numerical stability of the method.

Computation of the transmission spectrum was performed by FDTD method. The propagation of the Gaussian pulse with center frequency  $f_c = 6.3102 \cdot 10^{14}$  Hz and pulse width  $\Delta f = 2.072 \cdot 10^4$  Hz through the Bragg grating was considered. The parameter of the initial Gaussian pulse was chosen to overlay the first photonic band gap of the investigated structure. The amplitude of pulse was chosen to be  $A = 1$ , so the nonlinear effects was negligibly small.

The time-domain response of the transmitted electromagnetic field was monitored inside the Bragg grating in the plane  $x_2$ , which is shown in the Fig. 1. The Fast Fourier Transform of the monitored data in the plane  $x_2$  was performed to obtain the spectra of the time-domain responses. The result of this simulation is plotted in Fig. 2, where  $T(f)$  is the transmission coefficient which defines the amplitude of a transmitted wave relative to an incident wave,  $f$  is the frequency of electromagnetic wave.

Here we consider the CW signal propagation through Bragg grating. The nonlinear dynamics of CW signal propagation in the structure was studied in detail near the upper branch of the photonic band gap, where the dispersion is anomalous and the criterion of modulation instability (Agrawal, 2007) is satisfied. The modulation instability near the top branch of band gap is similar to that in the nonlinear Schrödinger equation (De Sterke, 1998).

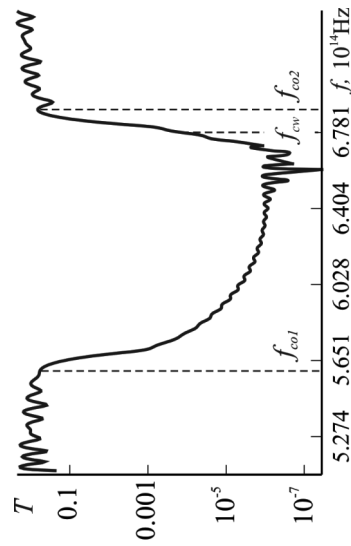


Figure 2. The transmission spectrum through the Bragg grating of the Gaussian pulse with the central frequency  $f_c = 6.3102 \cdot 10^{14}$  Hz and the width  $\Delta f = 2.072 \cdot 10^4$  Hz.

The form of the CW signal was chosen as

$$E_z(\gamma, t) = A \cdot E_{FM}(\gamma) \sin(2\pi f_{CW} t),$$

where  $f_{CW} = 6.78115 \cdot 10^{14}$  Hz is the signal frequency,  $E_{FM}(\gamma)$  is the mode profile of the fundamental TE mode of the planar waveguide (Haus, 1985). This frequency value is located near the cut-off frequency  $f_{co2}$  as shown in Fig. 2. A series of simulations was performed with the different value of the amplitude of the input signal denoted by  $A$ . When the power of source and therefore amplitude  $A$  is small, the electromagnetic wave exponentially decays as it propagates along the structure, as shown in Fig. 3. Here the distribution of the field component  $E_z(x)$  along the system is plotted. The time moment, at which the steady-state regime begins, was shown.

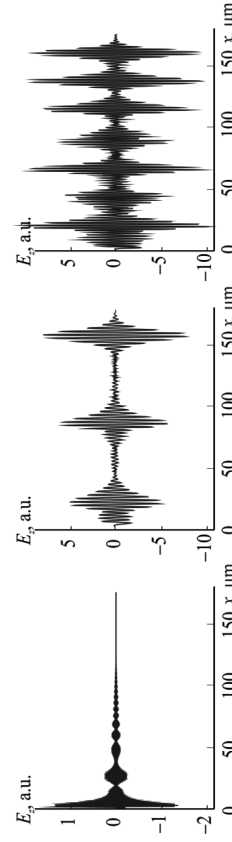


Figure 3. The distribution of the field component  $E_z(x)$  along the Bragg grating with the different amplitude values of CW input signal:  $A = 1$  (a),  $A = 7$  (b) and  $A = 10$  (c).

The relatively low value of the nonlinear coefficient  $n_n$  and small value of signal amplitude correspond to the linear system and the influence of nonlinear effects is therefore negligibly small.

It was demonstrated that increasing the input signal amplitude one can obtain the signal propagation along the periodical structure. This can be explained as the transformation of the band structures of the periodic nonlinear system and the nonlinear frequency shift. In the Fig. 3b the propagation of the signal with amplitude  $A = 7$  is shown. Moreover the signal profile inside Bragg grating is specifically modulated and the formation of multiple gap-solitons is observed. If the amplitude of initial signal reached a threshold value, the gap-soliton is formed, however as the intensity is increased more gap-solitons are generated. In Fig. 3c the CW signal with amplitude  $A = 10$  was set in the  $x_1$  plane in the lead-in waveguide. The number of the generated gap-solitons per system length is increased in this case.

In the Fig. 4 the spatio-temporal dynamics of CW signal propagation are demonstrated. The frequency of CW signal used in this simulation was chosen to be similar to the previous computation of the field distribution along the system. If the amplitude is below the threshold of gap-soliton formation the signal decays along the system, as shown in Fig. 4a. When the amplitude of initial signal was

chosen to be  $A = 7$ , the train of gap-solitons was formed. This dynamics of soliton generation is demonstrated in Fig. 4b. When the amplitude gets larger ( $A = 15$  in the Fig. 4c), the interaction between gap-solitons is observed at the time  $t > 15$  ps.

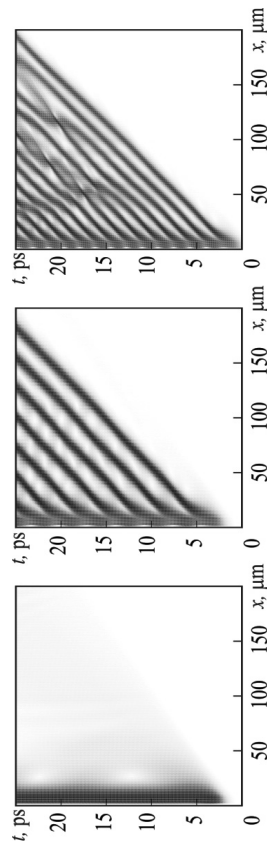


Figure 4. The spatio-temporal distribution of the field component  $E_z(x)$  along the Bragg grating with the different amplitude values of CW input signal:  $A = 6$  (a),  $A = 7$  (b) and  $A = 15$  (c).

The maximum value of the nonlinear additive ( $n_n |E|^2$ ) to the linear part of refraction index in the numerical simulation was approximately 5 %. At this intensities of total launched power of light the structure of real Bragg grating doesn't suffer permanent damage. The common method of reduction the threshold intensities for nonlinear effects near the band gap region is the fabrication of Bragg gratings of increased length and using the chalcogenide glasses (Hilton, 1966).

In conclusion, the dynamic of the electromagnetic wave propagation in 2D nonlinear Bragg grating was numerically studied. The estimation of the cut-off frequencies in periodical structure, which is confined in the transverse direction, was performed with the FDTD method. The possibility of CW signal propagation with the frequency within photonic band gap range was demonstrated by FDTD simulation. The process of soliton tunneling in nonlinear 2D Bragg grating has been observed. The multiple gap-soliton formation was investigated. The interaction between gap-solitons is observed, however we do not pursue a detailed analysis of this phenomenon here.

We acknowledge fruitful discussions with Nikita M. Ryskin. This work was supported by the Russian Foundation for Basic Research Grant No. 10-02-01403 and the Ministry of Education and Science of the Russian Federation Grant No.2.1.1/1738 in a frame of program of Development of Scientific Potential of Higher Education.

## REFERENCES

- 1 Aceves A.B., Wabnitz S. Self-induced transparency solitons in nonlinear refractive periodic media // Phys. Lett. A. 1989. Vol. 141. P. 37-42.

- 2 *Agrawal G.P.* Nonlinear Fiber Optics. Academic Press, Boston, 2007.
- 3 *Broderick N.G.R., Richardson D.J., Ibsen M.* Nonlinear switching in a 20-cm-long fiber Bragg grating // Opt. Lett. 2000. Vol. 25. P. 536.
- 4 *De Sterke C. M.* Theory of modulation instability in fiber Bragg gratings // J. Opt. Soc. Am. B. 1998. Vol. 15. P. 2660-2667.
- 5 *De Sterke C.M., Sipe J.E.* Gap solitons // Progress in Optics. 1995. Vol. 33. P. 203-260.
- 6 *Haus H.A.* Waves and Fields in Optoelectronics. Prentice-Hall, Englewood Cliffs, N.J., 1985. P. 188-190.
- 7 *Hilton A.R.* Nonoxide Chalcogenide Glass as Infrared Optical Materials // Appl. Opt. 1966. Vol. 5. P. 1877-1882.
- 8 *Oskooi A.F., Roudny D., Ibanescu M., Bermel P., Joannopoulos J.D., Johnson S.G.* MEEP: A flexible free-software package for electromagnetic simulations by the FDTD method // Computer Physics Communications. 2010. Vol. 181. P. 687-702.
- 9 *Romero R., Frazao O., Floreani F.* Multiplexers and Demultiplexers Based on Fibre Bragg Gratings and Optical Circulators for DWDM Systems // Lecture Notes in Computer Science. 2003. No. 2720. P. 442-451.
- 10 *Siegeman G.I., Wright E.M.* All-optical waveguide switching // Opt. and Quant. Electron. 1990. Vol. 22. P. 95-122.
- 11 *Sumetsky M., Eggleton B.J.* Fiber Bragg gratings for dispersion compensation in optical communication systems // Journal of Optical and Fiber Communications Research. 2005. Vol. 2. P. 256-278.
- 12 *Taflove A., Hagness S.C.* Computational Electrodynamics: The Finite-Difference Time-Domain Method. Artech House, Norwood. 2005.
- 13 *Taverner D., Broderick N.G.R., Richardson D.J., Lanning R.I. and Ibsen M.* Nonlinear self-switching and multiple gap-soliton formation in a fiber Bragg grating // Optics Lett. 1998. Vol. 23. P. 328-330.
- 14 *Yarivchuk I.Ya., Fitio V.M., Bobitski Ya.V.* Narrowband filters of new type for infra red spectral region // Radioelectronics and Communications Systems. 2008. Vol. 51. P. 339-344.
- 15 *Yee K.S.* Numerical solution of initial boundary value problems involving Maxwell's equation in isotropic media // IEEE Transaction on Antennas and propagation. 1996. Vol. 14. P. 302-307.
- 16 *Yu F.T.S., Yin S.* (Eds.) Fiber Optic Sensors. CRC Press, New York. 2008.
- 2 differential cross section which can be represented (A. Huetz, P. Selles, D. Waymel, and J. Mazeau, 1991) via gerade and ungerade amplitudes:
- $$\frac{d^3\sigma}{dE_1 d\alpha_1 d\alpha_2} = |a_g(E_1, E_2, \theta_{12})(\cos\theta_1 + \cos\theta_2) + a_u(E_1, E_2, \theta_{12})(\cos\theta_1 - \cos\theta_2)/2|, \quad (1),$$
- where  $E_1$  and  $E_2$  are energies of the ejected electrons,  $\theta_{12}$  is an angle between directions of ejection, and the ungerade amplitude  $a_u = 0$  for  $E_1 = E_2$ . The gerade amplitude  $a_g$  is usually referred to as the correlation parameter. Following the Wannier's theory (G.H. Wannier, 1953), it has the Gaussian shape (A.R.P. Rau, 1976):
- $$a_g(E_1, E_2, \theta_{12}) \approx A \exp[-2 \ln 2 \frac{(\theta_{12}-\pi)^2}{\gamma^2}] \quad (2),$$
- with the Gaussian width parameter equal to
- $$\gamma = \gamma_0 E^{1/4} \quad (3),$$
- where  $E = E_1 = E_2$  is the energy excess above the double-ionization threshold, and the scaled Gaussian width  $\gamma_0$  depends on the choice of the hyperradius of the boundary between the Coulomb and free zones. Coulomb zone is where the potential energy of the interaction between the electrons and the ion is much larger than  $E$ , and the free zone is where  $E$  is much larger than the Coulomb potential. The Coulomb zone, the free zone, and also the reaction zone (where the electrons start) are three zones which Wannier allocated having divided the space surrounding ion in his work.
- By analogy with the Wannier threshold law for the cross section, Eq. (3) is also commonly referred to as the Wannier threshold law, although Wannier himself has no direct relation to it. The Gaussian width parameter  $\gamma$  is a single-angle parameter describing the angular distribution. When  $\gamma$  is large, the interelectron correlation is weak, and vice versa; therefore, it is often used for the analysis of the strength of angular interelectron correlation.
- In spite of the fact that the energy range, where Eq. (3) is valid, is not established, experimenters and theorists often use Eq. (3) for the data interpretation, trying to find the scaled width parameter. Many formulas for have been proposed by various authors (S. Oranto and C.R. Garibotti, 2005). However, Kazansky and Ostrovsky (A.K. Kazansky and V.N. Ostrovsky, 1993) reduced the problem by a change of variable to the wave-packet evolution in a harmonic oscillator with time-dependent frequency and showed that the packet width has no time to follow adiabatically the oscillator frequency as a result of the deceleration of electrons by the nucleus field. This contradicts the assumption used in (A.R.P. Rau, 1976) to obtain (3), and when the nonadiabaticity is taken into account, the near-threshold behavior of Gaussian width is strongly modified. They also showed that the assumption about the presence of the only oscillator ground mode at the boundary of the reaction zone is not true and,

VALIDITY OF THE WANNIER THRESHOLD LAW FOR ANGULAR CORRELATION WIDTH IN DOUBLE PHOTOIONIZATION OF ATOMS  
**T.A. Sergeeva, V.V. Serov**  
Saratov State University  
In our previous work (T.A. Sergeeva, V.V. Serov, V.L. Derbov, 2010) we explored the double photoionization phenomena, the fundamental process which interelectron correlations act in. It can be described using the three-fold

therefore,  $a_g(\theta_{12})$  depends on the details of the process inside the reaction zone and can have non-Gaussian shape even at  $E \rightarrow 0$ . Moreover, it has been found previously (V.V. Serov, V.I. Derbov, B.B. Joulakian, and S.I. Vinitsky, 2008) that  $\gamma$  for the hydrogen negative ion H<sup>-</sup> starts to grow with energy decreasing at low energies, in obvious contradiction with the Wannier threshold law. So we explored this gamma dependence in detail.

## II. The calculations.

Like in the previous works, we used the TDCC method described in (T.A. Sergeeva, V.V. Serov, V.L. Derbov, 2010). At the present stage the 3DCS and  $\gamma$  were calculated for the helium in the ground state and the negative hydrogen ion H<sup>-</sup>. During the calculations we used the following numerical scheme parameters: the angular basis parameter  $l_{2,\max} = 25$ , the uniform radial grid with  $N_r = 500$  and the size  $\zeta_{\max} = 30^\circ$ , the complex scaling radius  $\zeta_{sc} = 22.5^\circ$ , the complex scaling angle  $\theta_{cs} = 30^\circ$ , and the grid expansion rate  $a_\infty = 0.1$ . The evolution was simulated up to the time  $t_{\max} = 12800$ . For H<sup>-</sup> other radial grid parameters are used:  $N_r = 500$ ,  $\zeta_{\max} = 50^\circ$ ,  $\zeta_{sc} = 45^\circ$ ,  $a_\infty = 0.05$ .

## III. Results and discussion.

At first, consider our first well-known result for Gamma for helium double photoionization.

Except for the perfect agreement of our results with the experimental data (in comparison with other methods results), we should note the shape of the  $\gamma$  curve. Figure 1 is presented in logarithmic scales at both axes, in which the power dependences such as the Wannier law (3) should look like sloping straight lines. Indeed, we see that our plots are close to straight lines when  $E$  is less than a few electronvolts. However, the exponent is not equal to  $1/4$  at all. The approximation of the  $\gamma(\sigma^2)$  curve in the E range from 0.1 to 2 eV, using the power law of the general form

$$\gamma = \tilde{\gamma}_0 E^s \quad (5)$$

through the least-squares approach, yields the exponent  $s=0.097$  and the proportionality constant  $\tilde{\gamma}_0 = 70^\circ \text{ eV}^{-s}$ . Such a significant deviation from the Wannier threshold law, which is often used for the interpretation of experimental and theoretical data, seems to be discouraging.

In Fig. 2, we show the scaled width parameter  $\gamma_0(E) = \frac{\gamma(E)}{E^{1/4}}$  in comparison with the curve obtained in (A.K. Kazansky and V.N. Ostrovsky, 1993) using the quadratic approximation of the interelectrons potential in  $(\theta_{12} - \pi)$  and the semiclassical approximation for radial motion. We also take into account the nonadiabaticity of the wave-function angular dependence on the hyperradius and the suggestion that only the lowest mode in  $\theta$  is populated at the boundary of the reaction zone with the hyperradius assumed to be  $R=4$ , which we

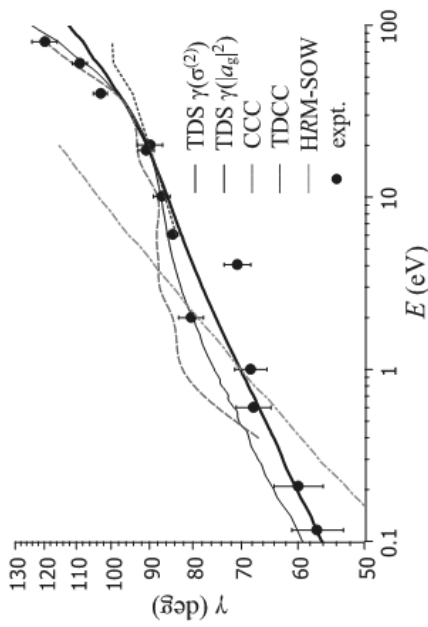


Fig. 1. The Gaussian width parameter  $\gamma$  as a function of the full energy of ejected electrons  $E$  for the photoionization of He; our results were obtained by the fitting of  $\sigma(2)$  ( $\theta_{12}$ ) (thick solid line) and  $|a_g(\theta_{12})|^2$  (thin solid line), along with CCC results (A.S. Kheifets and I.Brav, 2006) (dashed line), TDCC results (M. Foster and J. Colgan, 2006) (dotted line), HRM-SOW results (L. Malegat, P. Selles, and A.K. Karanthy, 1999) (dash-dotted line), and experimental data (A.Huetz and J. Mazeau, 2000; G. Turni, L. Avaldi, P. Bolognesi, R. Camilloni, M. Coreno, J. Berakdar, A.S. Kheifets, and G. Stefani, 2002) (filled circles).

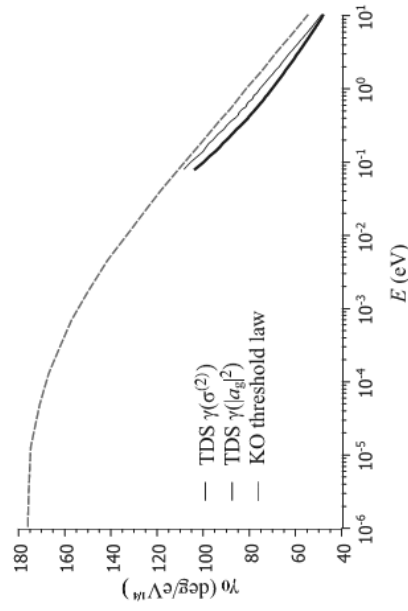


Fig. 2. The scaled width parameter as a function of E for He: our results were obtained with the fitting of  $\sigma(2)$  ( $\theta_{12}$ ) (thick solid line)  $|a_g(\theta_{12})|^2$  (thin solid line), along with the Kasansky-Ostrovsky threshold law (A.K. Kazansky and V.N. Ostrovsky, 1993) (dashed line).

will refer to as the Kasansky-Ostrovsky (KO) threshold law. It is clear that our curves are close to the KO threshold law curve, down to the minimal energy value  $E=0.1$  eV attained here. In Fig. 2, the Wannier threshold law (3) would look like a horizontal straight line. At very low energies of the order of  $10^{-5}$  eV, the KO curve seems to become horizontal, but this is just because the energies below  $10^{-6}$  eV are not shown in the figure, as follows from (A.K. Kazansky and V.N. Ostrovsky, 1993). Following the KO threshold law,  $\gamma_0(E)$  oscillates when energy decreases with the period, which is constant in the logarithmic scale (A.K. Kazansky and V.N. Ostrovsky, 1993) (in Fig. 2, only a half of the period is shown) and never turns into the Wannier threshold law.

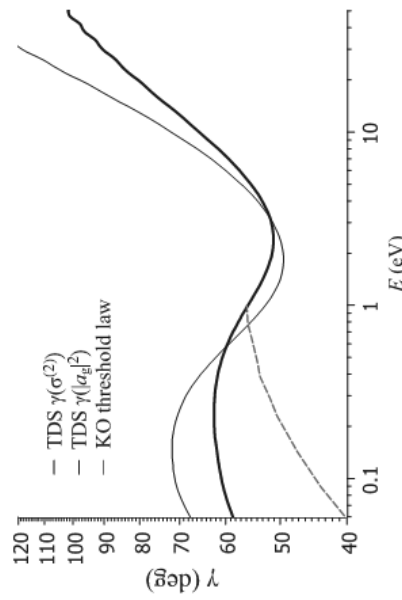


Fig. 3. The Gaussian width  $\gamma$  as a function of  $E$  for the photoionization of  $H^-$ : our results were obtained by the fitting of  $\sigma^{(2)}(\theta_{12})$  (thin solid line) and  $a_g^{(2)}(\theta_{12})^2$  (thick solid line) along with the Kasansky–Ostrovsky threshold law (A.K. Kazansky and V.N. Ostrovsky, 1993) (dashed line).

Then we explored the  $\gamma$  dependence on  $E$  for the negative hydrogen ion, for which we previously observed the  $\gamma$  increase for energies below 2.5 eV, in contradiction to the Wannier law. It is clear from Fig. 3 that derivative of  $\gamma(\sigma^{(2)})$  with respect to the energy is negative in the energy range from 2.6 to 0.23 eV. At energies below 0.09 eV,  $\gamma(\sigma^{(2)})$  appears to be a power function of the energy with the exponent  $s=0.083$  and  $\tilde{\gamma}_0 = 74^\circ eV^{-s}$ , however, the energy range is too small to treat this conclusion as a rigorous one.

Figure 4 demonstrates a clear-cut distinction between our results and the KO threshold law for the nuclear charge  $Z=1$  (A.K. Kazansky and V.N. Ostrovsky, 1993), unlike the helium case (Fig. 2). We should note that the  $\gamma(E)$  dependence obtained by Kasansky and Ostrovsky is monotonous (Fig. 3), despite the  $\gamma_0(E)$  dependence oscillating. Here we should note that the KO curve is obtained from the assumption that, at the boundary of the reaction zone, only

the ground angular mode is populated; but, in the same work (A.K. Kazansky and V.N. Ostrovsky, 1993), it is shown that it is not necessary at all, even at  $E \rightarrow 0$ , and at the boundary of the reaction zone, the wave-function angular dependence may have an arbitrary width or even be non-Gaussian, depending on the details of the process inside the reaction zone. Our hypothesis is that this special feature of  $H^-$ , compared with helium and helium-like ions (V.V. Serov, V.L. Derbov, B.B. Joukian, and S.I. Vinitsky, 2008), comes from the fact that the  $H^-$  bound-state configuration is strongly different from that of the helium ground state.  $H^-$  is a deuteron-like weakly bound system consisting of a hydrogen atom and an electron, spending the most time outside the region where the attracting potential acts. That is the obvious distinction from the helium.

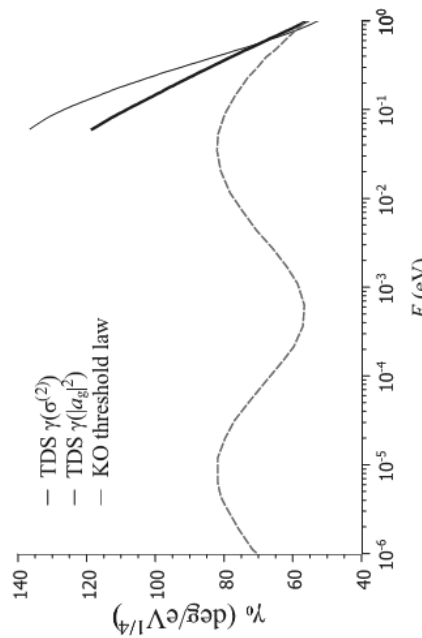


Fig. 4. The scaled width parameter as a function of  $E$  for  $H^-$ : our results were obtained by the fitting of  $\sigma^{(2)}(\theta_{12})$  (thin solid line) and  $a_g^{(2)}(\theta_{12})^2$  (thick solid line), along with the Kasansky–Ostrovsky threshold law (A.K. Kazansky and V.N. Ostrovsky, 1993) (dashed line).

#### IV. Conclusion.

We calculated using the *ab initio* method the Gaussian width  $\gamma$  dependence on the energy  $E$  of electrons in the double photoionization of the negative hydrogen ion  $H^-$  and the helium in the ground  $1s^2$  state. For the He ( $1s^2$ ) photoionization, our results are in perfect agreement with experimental data, but indicate that the well-known Wannier threshold law  $\gamma \sim E^{1/4}$  is not correct, even for sufficiently small excess energies of about 0.1 eV. It is shown that the  $\gamma$  dependence on the energy is much better described by the law obtained by Kasansky and Ostrovsky, where the influence of the electrons' deceleration by the nucleus field is properly taken into account. Their law is strongly different from the Wannier threshold law at any values of the excess energy, even at extremely low ones, and, therefore, the Wannier threshold law is meaningless in the interpretation of experimental and theoretical angular distribution data.

Acknowledgements  
This work was supported by the President of Russian Federation Grants No. MK-2344.2010.2 and No. RFBR 08-01-00604a.

#### REFERENCES

1. M. Foster and J. Colgan, *J. Phys. B* 39, 5067 (2006).
2. A. Huetz and J. Mazeau, *Phys. Rev. Lett.* 85, 530 (2000).
3. A. Huetz, P. Sellez, D. Waymel, and J. Mazeau, *J. Phys. B* 24, 1917 (1991).
4. A.K. Kazansky and V.N. Ostrovsky, *J. Phys. B* 26, 2231 (1993).
5. A.S. Kheifets and I. Bray, *Phys. Rev. A* 73, 020708(R) (2006).
6. L. Malegat, P. Sellez, and A.K. Kazansky, *Phys. Rev. A* 60, 3667 (1999).
7. S. Ostranto and C.R. Garibotti, *Phys. Rev. A* 71, 034703 (2005).
8. A.R.P. Rau, *J. Phys. B* 9, L283 (1976).
9. T.A. Sergeeva, V.V. Serov, V.L. Derbov, Presenting academic achievements to the world, p.120-125 (2010).
10. V.V. Serov, V.L. Derbov, B.B. Joulakian, and S.I. Vinitsky, *Phys. Rev. A* 78, 063403 (2008).
11. G. Turri, L. Avaldi, P. Bolognesi, R. Camilloni, M. Coreno, J. Berakdar, A.S. Kheifets, and G. Stefanini, *Phys. Rev. A* 65, 034702 (2002).
12. G.H. Wannier, *Phys. Rev.* 90, 817 (1953).

#### NUMERICAL SIMULATION OF ENVELOPE SOLITONS IN MAGNON CRYSTALS BASED ON SYSTEM OF NONLINEAR SCHRÖDINGER EQUATIONS

**S. E. Sheshukova**

Saratov State University

Investigations of the envelope solitons represent a great interest. This type of solitons (localized wave packets) can be formed from a pulses propagating in different medium with nonlinearity and dispersion (Akhmediev, Ankiewicz, 1997). A new type of solitons, called Bragg soliton, or the gap solitons can be formed in nonlinear media whose properties vary periodically in the definite direction with length (Malomed, 2006). The photonic crystals are an example of such media in optics. In this structure the refractive index is a periodic function of spatial coordinates (Kivshar, Agrawal, 2003). The investigation of Bragg solitons are of interest not only from a fundamental point of view, but also have great potential for practical use of such structures in telecommunications systems, in optical communication lines (Agrawal, 2005).

In recent years, due to advances in the technology of thin-film magnetic materials raising and a new approaches to obtain periodic structures the

production of crystals, based on the magnetic materials — magnon crystals (such as photonic crystal) represent a great interest. The magnon crystals where spin waves propagate are similar to the photonic crystal (Lyubchanskii et al., 2003; Гуляев и др., 2003). The magnon crystals have a number of significant advantages compared to the photonic crystals. The nonlinear effects in ferromagnetic films appear at relatively low power levels (Гуляев и др., 2003).

The magnon crystals by analogy with the photonic crystals demonstrate more interesting nonlinear phenomena in comparison with the effects observed in homogeneous ferromagnetic films. However, we can conclude that the nonlinear processes in such periodic structures, including those associated with the peculiarities of formation of solitons are investigated insufficiently. You can specify only some work in this direction (Niu-Niu Chen et al., 1993; Григорьев и др., 2008; Дроздовский и др., 2010), which shows the experimental and numerical simulation results based on a one-dimensional nonlinear Schrödinger equation (NSE). The coefficients of dispersion and nonlinearity, which were calculated based on the assumption that only one magnetostatic wave propagates in the ferromagnetic film. The dispersion of this wave depends on the parameters of the periodic structure.

The aim of this work was to investigate the features of formation the solitons are similar to a Bragg solitons in the ferromagnetic one-dimensional periodic structure. The system of coupled nonlinear Schrödinger equations for the amplitude envelope of the forward and backward waves was used for numerical simulation. We pay great attention to the conditions of formation of solitons, such as Bragg or gap solitons.

A one-dimensional periodic ferromagnetic structure (magnon crystal) was considered. The structure is infinite in the direction of the  $x$  and  $y$ . The constant magnetic field is applied perpendicular to the film plane. The value of this field  $\vec{H}_0$  was chosen in such a way that the forward volume MSW (FVMSW) propagated in the  $y$  direction.

To construct a nonlinear model of the periodic ferromagnetic structure use, similar to optical systems (Kivshar, Agrawal, 2003; Agrawal, 2005), coupled-wave approximation and represent the distribution of the magnetostatic potential near the gap as the sum of forward and backward waves:

$$\psi(y, t) = \varphi_f(y, t) \exp(i(\omega t - K_B y)) + \varphi_b(y, t) \exp(i(\omega t + K_B y)), \quad (1)$$

where  $\varphi_f(y, t)$ ,  $\varphi_b(y, t)$  are slowly varying complex envelopes of the forward (incident) and backward (reflected) waves, respectively.

Taking (Kivshar, Agrawal, 2003) into account for the approximation of weak nonlinearity, the nonlinear equations for the envelopes of direct and reflected waves can be represented as:

$$\left\{ \begin{array}{l} i \left( \frac{\partial \Phi_f}{\partial t} + V_g \frac{\partial \Phi_f}{\partial y} \right) - \beta \frac{\partial^2 \Phi_f}{\partial y^2} + \eta \Phi_f + \chi \Phi_b + \gamma \left( |\Phi_f|^2 + 2|\Phi_b|^2 \right) \Phi_f = 0 \\ i \left( \frac{\partial \Phi_b}{\partial t} - V_g \frac{\partial \Phi_b}{\partial y} \right) - \beta \frac{\partial^2 \Phi_b}{\partial y^2} + \eta \Phi_b + \chi \Phi_f + \gamma \left( |\Phi_b|^2 + 2|\Phi_f|^2 \right) \Phi_b = 0 \end{array} \right. , \quad (2)$$

where  $V_g$  is the group velocity,  $\eta = \omega_0 - \omega_B$  is the detuning ( $\omega_B = K_B V_{ph}$ ,  $V_{ph}$  is the MSW phase velocity in homogenous structure),  $\beta$  is the coefficient of dispersion,  $\chi$  is the coefficient of coupling,  $\gamma$  is the nonlinear coefficient.

Equations (2) are similar to the system of two coupled nonlinear Schrödinger equations describing the propagation of the direct and reflected waves in Bragg optical lattices (Malomed, 2006; Agrawal, 2005). It should be noted that the system (2) without taking into account the dispersion ( $\beta=0$ ), as shown in the (Kivshar, Agrawal, 2003), may have soliton solutions — the family of Bragg solitons. This type of soliton represents a combination of two waves moving together or remaining in place. If  $\Phi_f(y, t) = \Phi_b(y, t)$  soliton does not move — a stationary gap soliton.

The results relating to the formation of solitons in this system were obtained based on the numerical solution of the coupled system of the NSE (2) using a SSFM method (Kivshar, Agrawal, 2003). We consider the features of the wave evolution at a fixed value  $V_g$  depending on the parameter  $\chi$ . This parameter characterizes the geometrical parameters of the periodic structure and the relationship between the forward and backward waves, accordingly. The other coefficients in (2) were calculated:  $\beta = -2 \cdot 10^4 \text{ cm}^2 \cdot \text{s}^{-1}$ ,  $\gamma = 3 \cdot 10^{10} \text{ s}^{-1}$ ,  $\eta = 1 \cdot 10^6 \text{ s}^{-1}$ .

We consider the case when the input amplitude of the forward and backward waves are not zero  $\Phi_{0f} = \Phi_{0b} = \Phi_0 \exp(-y^2/y_{imp}^2)$ , where  $y_{imp}$  is the pulse width,  $\Phi_0$  is the dimensionless pulse amplitude during the initial moment of time which got out above a soliton threshold. In this excitation method the parameter space  $(V_g, \chi)$  corresponding to the soliton formation with a different features is shown in Fig. 1. The gray area in Fig. 1 corresponds to the formation of pulses localized on the limited length of the structure. This area corresponds to the finite values of  $V_g$  when  $\chi = 0$ . The existence of the localized solitons without a linear relationship between the waves ( $\chi = 0$ ) is explained by the so-called locking effect due to the nonlinear coupling between waves only. In this case, pulses moving in different directions at large amplitudes and relatively small values of  $V_g$  can capture each other and then move with zero velocity.

We consider the features of the wave evolution at a fixed value  $V_g$  depending on the parameter  $\chi$ . For the parameters corresponding to point 1 on Fig. 1 at small values of  $\chi$  the energy exchange between the waves is small and the

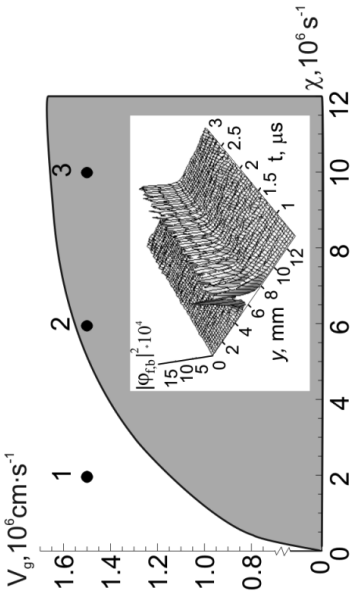


Fig. 1. The parameter space  $(V_g, \chi)$ , corresponding to envelope solitons formation  $\Phi_{0f} = \Phi_{0b} = 0.04$ . Insert shows the spatio-temporal evolution of the envelope amplitude  $\Phi_f$  and  $\Phi_b$  for point 3 ( $\chi = 10 \cdot 10^6 \text{ s}^{-1}$ ,  $V_g = 1.5 \cdot 10^6 \text{ cm} \cdot \text{s}^{-1}$ ).

pulses on the forward and the backward wave move in different directions (see Fig. 2). With increasing  $\chi$  (point 2 in Fig. 1) pulse excited on the forward wave moves at first in the positive direction of  $y$ -axis (Fig. 2 c – right half-

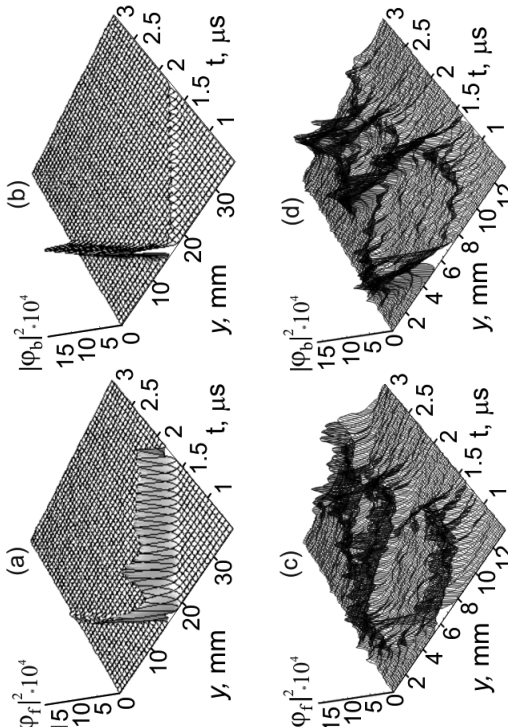


Fig. 2. The spatio-temporal evolution of the envelope amplitude  $\Phi_f$  (a) and  $\Phi_b$  (b) at  $\chi = 2 \cdot 10^6 \text{ s}^{-1}$  (point 1 in Fig. 1),  $\Phi_f$  (c) and  $\Phi_b$  (d) at  $\chi = 6 \cdot 10^6 \text{ s}^{-1}$  (point 2 in Fig. 1)  $V_g = 1.5 \cdot 10^6 \text{ cm} \cdot \text{s}^{-1}$ .

3. Дроzdовский А.В., Черкасский М.А., Устинов А.Б., Козырев Н.Г., Калинокс Б.А. Образование солитонов опибающей при распространении спин-волновых пакетов в тонкопленочных магнитных кристаллах // Письма в ЖЭТФ. 2010. Т. 91, №.1. С. 17-22.
4. Agrawal G.P. Lightwave Technology: Telecommunication Systems; New Jersey: John Wiley and Sons, Inc., 2005. 315 p.
5. Akhmediev N.N., Ankiewicz A. Solitons. Nonlinear pulses and beams. London: Chapman and Hall, 1997. 299 p.
6. Kivshar Yu.S., Agrawal G.P. Optical Solitons: From Fibers to Photonic Crystals; San Diego: Academic Press, 2003. 520 p.
7. Lyubchanskiy I.I., Didenkova N.N., Lyubchanskiy M.I., Shapovalov E.A. and Rasing T. Magnetic photonic crystals // J. Phys. D: Appl. Phys. 2003. V. 26. P. 277 – 287.
8. Malomed B.A. Soliton management in periodic systems; New-York: Springer, 2006. 192 p.
9. Niu-Niu Chen, Slavkin A.N., Cottam M.G. Gap solitons in periodic structures: Modulated magnetic thin films // Phys. Rev. B. 1993. Vol. 47. P. 8667 – 8671.

plane) and eventually transferred to the pulse on the backward wave moving in the same direction (Fig. 2 d – right halfplane). After a time interval  $T/2$  (as soon as the power pulses on the forward and backward waves turns equal), the pulses stop. Then they continue moving in the negative direction of  $y$ -axis, because the pulse power on the backward wave becomes more. However, the pulse excited initially on the backward wave begins moving in the negative direction of  $y$ -axis and eventually it pumps to the pulse on the forward wave. Then both pulses stop and continue moving in the positive direction of  $y$ -axis (see Fig. 2 c, d – left halfplane). There is a symmetrical dynamic of the pulses on the forward and backward waves, the pulses remain localized in space and their combination behaves as a Bragg soliton. The dynamics of pulses formation for the parameters corresponding to point 3 in Fig. 1 is shown in an insert in Fig. 1. With increasing  $\chi$  period  $T$  decreases, the pulses change their direction frequently and the area, in which pulses localized, compressed. As a result, one solution on the forward and one soliton on the backward wave are formed and come to stand still, i.e.  $V = 0$ .

In this paper, the model based on coupled nonlinear Schrodinger equations for the envelope amplitude forward and backward waves was used to calculate the parameter spaces corresponding to solitons, similar Bragg solitons with different properties. In particular, the basic mechanism of formation of soliton, similar Bragg soliton, and localized on the limited length of structure, is mutual capture of pulses on forward and backward waves, which move with the cumulative velocity (velocity, in turn, it is defined by relative power of two waves), and presence of power swapping between forward and backward waves which is defined by value coupling between waves. Features of wave evolution depending on coupling parameter and group velocity and the areas of parameters corresponding to formation of pulses, similar to Bragg solitons and localized on the limited length of structure, are investigated.

#### Acknowledgments

This work was supported by Ministry of Education and Science of Russian Federation Grant #2.1.1/2695 in a frame of program “Development of Scientific Potential of Higher Education” and Federal Targeted Programme “Scientific and scientific-pedagogical cadres of Innovative Russia” for 2009–2013 (project #2010-1.2.2-123-019-002)

#### REFERENCES

1. Григорьев Н.Ю., Устинов А.Б., Калинокс Б.А. Наблюдение солитонов огибающей спиновых волн в периодических магнитных пленочных структурах // Письма в ЖЭТФ. 2008. Т. 88, №.1. С. 34-39.
2. Гуляев Ю.Б., Никитов С.А., Жиготовский Л.В. и др. Ферромагнитные пленки с периодическими структурами с магнитной запрещенной зоной – магнитные кристаллы // Письма в ЖЭТФ. 2003. Т. 77, № 10. С. 670 – 674.

## THE SYNTHESIS OF CARBON NANOTUBES USING LIQUID CATALYSTS

**E. A. Tarasov, Z. I. Buyanova, M. V. Samarsky**

Saratov Branch of Kotelnikov Institute of Radio Engineering  
and Electronic of Russian academy of sciences

#### Introduction

Carbon nanotubes (CNTs) are promising materials for applications to nanoscale devices, including energy storage and energy conversion devices, sensors, field emission displays and radiation sources, semiconductor devices, probes, and interconnects (Baughman, Zakhidov and Walt de Heer, 2002). CNTs are especially considered as good electron emitting sources for the field emission displays due to their high geometrical aspect ratio, electrical conductivity, and mechanical strength (Dohyung Kim, Jean-Eric Bourree, and Sang Youl Kim, 2009).

At present, the control of the growth of CNTs and their selective positioning is very important for developing devices based on CNTs. In particular vertical alignment is essential to achieve a high geometrical enhancement factor in field emitters (Do-Hyung Kim, Dong-Soo Cho, Hoon-Sik Jang, Chang-Duk Kim, and Hyeong-Rag Lee, 2003).

Vertically aligned CNT-arrays can be grown on a moving substrate, demonstrating continuous growth of nanoscale materials with long-range order (Guzman de Villoria, Figueiredo, Hart, Steiner, Slocum and Wardle, 2009). According to the text, a cold-wall chamber with an oscillating moving platform was used to locally heat a silicon growth substrate coated with an Fe/Al<sub>2</sub>O<sub>3</sub> catalyst film for CNT growth via chemical vapor deposition (CVD).

In 2010, Shang *et al* (Shang, Tan, Stolojan, Papakonstantinou and Silva, 2010) reported the low-temperature growth of vertically aligned CNTs at high growth rates by a photo-thermal chemical vapour deposition (PTCVD) technique using a Ti/Fe bilayer film as the catalyst. It is said in the article that the bulk growth temperature of the substrate was as low as 370 °C and the growth rate was up to 1.3  $\mu\text{m}/\text{min}$ , at least eight times faster than the values reported by traditional thermal CVD methods.

We assume that the growth of vertically aligned CNTs can be implemented by using porous silicon as a substrate. In this case CNTs will grow in pores and align. Furthermore, if we can find process conditions we will grow free-standing single CNTs.

In our researches we use the commercially pure iron as a catalyst. In order to fill the pores by the catalyst we have to use the liquids. In this paper we report the results of our researches on the application of the liquid ferriferous salts solutions as sources of iron (catalyst).

Fig. 1 shows a schematic diagram of installation for performing CVD-processes that we use in our experiments.

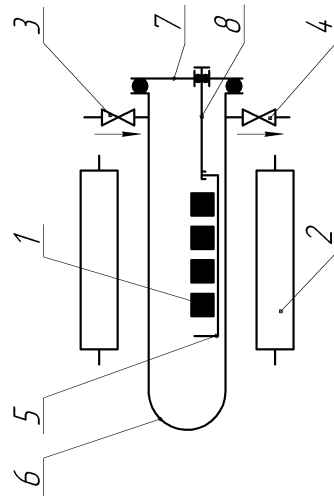


Fig. 1. Schematic diagram of installation for performing CVD-processes: 1 – substrates with thin film of catalyst, 2 – heater, 3 – gas system, 4 – pump, 5 – boat for samples, 6 – reactor (vacuum chamber), 7 – vacuum lock, 8 – tie.

CVD-method consists in the following (Дьячков, 2006): vapors of the hydrocarbons are skipped in the flow of gas-carrier above a thin film of catalyst at temperature range of 650 – 1000 °C. Heating is necessary because the layer of catalysts must be restructured and activated and reactive gases must be dissociated and reacted with catalysis (Фурсиков, Тапаков, 2004). In our experiments we usually use epitaxial silicon wafers as a substrates (as well polycor can be used), vapor of heptane as a source of carbon and

In our experiments we usually use epitaxial silicon wafers as a substrates (as well polycor can be used), vapor of heptane as a source of carbon and

argon as a gas-carrier. In our laboratory CVD-processes are performed at temperatures above 750 °C.

This study was carried out with using solutions of iron salts as a sources of catalyst. We used solutions of the ferritin and ferrous acetate in the distilled water and ethanol (0.02 %).

Solutions were deposited on the substrates by conventional drop method. Presence of CNTs was confirmed by using scanning electron microscopy (MRSEM-100M).

## Results and discussion

As noted above, obtained samples were studied on the scanning electron microscope. Fig. 2(a)-(d) clearly show that on the all surfaces of substrates CNT films were grown.

As shown in Fig. 2(a), in case of solution of ferrous acetate in distilled water CNTs grown very matted. CNT-film on the surface was non-uniform that was determined by low wettability of the substrate.

As we can see, most thin CNTs were obtained on the substrates coated by the solution of ferrous acetate in ethanol (see Fig. 2(b)). In this case good wettability of the substrate was observed. Density of the CNT packing is low indicating that the solution of salt flowed uniformly and that the thin film of

In Fig. 2(c) we can see “forest” of thin CNTs. In this case bad wettability of the substrate was observed and CNT-film on the surface was non-uniform.

## Conclusions

In conclusion, CNTs were grown on silicon substrates by CVD-method at high temperature (above 750 °C) using ferriferous salts solutions as sources of iron (catalyst). We used solutions of the ferritin and ferrous acetate in the distilled water and ethanol (0.02%). Solutions were deposited on the substrates by conventional drop method.

## Acknowledgments

This study was supported by the laboratory of micro and nanoelectronics (Saratov Branch of the Kotelnikov Institute of Radio Engineering and Electronic of Russian academy of sciences). E.A. Tarasov would like to thank Z.I. Buyanova for all her assistance and discussions regarding fabrication of CNTs.

- The growth of freestanding single carbon nanotube arrays // Nanotechnology. 2003. Vol. 14, №12. P. 1269 – 1271.
5. N G Shang, Y Y Tan, V Stolojan, P Papakonstantinou and S R P Shka. High-rate low-temperature growth of vertically aligned carbon nanotubes // Nanotechnology. 2010. Vol. 21, №50. P. 1 – 6.
  6. Ray H. Baughman, Anvar A. Zakhidov and Walt A. de Heer. Carbon Nanotubes-the Route Toward Applications // Science. 2002. Vol. 297, №5582. P. 787 – 792.
  7. R Grizman de Villoria, S L Figueiredo, A J Hart, S A Steiner III, A H Slocum and B L Wardle. High-yield growth of vertically aligned carbon nanotubes on a continuously moving substrate // Nanotechnology. 2009. Vol. 20, №40. P. 1 – 8.

## TECHNOLOGICAL SYSTEM OF MODELING OIL AND GAS BASINS

**E.V. Vorobieva**

Saratov State University

Basin modeling, hydrocarbons, Temis software, simulating parameters, exploration and prospecting oil and gas

### Introduction

Basin modeling is the essential tool applied to a group of geological methods and geological information that can be used to analyze the formation and evolution of sedimentary basins. Nowadays it is often used to check evaluation of potential hydrocarbon reserves. Software packages have been designed for 1D, 2D, 3D basin modeling purposes to simulate the burial and thermal history of a basin as well as petroleum migration modeling. They offer us faster and more reliable results for increasing scientific and business potential of exploration and prospecting oil and gas fields.

The main purpose of this software is to reconstruct the history of a sedimentary basin and to simulate the main processes leading to petroleum occurrence and entrapment, such as: hydrodynamics, thermal transfer, hydrocarbon generation, expulsion and migration.

The petroleum industry now ranks basin modeling as the top leadership technology that increases exploration success and lowers finding costs. Over the last two decades, 2D and 3D imaging and modeling of the subsurface through time have co-evolved and emerged as a major research focus of the petroleum industry (Галушкин, 2007). So currency and importance of modeling in geology don't give rise to doubt.

In this article I would like to examine the technological system of modeling basins on Temis software example, give geological explanation of every module in this program and mention some problems which are connected with modeling usage.

### REFERENCES

1. Дьяконов П.Н. Углеродные нанотрубки: строение, свойства, применения. М.: БИННОМ, 2006.– 248 с.
2. Фурсиков П.В., Тарасов Б.П. Каталитический синтез и свойства углеродных нановолокон и нанотрубок. Международный научный журнал «Альтернативная энергетика и экология». 2004, №10(18). С. 5 – 21.
3. Dohyung Kim, Jean-Eric Bourree, and Sang Youl Kim. Calculation of the field enhancement for a nanotube array and its emission properties // Journal Of Applied Physics. 105, 084315 (2009). 5 pages.
4. Do-Hyung Kim, Dong-Soo Cho, Hoon-Sik Jang, Chang-Duk Kim, and Hyewong-Rag Lee.

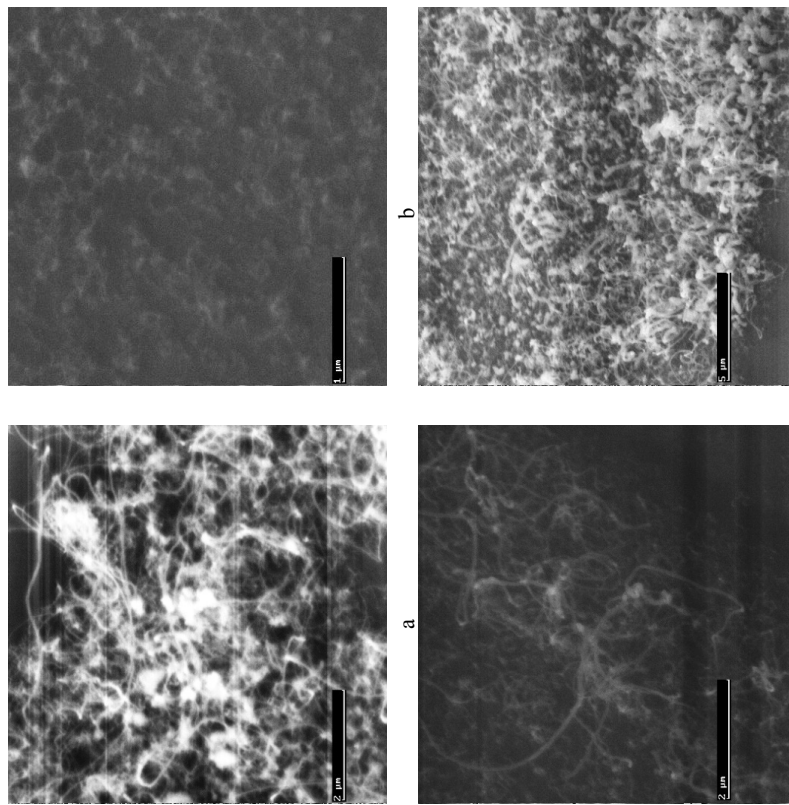


Fig. 2. Surfaces of the CNT “forests” grown by using the ferrous salts solutions:  
a – solution of ferrous acetate in distilled water, b – solution of ferrous acetate in ethanol,  
c – solution of ferritin in distilled water, d – solution of ferritin in ethanol.

## The main idea and methodology of basin modeling

There are different kinds of modeling. Usually all versions (1D, 2D, 3D) are integrated in one program for convenience. It is very useful because they work with different geological information (wells, sections and maps) and are used for different purposes. It allows us to have complex and reliable results. In this article 2D and 3D will be examined more detailed. 1D basin modeling is very helpful for some targets but it is also the easiest one. So it is usually used as subsidiary tool.

The program simulates the physical and geochemical processes leading to hydrocarbon generation, migration and entrapment. The simulation is performed on geological section or map characterized by a geometric evolution, stratigraphy and lithological infilling. The grid formed in the program is a set of cells. The upper and lower limit of each cell is corresponded to isochrones. The lateral limits of the cells are vertical lines. The geological mesh, resulting from gridding detailed present-day geological information, is progressively reconstructed during the forward simulation. The genetic information contained in the cells describes geological event in terms of age and type. This geological event can be the deposition of a certain amount of sediments of a given lithology. Such an event will lead to the creation of a cell filled with sediments. It can also be erosion or a hiatus. You can simulate the basin history without providing any more data than is initially contained in the geological mesh. Such a simulation will at least allow you to visualize the geometric evolution of the geological mesh through time. This simulation will be very simple. This is the first step of creating huge useful model with various geological information databases.

At its most basic, a basin modeling exercise must contain the burial history of the basin (usually called back-stripping), the thermal and hydrodynamic history of the basin, the maturity history of the source rocks and also the expulsion, migration and trapping of hydrocarbons (Fig 1).

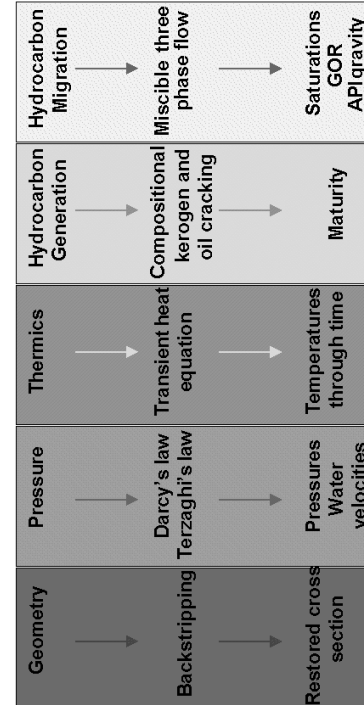


Fig. 1 Common processes in basin modeling

These models are based on four principal issues:

1. The geometric evolution of the basin shape, as a result of sedimentation, compaction, erosion and faulting.
2. The thermal evolution of sediments, resulting from crustal heat flow distribution and sedimentary heat transfer processes.
3. The evolution of fluid pressures and fluid flow, due to both compaction and regional hydrodynamics.
4. The generation and migration of hydrocarbons from source rocks to traps.

Module system of basin modeling on Temis 2D software example  
Technological system will be examined on Temis 2D example because of its simplicity. It doesn't differ much from other versions although it has some distinctive features.

On figure 2 Temis 2D interface is presented.

Its purpose is to provide the user with all the necessary information about the program and the physical and geological concepts that are embodied in it. It allows creating a 2D model, defining the boundary conditions and the simulation parameters.

The main window consists of a list describing the structure of a data set. This main window is the only Temis window that is continuously opened during a session. It is organized into two sections: a section menu (contains all the editors that allow the definition of data used to define the sections) and a simulation parameters menu (contains all the editors that allow the definition of the simulation options).

In the first part of this section you put the most important data for modeling such as geometry and properties, eustatism, lithology, fault zones and water. As the first module was mentioned earlier, the main attention will be paid to other modules.

- Eustatism allows you to edit sea level variations through time relative to the present day sea level. Sometimes it is not used because of the lack of information about the sea level on studied territory in different periods of geological time.
- The Lithology editor allows you to load and edit different kinds of rocks and the parameters describing their physical and chemical behavior.
- The faults zones hydraulics histories editor allows creating, deleting and managing the fault areas defining their hydrodynamic characteristics. A fault area is a lithology independent entity defined by a name, a color and history of three parameters: vertical permeability, horizontal permeability and capillary pressure. The hydraulic history is a collection of time intervals during which the fault area is active or inactive. When the fault is active, in each cell of the mesh belonging to a fault area, the above mentioned properties are described by the fault area history rather than by the lithology contained in the cells.

- The water editor allows defining the physical properties of water. These properties are used when simulation involves fluid flow.

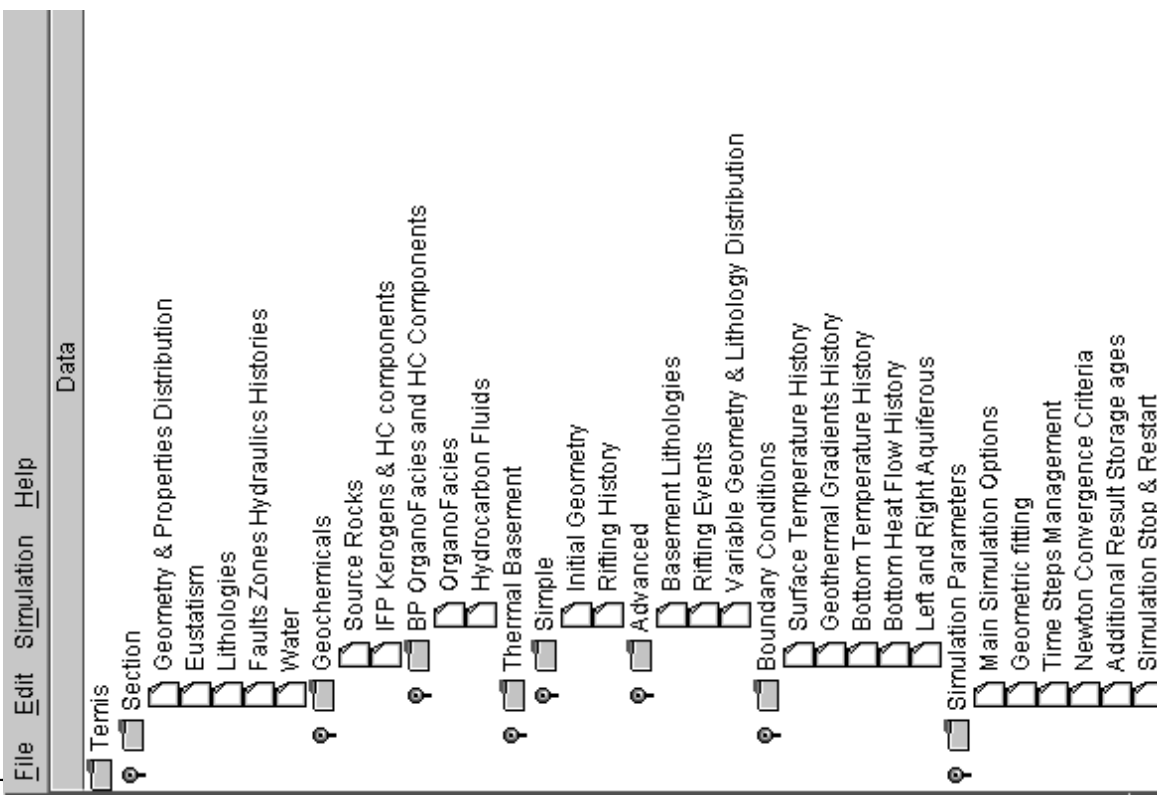


Fig. 2 Temis 2D interface

- The next group of modules is connected with geochemistry. These parameters are very important in petroleum geology. Basin modeling is rapidly growing as a tool for better understanding subsurface migration, accumulation, and preservation of hydrocarbons. This approach is also used as a tool for predicting active source rock, thermal maturity of the source rock, migration pathways, and the timing of petroleum generation.

The Source rocks list editor allows creating and managing source rocks. They are defined by name, color, kerogen and richness. Types of kerogen are classified by IFP (Institute Francais du Petrole). The IFP Kerogens and HC components module allows you to describe kerogens according to one or several hydrocarbon schemes whose complexity is defined by the number of their chemical components. The geochemical principles describing the behavior of these kerogens are embodied in program. There is a problem with these types because Russian scientists use another classification of kerogen and it is very difficult to correlate data with French classification. Another problem here is a lack of data regarding source-rock maturity.

Kerogen is formed during sediment diagenesis and is progressively thermally cracked to petroleum fluids during sediment burial. Kerogen degradation rates, amount and chemical composition of the generated products are modeled in Temis 2D. The prediction of trapped petroleum volumes, their detailed compositions, and effects of secondary processes are also modeled which is really useful for petroleum production (Taryushkin, 2007; Xaht, 1982).

Another important part of modeling is thermal evolution of sediments.

The earth is a gigantic heat engine. A tremendous amount of heat is constantly transported from its center to the surface by thermal convection and conduction. The geothermal heat is ultimately the driving force of most large-scale geologic processes that take place on the surface of the earth (e.g., movement of tectonic plates, volcanic eruption, etc.). A portion of the heat conducted through the earth's crust is used to drive the chemical reactions which transform the organic matter contained in sedimentary rocks into petroleum. Without the geothermal heat, there would be no naturally occurring petroleum on this planet. Therefore, measuring this heat and understanding its transport mechanisms through the crustal rocks are essential to the science of petroleum exploration (Nagihara, 2002).

Most of the used concepts are difficult to calibrate (e.g. basement lithology or rifting) generally because of the shortage of information or they are poorly studied.

The boundary conditions editors allow you to create and manage the thermal and hydraulic boundary conditions of the model.

It includes the five following editors:

- Surface temperature history (surface temperatures are defined as temperature profile along the section)

- Geothermal gradient history (geothermal gradients are defined as a profile along the section, when geothermal gradient option is used, the thermal basement is not involved in the thermal computation: the temperature is computed only in the sedimentary layers but not in the basement.)
  - Bottom temperature history (using temperature as the thermal boundary condition at the bottom of the lithosphere)
  - Bottom heat flow history (bottom heat flow is the amount of heat entering the basement.)
  - Left and right aquiferous (gathers in one manager the definition of the water head history and the temperature history)
- Simulation parameters are very important in basin modeling. They are set for the type of simulation to be performed. They are grouped around six editors:

- Main simulation options (compaction and hydraulics, thermics)
- Geometric fitting (true geometry or thickness correction can be used)
- Time steps management (time step limits)
- Newton convergence criteria (Newton scheme for controlling the accuracy of pressure, porosity, volume and saturation calculation)
- Additional result storage ages (allows you to add intermediate ages between the already existing ones)
- Simulation stop and restart (choose to start the simulation either at the beginning of the section history, i.e. at the age of its oldest marker or from an intermediate stage by using intermediate results from a previous simulation)

## Conclusion

Basin modeling plays an important role in modern petroleum exploration because it integrates practically all geological principles (**Бычко, Пырьевич**, 1994). Basin models are deterministic, and therefore, modeling results are unique. However, exploration scenarios are uncertain, and therefore, modeling results should be expressed in a probabilistic manner (Wendebourg, 2004). One of the most important problems with basin modeling is lowering risks in geological prospecting. This is difficult to achieve with basin models because they require a multitude of input parameters, some of which are little or not at all known. Identify the ones that actually influence the oil production process, and make safe production forecasts are the main purposes.

As petroleum becomes more difficult to find and reserves become more difficult to replace, petroleum systems modeling has grown because it better quantifies the generation, migration, and entrapment of the remaining resource. Thanks to growing computational facilities, reservoir modeling is getting more and more complex. It also facilitates the interpretation of the stratigraphic and sedimentologic processes that are important to develop a predictive sequence stratigraphic framework.

- Geothermal gradient history (geothermal gradients are defined as a profile along the section, when geothermal gradient option is used, the thermal basement is not involved in the thermal computation: the temperature is computed only in the sedimentary layers but not in the basement.)
  - Bottom temperature history (using temperature as the thermal boundary condition at the bottom of the lithosphere)
  - Bottom heat flow history (bottom heat flow is the amount of heat entering the basement.)
  - Left and right aquiferous (gathers in one manager the definition of the water head history and the temperature history)
- Simulation parameters are very important in basin modeling. They are set for the type of simulation to be performed. They are grouped around six editors:

- Geothermal gradient history (geothermal gradients are defined as a profile along the section, when geothermal gradient option is used, the thermal basement is not involved in the thermal computation: the temperature is computed only in the sedimentary layers but not in the basement.)
  - Bottom temperature history (using temperature as the thermal boundary condition at the bottom of the lithosphere)
  - Bottom heat flow history (bottom heat flow is the amount of heat entering the basement.)
  - Left and right aquiferous (gathers in one manager the definition of the water head history and the temperature history)
- Simulation parameters are very important in basin modeling. They are set for the type of simulation to be performed. They are grouped around six editors:

## Acknowledgements

The author wish above all to thank Postnova E. for patience and support. And I also appreciate the helpful suggestions and comments by all members of geology and oil-and-gas content division in NVNIGG. Their help had a great influence on the article and I am very grateful to them.

## REFERENCES

1. Бурдук Д.ж., Родникович Д.ж. // Моделирование бассейна и разведка нефти и газа // Геология нефти и газа. 1994. №1
2. Хант Д.ж. Геохимия и геология нефти и газа. М. : Мир, 1982
3. Гапукин Ю. И. Моделирование осадочных бассейнов и оценка их нефтегазоносности; М. : Научный мир, 2007
4. Naghara S., Brooks J. M., Bernard B. Application of marine heat flow data // Oil and gas journal. 2002. July
5. Wendebourg J. Uncertainty of petroleum generation using methods of experimental design and response surface modeling: application to the Gippsland Basin, Australia // AAPG / Datapages discovery series. 2004. № 7. P. 295–307.

## DYNAMIC LOADING OF HYDRO MANIPULATOR EFFECT ON ITS LONG-TERM STRENGTH

**Zhigunov**

*Институт?*

The major task of agriculture is to satisfy the needs of the population in high-quality food and providing raw materials for various sectors of reprocessing industry.

One of the important stages of almost any manufacture is loading of made production for its further transportation, and this is done with the help of load-lifting machines of various type.

Using different capture devices on the base of one load-lifting unit substantially reduces the cost of mobile technology, which is important not only in small farms and businesses.

As the object of our research we consider the hydraulic manipulator with exchangeable working unit (fig. 1)

There is a large number of outrigger hydromanipulators different both in design and complexity produced nowadays.

In connection with the specific character of this sort of technique special demands are made for its reliability.



Fig. 1. Hydromanipulator

From among the problems associated with the solution of this problem, first of all, it is necessary to mention those associated with getting actual and reliable information about operational capability of construction elements of boom hydro manipulators.

Dynamic loadings in this case arise during the periods of unsteady movement, for example, at the moments of sharp lifting of loads or instant braking of cargo and in a number of other cases, and have a casual character.

However, in order to obtain necessary information actual tests are required using fairly complex and expensive measurement systems as well as the measurement results processing.

The best solution in this case is imitation (computer) simulation. To study the dynamic loadings of hydraulic manipulator in different work conditions its computer simulation model has been accomplished (fig. 2). The model has been simulated in Ansys system, which allows us to create models of parts and assembly units, and also carry out research, tests and optimization of the models.

Structures under static have been analyzed on the basis of this model. Dynamic loading has revealed dangerous cross and boom arm. Zones of the greatest internal stress are shown in Fig. 2.

This technique allows us to estimate solid construction with dynamic loads and determine the place of the greatest internal tensions and, accordingly, to place labels for full-scale tests.

A numerical experiment simulating variable loading (with decaying character) under different loading-unloading operations cycle (idle moving arrows, lowering the grapple for cargo hoisting, uplifting and moving booms with the cargo unloading) has been carried out.

It has been found that the buffering boom of the hydro-cylinder reduces the maximum dynamic loadings and the number of cycles of repeatedly-variable loadings, as frequency of loadings in a unit decreases the affects of the fatigue of the steel truck, and hence its long-term strength.

With such a conclusion, it would be most interesting to test the results of the experiment reducing these parameters with special dampers.

#### REFERENCES

1. Карпов Ю. Г. Имитационное моделирование систем. Введение в моделирование с AnyLogic 5. СПб : БХВ-Петербург, 2005.
2. Шеленков А. Н. Использование 3D моделирования для расчёта гидроманипуляторов / А. Н. Шеленков, П. Г. Колесников. Журнал «Современные наукоёмкие технологии», № 3, М., 2010, С. 56–57.
3. Кратинков А. Н. Математическое моделирование динамических характеристик погрузчиков-манипуляторов : дис. канд. техн. наук. Саратов, 2003.



Fig. 2. A breakdown of the model manipulator on finite elements and strength analysis of constructions

#### STUDYING THE NATURE OF CONTACT CORROSION LAYERS ON LEAD ALLOYS BY IMPEDANCE SPECTROSCOPY

I. V. Zotova, S. E. Tulanov

Saratov State University

Corrosion layers on lead alloys were studied by means of impedance spectroscopy, scanning electron microscopy, and X-ray analysis. The films were formed under several potentials and polarization conditions in a 4.8

$\text{M H}_2\text{SO}_4$  solution. Parameters of the equivalent circuits proposed were estimated.

Up to now, lead-acid batteries are still widely used due to their high performance/price ratio, safety and reliability [1]. The shift to maintenance free batteries has resulted in the search for non-antimoniul grid compositions in lead acid batteries. The initial approach to solve this problem has been to use pure lead anodes or lead calcium binaries. The lead-calcium grid has good maintenance-free performance but has a short deep-discharge cycle life. In the deep-discharge process, a  $\text{PbSO}_4/\alpha\text{-PbO}$  film with high resistivity grows more easily on the positive grid alloys, seriously shortening the cycle life [2]. One of the most effective methods is to add tin into the lead alloy to improve the conductivity of the anodic film. The addition of tin can improve the physical and chemical properties of a Pb-Ca alloy, typically reducing the thickness of the PbO passive film, and improving the conductive properties of the passive layer [3].

The objective of the present study is to present a comparative study of the properties of contact corrosion layers on lead alloys by means of impedance spectroscopy, scanning electron microscopy, and X-ray analysis.

The investigation was performed on pure lead, Pb – 0.1 wt. % Sn and Pb – 0.1 wt.% Sn – 0.08 wt.% Ca alloys. A lead alloys were used as working electrodes. The working-electrode surface was polished mechanically with emery paper of successively decreasing grain size down to about 10 mm. The working electrodes were, then, washed with distilled water before immersing in to the electrolyte. Before every experiment, cathodic polarization at a potential of -1.2 V for 20 min was performed in order to remove any oxidation products formed by aerial oxidation during preliminary treatment. The electrolyte was 5  $\text{M H}_2\text{SO}_4$  solution. A platinum plate served as a counter electrode. An Ag/KCl electrode was used as the reference electrode. All potentials reported here are referred to this electrode.

On Fig. 1, Nyquist plots are resulted for the investigated samples. It is visible that the greatest value of the general impedance is observed at electrodes from lead. The corrosion film formed at this potential can be characterized as double system Pb/PbO/PbSO<sub>4</sub>. Presence of phases PbO and PbSO<sub>4</sub> has been confirmed by the X-ray analysis. The addition of tin in lead alloys leads to reduction of the general impedance of system that is connected with transformation of PbO to  $\text{PbO}_x$  ( $1 < x < 2$ ), having higher conductivity. The received frequency dependence is most precisely approximated by the equivalent electric scheme consisting of capacity C, connected in parallel with resistance R1 and block CPE-R1 and is consecutive with resistance R<sub>S</sub>, which corresponds to ohmic resistance of electrolyte (Fig. 2).

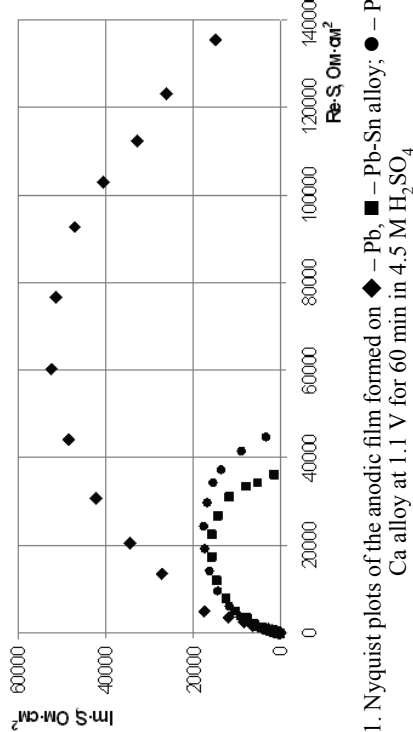


Fig. 1. Nyquist plots of the anodic film formed on  $\blacklozenge$  – Pb, ■ – Pb-Sn alloy; ● – Pb-Sn-Ca alloy at 1.1 V for 60 min in 4.5 M  $\text{H}_2\text{SO}_4$

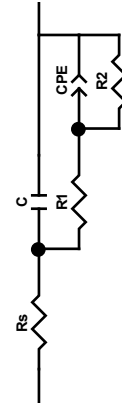


Fig. 2. Equivalent circuit of the electrochemical impedance spectroscopy

The calculated parameters of this scheme are resulted in Table 1. Elements R<sub>1</sub> u R<sub>2</sub> can be carried to external and internal parts of a corrosion layer, consisting at the given potential from sulfate of lead  $\text{PbSO}_4$  and lead oxide  $\text{PbO}$  ( $\text{PbO}_x$ ), accordingly. The capacity C describes a double electric layer on border a surface of a corrosion layer / electrolyte. Nature CPE (an element with a constant corner of shift of phases) is connected with non-uniform distribution of a current on a surface lead oxide in thickness of a corrosion layer.

Table 1  
Fit parameters for a Pb, Pb – Sn and Pb – Sn – Ca electrodes at polarization time 60 min at 1.1 V in 5 M  $\text{H}_2\text{SO}_4$

Circuit element	t, min	Pb	Pb-Sn	Pb-Sn-Ca
$R_S, \Omega \cdot \text{cm}^2$	0.73	0.63	0.54	
$C, \text{F}$	$2.28 \cdot 10^{-6}$	$2.96 \cdot 10^{-6}$	$8.96 \cdot 10^{-6}$	
$R_1, \Omega \cdot \text{cm}^2$	12.80	9.14	10.40	
$CPE$	$Y, \Omega^{-1} \cdot \text{cm}^{-2} \cdot \text{s}^\alpha$	$0.74 \cdot 10^{-5}$	$1.10 \cdot 10^{-5}$	$1.32 \cdot 10^{-5}$
	$\alpha$	0.78	0.80	0.80
	$R_2, \Omega \cdot \text{cm}^2$	133020.00	38962.00	45004.00

For the analysis of the calculated data it is possible to draw a conclusion what exactly the alloying tin promotes formation more a conductor lead oxide. Calcium as active metal can lead to an alkalinization of the near-electrode layer and to promote the formation of  $\text{PbO}$ , than it is possible to explain small deterioration of conductivity of a corrosion layer on the alloy  $\text{Pb-Sn-Ca}$ , in comparison by the alloy  $\text{Pb-Sn}$ .

In electronic microphotos (Fig. 3) for lead it is possible to observe a dense film with crystals homogeneous by both the size and structure, and that time as for the  $\text{Pb-Sn}$  alloy, the main part of the film is microcrystalline, with large grains, and it is characterized by the presence of cracks and pores that can lead to simplification of the process of lead monoxide oxidation to higher oxidation states. In the  $\text{Pb-Sn-Ca}$  alloys, the formed film again finds a large-grained structure of sulfate, but more friable and with the same porosity. The aforesaid can create small difficulties for the  $\text{PbO}_x$  formation.

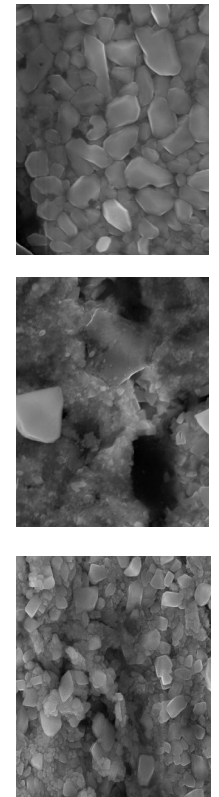


Fig. 3. Scanning electron micrographs of pure Pb (a),  $\text{Pb-Sn}$  (b) and  $\text{Pb-Sn-Ca}$  alloys. The corrosion layer was formed at 1.1 V for 6 h in 5 M  $\text{H}_2\text{SO}_4$ . Magnification –  $5 \cdot 10^5$

#### REFERENCES:

1. Li A., Chen Y., Chen H., Shu D., Li W., Wang H., Dou C., Zhang W., Chen S. Electrochemical behavior and application of lead-lanthanum alloys for positive grids of lead-acid batteries // J. Power Sources. 2009. Vol. 189. P. 1204–1211.
2. Slavkov D., Haron B. S., Popov B. N. Effect of Sn and Ca doping on the corrosion of Pb anodes in lead acid batteries // J. Power Sources. 2002. Vol. 112. P. 199–208.
3. Sherveldani R. K., Isfahani A. Z., Khodaviv R., Hafez-Mehriadi A. Electrochemical investigation of the anodic corrosion of  $\text{Pb-Ca-Sn-Li}$  grid alloy in  $\text{H}_2\text{SO}_4$  solution // J. Power Sources. 2007. Vol. 164. P. 890–895.

## OPTICAL CLEARING OF EYE TISSUES

*E. A. Zubkina, E. A. Genina, A. N. Bashkatov*

*Saratov State University*

#### Introduction

Optical diagnostic techniques are perspective in such fields of ophthalmology as transscleral eye surgery, development of noninvasive methods of optical eye tomography, indication of tissue fluid homeostasis (Tuchin et al., 1997). For example transscleral photocoagulation of eye bulb tissues, ciliary body, retina etc. is widely applicable for treatment of glaucoma, retinal detachment, and several other diseases (Bakutkin, Shubochkin, 1991; Nemati et al., 1996; Nemati et al., 1998). However, because of the multiple light scatterings by connective (fibrous) eye tissues, a sufficient limitation of laser beam penetration depth and focusing precision is occurred during the operation on retina.

It is known that basic reason of light scattering in conjunctiva and sclera as well as other fibrous tissues is refractive index mismatching between interstitial fluid and connective tissue structural elements (collagen and elastic fibers) (Tuchin, 2007; Genina et al., 2010). Administration of immersion liquid with refractive index higher than interstitial fluid refractive index in tissue causes partial substitution of interstitial fluid by immersion solution, refractive indices matching of tissue scatterers and their environment and, therefore, sufficient decrease of scattering. Besides, immersion liquids can induce local dehydration of tissue due to their osmotic properties that also results in matching of refractive indices of different tissue components (Liu et al., 1996).

Information about diffusion coefficients is required for creation of appropriate mathematical model describing processes of interaction of osmotic fluids with tissues. Although the diffusion of many biocompatible liquids in water solutions is well described (Bretschneider, 1966; Rid et al., 1982; Kotyuk A., Yanachek K., 1980), their diffusion in tissues is investigated not enough. In this work we have performed the estimation of diffusion coefficient of glucose solution in both rabbit eye conjunctiva and sclera in vitro on the basis of experimental researches of the change of their optical properties under the action of 40%-aqueous glucose solution.

#### Materials and methods

For this study in tens samples of rabbit eye sclera and conjunctiva in vitro were used. The samples were obtained from autopsy and kept in saline at temperature 4–5°C during 24 hours until spectroscopic measurements. Connective tissues were removed from each sample before measurements were started. Sample's thickness was measured by micrometer to within 50  $\mu\text{m}$ .

As an immersion agent commercially available 40%-aqueous solution of glucose was used. Refractive index of the solution was 1.391. It was measured using Abbe refractometer at wavelength 589 nm.

Investigations were performed with experimental setup containing the light source – halogen lamp HL-2000, fibers delivering light to the tissue sample and collecting light passed through the sample, cuvette with the sample, spectrometer – USB-4000 (Ocean Optics, USA) and PC. Scheme of experimental setup is presented in the fig. 1.

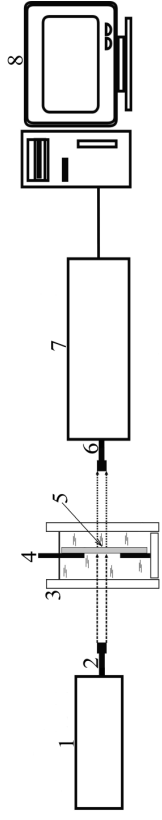


Fig. 1. Scheme of experimental setup: 1 – light source – halogen lamp HL-2000; 2 – fiber delivering light to the tissue sample; 3 – cuvette with immersion liquid; 4 – frame for tissue sample attaching; 5 – the tissue sample; 6 – fiber collecting light passed through the sample; 7 – multichannel spectrometer; 8 – PC.

Tissue samples were fixed on the frame with a hole 7×7 mm<sup>2</sup> for collimated transmittance measurement, and then they were placed in the cuvette between two optic fibers P400-1-UV-VIS (Ocean Optics, USA) with inner diameter 400 μm. One fiber was used for light delivery to the sample and another – for collecting light passed in forward direction. Collimators 74-ACR (Ocean Optics, USA) were fixed on the fiber's ends with standard connectors SMA-905 (Ocean Optics, USA) for collimated bundle ensuring.

The dynamics of the change of collimated transmittance of tissue samples was registered by once-a-minute consecutive recording of collimated transmittance spectra in the range of 500-900 nm for 30-60 minutes for conjunctiva and for 40-65 minutes for sclera since the moment of the placement of tissue sample in the glucose solution. The signal received from the cuvette with 40%-aqueous glucose solution and the frame was used as a reference signal. All measurements were performed at room temperature (about 20°C).

In the investigation we supposed that the change of sample interstitial fluid refractive index is consequence of immersion liquid diffusion in tissue and osmotic water outflow from tissue. It results in tissue scattering coefficient decrease. The exploration of dynamics of this process allows estimating the diffusion coefficient as a measure of average speed of exchange flow of osmotic fluid in tissue and water from tissue.

Free diffusion model (Bashkatov et al., 2003) was used for the quantitative description of the process of glucose penetration in eye tissues. We assumed that the following approximations were valid for the transport process:

- 1) only concentration diffusion took place, i.e., the exchange flux of osmotically active solution into the tissue and water from the tissue at a certain point within the tissue sample was proportional to the osmotically active substance concentration at this point;
- 2) the diffusion coefficient was constant over the

entire sample volume. Geometrically the tissue sample was presented as a plane-parallel slab with a finite thickness. Since the square of superior and inferior surfaces of such plate is much more than the square of its lateral surfaces we can neglect by edge effects and solve one-dimensional problem of diffusion. So, problem statement can be expressed as

$$\frac{\partial C(x,t)}{\partial t} = D \frac{\partial^2 C(x,t)}{\partial x^2}, \quad (1)$$

where  $C(x,t)$  is the glucose concentration in tissue, g/ml;  $D$  is the diffusion coefficient, cm<sup>2</sup>/sec;  $t$  is the time period of diffusion process, sec; and  $x$  is the spatial value of tissue sample thickness, cm.

Since the volume of glucose solution ( $\approx 3000$  mm<sup>3</sup>) significantly exceeded the volume of the tissue sample ( $\gg 50$  mm<sup>3</sup>) in the experiments, so corresponding boundary conditions can be write in the form:

$$C(0,t) = C(d,t) = C_0, \quad (2)$$

where  $C_0$  is the glucose concentration in the solution;  $d$  is the tissue sample thickness, cm.

Initial condition indicates the fact of glucose absence in all internal points of conjunctiva and sclera sample before its incubation in the solution:

$$C(x,0) = 0, \quad (3)$$

The solution of diffusion equation (1) subject to the boundary (2) and initial (3) conditions has the form:

$$C(x,t) = C_0 \left( 1 - \sum_{i=0}^{\infty} \frac{4}{\pi(2i+1)} \sin \left( \frac{(2i+1)^2 D \pi x}{d} \right) \exp \left( -\frac{(2i+1)^2 D \pi^2 t}{d^2} \right) \right). \quad (4)$$

Scattering coefficient of conjunctiva and sclera  $\mu_s$  can be described with the expression [1]:

$$\mu_s(t) = N \sigma_s(t) = N \frac{\pi^2 \alpha x^3}{8} (m^2 - 1)^2 \left( 1 + \frac{2}{(m^2 + 1)^2} \right), \quad (6)$$

where  $N$  is the number of scatterers in unit volume,  $\sigma_s$  is the scattering cross-section,  $x = 2\pi n m_l / \lambda$  is the diffraction parameter,  $m = n_c / n_l$  is the relative refraction index of scatterers,  $\square$  is the refraction index of collagen fibers (Bashkatov et al., 2000), and  $\square$  is the scatterer's radius.

Time dependence of collimated transmittance coefficient of conjunctiva and sclera sample, placed into glucose solution has the form:

$$T_c(t) \cong \exp(-(\mu_a + \mu_s(t))d), \quad (7)$$

where  $T_c(t)$  is the collimated transmittance;  $\mu_a$  is the absorption coefficient.

Since average absorption coefficient of eye tissues is significantly less than scattering coefficient (Bashkatov et al., 2010) in the investigated spectral range, we can neglect absorption coefficient.

Equations (4)-(7) define the collimated transmittance dependence on glucose solution concentration in conjunctiva and sclera samples, i.e. form the direct problem. In this case inverse problem is recovery of diffusion coefficient value with using of the time-dependent transmittance. This problem was solved by minimization of the target function:

$$f(D) = \sum_{i=1}^{N_t} (T_c(D, t_i) - T_c^*(t_i))^2, \quad (8)$$

where  $N_t$  is the total amount of experimental points obtained in the course of registration of the time-dependent collimated transmittance;  $T_c(D_i)$  is the theoretical value of transmittance in the time point  $t_i$  and with the setting value of  $D$ ;  $T_c^*(t_i)$  is the experimental value of transmittance in the time point  $t_i$ .

To minimize the target function (8) the «complex» method (Bandi, 1988) was used. Iteration procedure repeated until experimental and calculated data were matched. As a termination condition of the iteration process, we used the

$$\text{following expression: } \frac{1}{N_t} \sum_{i=1}^{N_t} \left| \frac{T_c(D, t_i) - T_c^*(t_i)}{T_c^*(t_i)} \right|^2 \leq 0.01.$$

## Results and discussion

In the results of the experiments we have measured time dependence of collimated transmittance and scattering coefficient for each sample of rabbit eye conjunctiva and sclera sample under action of 40%-aqueous glucose solution in the spectral range 500-900 nm (fig. 2-5).

On the experimental curves we can see that at the initial time conjunctiva and sclera are almost opaque mediums for both VIS and NIR ranges. Substitution of interstitial fluid for glucose solution causes scattering coefficient decrease and, therefore, collimated transmittance increase. Figures 2-5 show that optical clearing of conjunctiva and sclera samples takes place in all vision range with predominance in red spectral region.

From analysis of experimental data we determined that average increasing of the collimated transmittance of radiation passed through the rabbit eye conjunctiva and sclera is  $1.98 \pm 0.087$  folds and  $19.7 \pm 17.2$  folds, respectively. The scattering coefficient of this radiation decreased in about  $0.88 \pm 0.08$  folds and  $0.61 \pm 0.18$  folds, respectively.

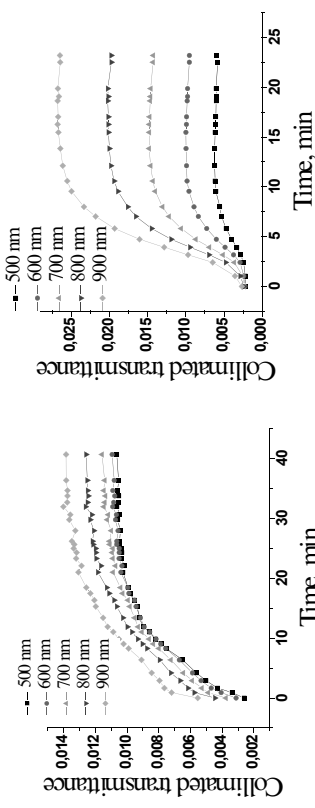


Fig.2. The time-dependent transmittance of rabbit eye conjunctiva under the action of 40%-aqueous glucose solution

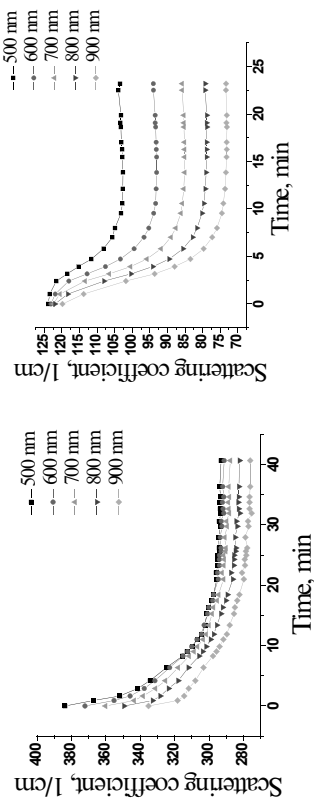


Fig.3. The time-dependent transmittance of rabbit eye sclera under the action of 40%-aqueous glucose solution

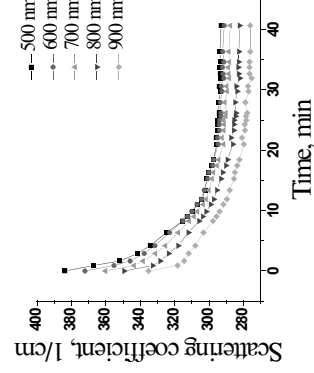


Fig.4. The time-dependent scattering coefficient of rabbit eye conjunctiva under the action of 40%-aqueous glucose solution

It can be noticed that the collimated wavelength-dependent transmittance increases in the course of 15 minutes for sclera and 30 minutes for conjunctiva. And we can presume that diffusion of glucose in these tissues and water from interstitial space to environmental solution caused by concentration gradient. Both processes make a contribution to the collimated transmittance increasing in the course of the first 10-30 minutes, in dependence on the sample. However, a satiation and even some decrease of the collimated transmittance value  $T_c$  occur in the period of time from 10-30 to 25-40 minutes for the sclera samples. It can be, seemingly, explained by the result of interaction of renewed

interstitial fluid and hydrated collagen and elastin fibers. The refractive index of these fibers increases because of bond water diffuses from the fibers to the interstitial fluid. For this reason the refractive index of interstitial fluid decreases slightly. Both processes lead to some increase of light scattering of the samples.

Different times and degrees of sclera and conjunctiva clearing can be explained by different structures and functions of these tissues. Sclera is the connective tissue basically consisting of chaotically interwoven collagen and elastin fibers which are merged into interstitial fluid (Komai, Ushiki, 1991). The basic conjunctiva component is also a porous connective tissue, however, a conjunctiva surface is covered with multilayer flat epithelium (Egorov, Baminskiy, 2007). Since eye bulb conjunctiva performs a protective function and saves eye from foreign substance penetration, the diffusion of chemical agents is complicated in this tissue. This fact explains the clearing time increase and clearing degree decrease of conjunctiva in comparison with sclera.

The experimental data allowed to estimate their glucose diffusion coefficient values on basis of algorithm presented above. We performed the calculations for nine wavelengths (500 nm, 550 nm, 600 nm, 650 nm, 700 nm, 750 nm, 800 nm, 850 nm, and 900 nm) for each sample. The average values of glucose diffusion coefficient in rabbit eye conjunctiva and sclera are  $(3.2 \pm 3.9) \times 10^{-7}$  and  $(9.38 \pm 6.84) \times 10^{-7}$  cm<sup>2</sup>/sec, respectively. Such value spread can be explained by peculiarities in structure of these tissue samples.

Presented results agree with our presumption about predominant influence of concentration diffusion, in which velocity of exchange flow of osmotic substance in tissue and interstitial fluid from tissue is defined by concentration gradient. Obtained values of glucose diffusion coefficient are smaller than that in water (Fizicheskie vechiny, 1991). It can be explained by sclera and conjunctiva complex structure-morphological composition that complicate the diffusion. It is expected that glucose diffusion coefficients will have some greater values in investigated eye tissues *in vivo*, because a diffusion coefficient rises with temperature increasing [Bretschneider, 1966; Rid et al., 1982; Bashkatov et al., 2003; Tuchin, 2010].

Presented results allow to conclude that proposed method for the diffusion coefficient estimation based on measurements of the changes of optical properties of tissue is the perspective instrument for investigation of diffusion processes of optical clearing agents in tissues.

#### Conclusion

Results of our investigation have shown that the application of 40%-aqueous glucose solution as a clearing agent allows effective control of optical parameters of conjunctiva and sclera. Particularly, we can see the increase of collimated transmittance of radiation passed through the rabbit eye conjunctiva and sclera on average in  $1.98 \pm 0.87$  and  $19.7 \pm 17.2$  folds, respectively, and scattering coefficient decrease on average in  $0.88 \pm 0.08$  and

$0.61 \pm 0.18$  folds, respectively, in the spectral range of 500–900 nm. It promotes increasing of penetration depth for optical radiation into tissue. Thus, the optical clearing can be used as a method of increase of effectiveness of optical diagnostics and treatment of different pathologies of visual organs.

#### Acknowledgements

The research has been made possible by grants: 224014 Photonics4life-FP7-ICT-2007-2; RUB1-2932-SR-08 CRDF; and Governmental contracts 02.740.11.0770, and 02.740.11.0879.

#### REFERENCES

- 1 *Бакуткин В. В., Шубочкин Л. П.* Увеличение светопропускания склеры и патологически измененных роговицы // Офтальмолог. журн. 1991. Т. 2. С.105-107.
- 2 Банюк Б. Методы оптической измерения // Офтальмолог. журн. 1988. 128 с.
- 3 *Башкатов А. Н., Генина Э. А., Синичкин Ю. П., Корубей В. И., Лакодина Н. А., Тучин В. В.* Определение коэффициента диффузии глюкозы в склере глаза человека // Биофизика. 2003. Т. 48. № 2. С. 309-313.
- 4 *Башкатов А. Н., Генина Э. А., Корубей В. И., Тучин В. В.* Оптические свойства склеры глаза человека в спектральном диапазоне 370-2500 нм // Оптика и спектроскопия. 2010. Т. 109. № 2. С. 226-234.
- 5 *Бретшнейдер С.* Свойства газов и жидкостей. Л.: Химия, 1966. 536 с.
- 6 *Генина Э. А., Башкатов А. Н., Синичкин Ю. П., Тучин В. В.* Оптическое проявление юкки под действием глицирина: исследование *ex vivo* и *in vivo* // Оптика и спектроскопия. 2010. Т. 109. № 2. С. 1312-1319.
- 7 *Егоров Е.А., Басинский С.Н.* Клинические лекции по офтальмологии, ГЭОТАР-МЕД: Москва; 2007
- 8 *Котык А., Яначек К.* Мембранный транспорт. М.: Мир, 1980. 341 с.
- 9 *Рид Р., Праусниш Дж., Шервуд Т.* Свойства газов и жидкостей. Л.: Химия, 1982. 592 с.
- 10 *Тучин В.В.* Лазеры и волоконная оптика в биомедицинских исследованиях. Москва : ФИЗМАЛПИТ, 2010. 488 с.
- 11 Физические величины : Справочник / под ред. Григорьева И.С., Мейхикова Е.З. М. : Энергоатомиздат, 1991. 1232 с.
- 12 *Bashkatov A.N., Genina E.A., Kochubey V.I., Tuchin V.V.* Estimation of wavelength dependence of refractive index of collagen fibers of scleral tissue // In Controlling of Tissue Optical Properties: Applications in Clinical Study. Valery V. Tuchin Ed. (European Biomedical Optics Week «EBIOS 2000»), Proc. SPIE 2000, V. 4162, P. 265-268.
- 13 *Komai Y., Ushiki T.* The three-dimensional organization of collagen fibrils in the human cornea and sclera // Investigative Ophthalmology & Visual Science. 1991. Vol. 32(8), P. 2244-2258.
- 14 *Liu H., Beauvoit B., Kimura M., Chance B.* Dependence of tissue optical properties on solute-induced changes in refractive index and osmolarity // J. Biomed. Opt. 1996. Vol. 1. # 2. P. 200-211.
- 15 *Nemati B., Rylander III H.G., Welch A.J.* Optical properties of conjunctiva, sclera, and the ciliary body and their consequences for transscleral cyclophotocoagulation // Appl. Opt. 1996. Vol. 35. N. 19. P. 3321-3327.

- 16 Nemati B., Welch A.J., Rylander III H.G. Optical model for light distribution during transscleral cyclophotocoagulation // Appl. Opt. 1998. Vol. 37. N. 4. P. 764-771.
  - 17 Tuchin V.V., Maksimova I.L., Zimnyakov D.A., Kon I.I., Matyutov A.H., Mishin A.A. Light propagation in tissues with controlled optical properties // J. Biomed. Opt. 1997. V. 2. № 4. P. 401-417.
  - 18 Tuchin V.V. Tissue Optics: Light Scattering Methods and Instruments for Medical Diagnosis. Bellingham: SPIE Press, 2007. 882 p.

CONTENT

<i>Baldin M. I.</i> Dynamical Behavior of Van Der Pol Generator with Time Delayed Feedback .....	5
<i>Bogina M.Y.</i> Deformation Models of Materials in Radiation Medium .....	9
<i>Chichvarina O., Galushka V., Bileenko D.</i> Artefacts in Sem: Hydrocarbon Contamination .....	12
<i>Dorokin D. M., Shilovskiy P. A.</i> The Method for Solving Differential Equations Systems on the Base of Quadrature Formulas .....	15
<i>Glukhova O. E., Kirillova I. V., Shunayev V. V.</i> Distribution of the Local Stress of Atomic Monolayer Graphene .....	20
<i>Glukhova O. E., Kolesnikova A. S.</i> Simulation of the Fullerenes Filled Nanotubes Bending .....	25
<i>Glukhova O. E., Vesel S. S.</i> Calculation of Bending and Elastic Properties of Monolayer Graphene .....	27
<i>Kopiel A. V.</i> Test For Quantitative Determination T-2 and Ht-2 Toxins .....	33
<i>Knyvorostukhin D., Molochko A.</i> Geomarketing Analysis of the New Sales Outlet Optimal Location (with the Saratov Pharmacy Network as an Example) .....	37
<i>Kozina A. M., Yanina I. U., Svenskaya U. I., Genina E. A., Portnov S. A., Bashkatov A. N., Tuchin V. V.</i> Photodynamic Lipolysis with Indocyanine Green .....	42
<i>Lapkovskiy R. Y.</i> The Processes Synchronization in The Model of Cause-Effect Complexes .....	46
<i>Osokina A.</i> Scanning Electron Microscopy Research of Biological Specimens .....	50
<i>Parashchenko I. I., Ptitskeva S. A., Smirnova T. D.</i> Sorption-Luminescent Determination of Eurofloxacine and Oxalic Acid .....	56
<i>Pogorelova E. S., Kulapina E. G., Makarova N. M.</i> The Main Physical and Chemical Properties of Nanofiltration Membranes Based on Alkylpyridinium Salts .....	59
<i>Pozharov M. V.</i> Quantum Chemical Study of Several Rare-Earth Metal Complexes with Organic Ligands .....	63
<i>Savina T. F.</i> Equilibrium Points in Antagonistic Games with Preference Relations .....	71
<i>Sadovnikov A. V., Rozhnev A. G.</i> Nonlinear Dynamics of The Electromagnetic Wave Propagation in 2D Periodic Nonlinear Structure .....	75
<i>Sergeeva T. A., Serov V. V.</i> Validity of the Wannier Threshold Law for Angular Correlation Width in Double Photoionization Of Atoms .....	80
<i>Sheshukova S. E.</i> Numerical Simulation of Envelope Solitons in Magnon Crystals Based on System of Nonlinear Schrodinger Equations .....	86
<i>Tarasov E. A., Buyanova Z. I., Samarskiy M. V.</i> The Synthesis of Carbon Nanotubes Using Liquid Catalysts .....	91
<i>Vorobieva E.V.</i> Technological System of Modeling Oil and Gas Basins .....	95
<i>Zhigunov</i> Dynamic Loading of Hydro Manipulator Effect on Its Long-Term Strength .....	101
<i>Zaiova I. V., Talanov S. E.</i> Studying the Nature Of Contact Corrosion Layers on Lead Alloys by Impedance Spectroscopy .....	103
<i>Zubkina E. A., Genina E. A., Bashkatov A. N.</i> Optical Clearing of Eye Tissues .....	107

Научное издание

**ПРЕДСТАВЛЕНИЕ  
НАУЧНЫХ ДОСТИЖЕНИЙ МИРУ.  
ЕСТЕСТВЕННЫЕ НАУКИ**

Материалы научной конференции молодых ученых  
«Presenting Academic Achievements to the World»

Выпуск 2

Ответственный за выпуск *Н.И. Иголкина*  
Технический редактор *Л.В. Агальцова*  
Оригинал-макет подготовила *Н.И. Степанова*

Подписано в печать 15.07.2011. Формат 60x84 1/16.  
Бумага офсетная. Гарнитура Таймс. Печать офсетная.  
Усл. печ. л. 9,76 (10,5). Уч.-изд. л. 9,8.  
Тираж 90 экз. Заказ 45

Издательство Саратовского университета.  
410012, Саратов, Астраханская, 83.  
Типография Издательства Саратовского университета.  
410012, Саратов, Астраханская, 83.